



Dipl.-Ing. Laura Watzlik, BSc

# **Numerical studies on progressive failure of ground anchors**

## **MASTER'S THESIS**

to achieve the university degree of

Diplom-Ingenieurin

Master's degree programme: Civil Engineering, Geotechnics and Hydraulics

submitted to

**Graz University of Technology**

Supervisor

Ao.Univ.-Prof. Dipl.-Ing. Dr.techn. M.Sc. tit.Univ.-Prof. Helmut Schweiger

Institute of Soil Mechanics and Foundation Engineering

Dipl.-Ing. Patrick Pichler, BSc.



## **AFFIDAVIT**

I declare that I have authored this thesis independently, that I have not used other than the declared sources/resources, and that I have explicitly indicated all material which has been quoted either literally or by content from the sources used. The text document uploaded to TUGRAZonline is identical to the present master's thesis dissertation.

---

Date

---

Signature



## Acknowledgement

I am using this opportunity to express my gratitude to everyone who supported me throughout the course of this master's thesis. I am thankful for their aspiring guidance, invaluable constructive criticism and friendly advice during the project work. I am sincerely grateful to them for sharing their truthful and illuminating views on a number of issues related to the thesis.

I express my warm thanks to Mr. *Ao.Univ.-Prof. Dipl.-Ing. Dr.techn. M.Sc. tit.Univ.-Prof. Helmut Schweiger* and Mr. *Dipl.-Ing. Patrick Pichler, BSc.* for their extraordinary guidance and support. Furthermore, I am also grateful to *Univ.-Prof. Dipl.-Ing. Dr.techn. Roman Marte* for his commitment to students' education.

I would also like to thank my thesis external guide Mr. *Dipl.-Ing. Dr.techn. Václav Račanský* from the company *Keller Grundbau Ges.m.b.H.* for the helpful information and discussions.

Special thanks are directed to my family for their support throughout my whole period of education. The same holds for my best friend Mr. *Dipl.-Ing. Michael Mayer, BSc.*, whose help in every condition of life is exceptionally invaluable. I would also like to thank the other fellow students about to take their diplomas for all the constructive discussions and advice.

Graz, June 2015

---

(Signature)



## Abstract

The present master's thesis deals with numerical simulations of the progressive failure mechanism arising along ground anchors in highly overconsolidated clay. This non-uniform distribution of shear stress is a result of the strain softening behaviour of this type of soil.

Finite element analyses are conducted in PLAXIS 2D incorporating two user-defined models: the Multilaminate soil model and the Shotcrete model. The former is a constitutive model applying a Hvorslev surface embedded in a multilaminate framework. It is employed for limiting peak shear strength in heavily overconsolidated soil with subsequent strain softening. Dilatant behaviour and peak friction angle are outcomes of the model. The second material model is utilised for the grout in the computations, as it is developed for simulating cemented materials. Tension softening reproduces cracking in the fixed length which results in an overall reduction in stiffness, whereas compression softening causes sudden failure in the free length.

The conducted studies are separated into two models, the basic and the advanced model. The difference between them is the grout in the free length that is simulated solely in the advanced model and increases the ultimate bearing capacity significantly. A number of sensitivity analyses and evaluations of the results are performed for both models.

## Kurzfassung

Die vorliegende Masterarbeit beschäftigt sich mit numerischen Studien des progressiven Bruchmechanismus, welcher entlang von vorgespannten Ankern in stark überkonsolidierten Tonböden auftritt. Diese ungleichmäßige Verteilung der Schubspannung ist ein Resultat der Entfestigung bei der genannten Bodenart.

Zwei benutzerdefinierte Modelle, die im Finite-Elemente-Programm PLAXIS 2D implementiert sind, wurden für die Durchführung der Analysen verwendet, zum einen das „Multilaminate soil model“ und zum anderen das „Shotcrete model“. Ersteres wendet eine Hvorslev-Fließfläche an, die in einem multilaminaten Stoffmodell eingebunden ist. Diese bestimmt die Festigkeit in stark überkonsolidierten Böden mit anschließender Entfestigung. Dilatantes Verhalten und der Peak-Wert des Reibungswinkels resultieren aus dem Modell. Das zweite Materialmodell wird auf den Mörtel angewandt, da es entwickelt wurde, um zementierte Materialien zu simulieren. Der Überschreitung der Zugfestigkeit folgt eine Entfestigung, die die Rissbildung in der Haftstrecke nachbildet. Dies hat eine Verringerung der Steifigkeit des gesamten Systems zur Folge. Durch Erreichen der Druckfestigkeit und anschließender Entfestigung kann hingegen plötzliches Versagen in der Freispielstrecke verursacht werden.

Die durchgeführten Studien sind in zwei verschiedene Modelle aufgeteilt, das Basismodell und das erweiterte Modell. Deren Unterschied ist der Zementmörtel in der Freispielstrecke. Dieser wird nur im erweiterten Modell berücksichtigt und erhöht die Tragfähigkeit des Ankers maßgeblich. Mehrere Sensitivitätsanalysen und deren Auswertungen werden im Zuge dieser Masterarbeit für beide Modelle durchgeführt.



# Table of contents

<b>1</b>	<b>Introduction</b>	<b>1</b>
<b>2</b>	<b>Ground anchor</b>	<b>2</b>
2.1	Progressive failure .....	3
2.2	Estimation of the bearing capacity .....	3
2.2.1	Shear strength .....	4
2.2.2	Ostermayer's nomograms .....	5
2.2.3	Undrained shear strength .....	6
2.3	Grouting .....	7
<b>3</b>	<b>Constitutive models</b>	<b>9</b>
3.1	Mohr-Coulomb model (MC) .....	9
3.2	Shotcrete model (SC) .....	10
3.2.1	Compression hardening and softening.....	10
3.2.2	Tension softening .....	11
3.3	Hardening soil model (HS) .....	12
3.4	Multilaminate soil model (MLSM) .....	12
3.4.1	Behaviour of stiff soil .....	12
3.4.2	Multilaminate framework.....	14
3.4.3	Yield function, softening and plastic potential .....	15
<b>4</b>	<b>Calculation model</b>	<b>18</b>
4.1	Model geometries and assumptions.....	18
4.2	Material parameters.....	22
4.2.1	Tendon.....	22
4.2.2	Grout.....	23
4.2.3	Soil.....	24
<b>5</b>	<b>Basic model computations</b>	<b>27</b>
5.1	Overview of performed analyses.....	27
5.2	Computation .....	29
5.3	Mesh sensitivity analysis .....	30
5.4	Reference model (MC) .....	33
5.5	Softening – MLSM .....	40
5.6	Dilatancy and peak friction angle – MLSM.....	44
5.7	Tension softening – SC model .....	52
5.8	Geometry impact .....	56
<b>6</b>	<b>Advanced model computations</b>	<b>57</b>
6.1	Overview of performed analyses.....	58
6.2	Modifications.....	59
6.3	Free length – mesh sensitivity analysis.....	63
6.4	Softening and dilatancy – MLSM.....	69
6.5	Compression softening – SC model.....	74
6.6	Geometry alteration .....	79
6.7	SC material parameter alteration .....	84
6.8	Bearing capacity grout.....	87
6.9	Pressure grouting .....	89

<b>7</b>	<b>Comparison to literature</b>	<b>94</b>
<b>8</b>	<b>Conclusion</b>	<b>96</b>
<b>9</b>	<b>Registers</b>	<b>98</b>
9.1	List of figures .....	98
9.2	List of tables .....	101
9.3	List of notations and abbreviations .....	102
9.4	References .....	105

# 1 Introduction

The main aspect of this thesis is the numerical simulation of ground anchors in heavily overconsolidated clay. This comprises modelling the non-uniform shear stress distribution that arises along the interface between grout and soil in such conditions. It is called progressive failure mechanism and is a result of the strain softening behaviour of overconsolidated clay.

Ground anchors are an essential tool for a wide field of application in geotechnical engineering. Their performance is limited by the efficiency of load transfer from tendon to soil via grout, induced by the progressive failure mechanism in overconsolidated soil.

The prime goal is to lay the foundations for optimising ground anchors in further investigations, especially in terms of a type called Single Bore Multiple Anchor (SBMA) that is supposed to reduce the impact of the progressive failure mechanism. Thus, this mechanism has to be realistically modelled, which is the main aim of the present thesis. Numerical studies can save on expenditures and effort compared to field tests, as parameters and geometries are easily altered once the simulation model is developed. The present thesis is conducted in cooperation with the ground engineering contractor Keller Grundbau GmbH.

The objectives in order to reach this aim are developing a reliable numerical model, followed by performance of a number of sensitivity analyses and evaluation of the results. For this purpose, a constitutive model incorporating a Hvorslev surface embedded in a multilaminate framework is employed for limiting the peak shear strength in heavily overconsolidated range with subsequent strain softening developed by Schädlich (2012). Furthermore, the impact of the grout is determined in terms of cracking and the free length. Thus, the shotcrete model (Schädlich and Schweiger 2014 b) for simulating cemented materials is applied for the grout. The conducted studies are separated into two models, the basic and the advanced model. The difference between them is the grout in the free length that is simulated only in the advanced model.

## 2 Ground anchor

Ground anchors have a broad field of application in geotechnical engineering such as slope stabilisation, cases of water buoyancy and retaining structures. The focus of the present thesis is set on the latter, yet, it is also adaptable to other disciplines. Moreover, it is restricted to the application in highly overconsolidated soil due to its unique behaviour. This chapter deals with the concept, the load-bearing behaviour, estimations of the bearing capacity and grouting of such an anchor.

A schematic longitudinal cross-section of the system employed in a structural support of a retaining wall is shown in Fig. 2.1. It is usually tilted at an angle of 10-15 ° to the horizontal in this application area, as shown by the angle  $\beta$ . The distal end is hereinafter referred to as the bottom end, whereas the proximal end is called the top end. The anchor is divided in two sections, namely the free and fixed anchor length. The prestress that is applied to the tendon at the anchor head is solely transferred to the fixed length, as load transfer in the free length is prevented by encapsulation of the tendon. However, both free and fixed length contain the same cement mortar, thus all termed grout.

The anchor segment that is termed fixed length is pressure grouted in order to increase the load bearing capacity of the anchor, which is why this part is enlarged, compared to the borehole diameter. The free length is only gravity grouted instead. Section 2.3 goes into detail of grouting.

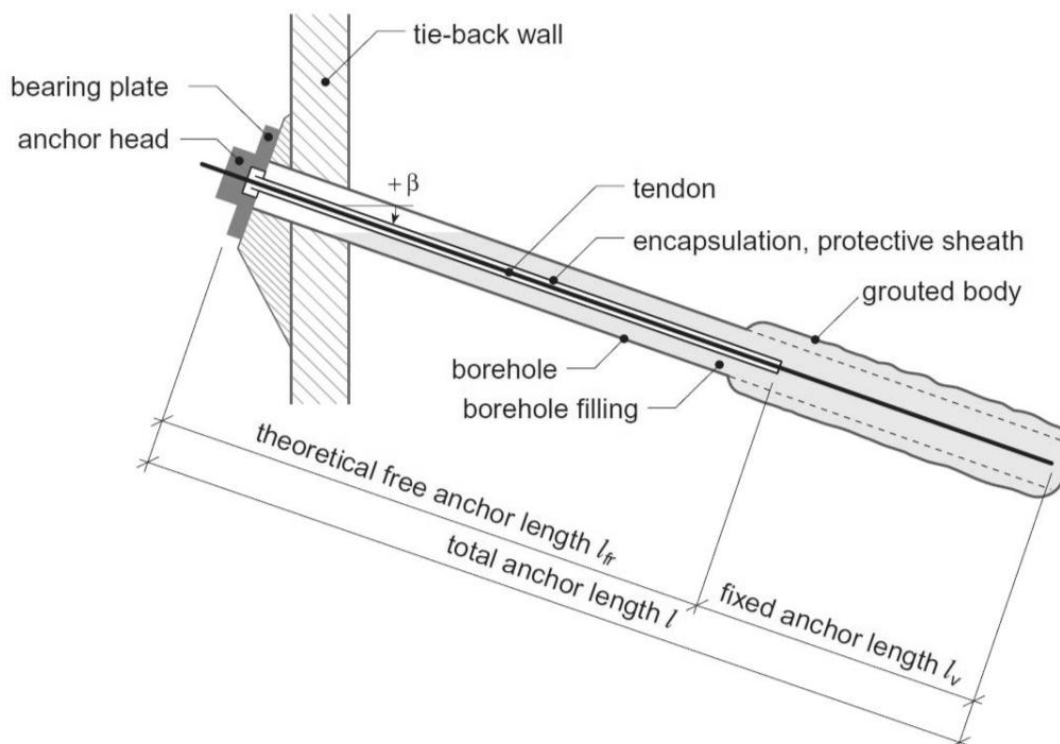


Fig. 2.1. Schematic longitudinal section and terminology of a prestressed ground anchor (Iten 2011)

The ultimate bearing capacity of ground anchors depends on many factors, as failure can occur in the following locations:

- Tendon
- Grout

- Soil
- Interface tendon-grout
- Interface grout-soil
- Any combination of the modes of failure mentioned above

Nevertheless, for ground anchors, failure generally takes place in the soil-grout interface (Xanthakos 1991) as tendon ribs prevent failure in the tendon-grout interface. More precisely, failure occurs within the soil along a shear zone but still in the area of the interface grout-soil. Thus, the following calculations, explanations and analyses in the present thesis will focus on this failure. Other failure mechanisms are still taken into account in the computations, but are not supposed to be decisive. The impact of the progressive course of debonding in the interface tendon-grout, starting from the top, and cracks in the grout is considered.

## 2.1 Progressive failure

For the abovementioned reason of being the decisive location of failure, the interface between soil and grout is subject of research. Moreover, a highly non-uniform distribution of shear stress along the anchor in stiff soil is proved by field, experimental and theoretical evidence e.g. by Barley (1997) and Ostermayer (1974) and widely acknowledged.

At the onset of anchor loading, ultimate bond stress  $\tau_{ult}$  is mobilised at the proximal end of the anchor. As the load is increased, the shear stress at this location decreases to the residual value  $\tau_{res}$  and the peak shear stress moves towards the end of the anchor. This phenomenon is referred to as progressive failure mechanism and is schematically illustrated in Fig. 2.2.

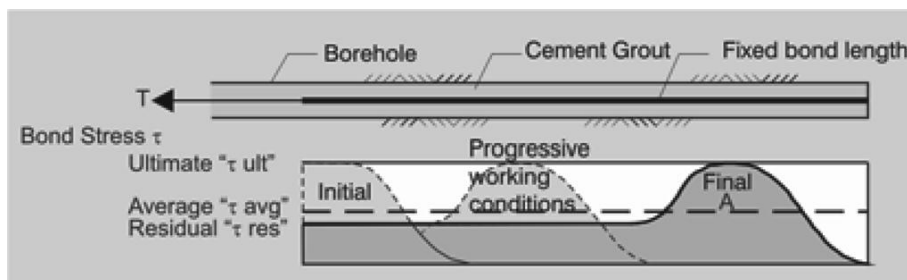


Fig. 2.2. Development of bond stress distribution along the fixed anchor length (Barley 1995)

This mechanism is associated with the growth of a slip surface in material with strain-softening behaviour (Terzaghi & Peck 1948). It is worth mentioning that this mechanism only appears in stiff material, such as overconsolidated clay, rock and dense sand. Incompatibility of the elastic properties of tendon, grout and soil is the widely acknowledged cause of this phenomenon (Barley 1995).

## 2.2 Estimation of the bearing capacity

The bearing capacity of anchors is not easily determined, especially when considering the progressive failure mechanism. For the sake of completeness, however, it should be noted that there

are also various influencing factors apart from that. Many of them are usually not taken into account. Some factors are listed in the following, however, not exhaustively:

- **Soil conditions**

The soil type and a variety of conditions have high impact on the ultimate bearing capacity.

- **Anchor installation**

The grout injection method, the injected volume and the boring technique are examples of effects of anchor installations that can have decisive effect on the load capacity.

- **Geometries**

Studies have e.g. shown that the skin friction is not direct proportional to the diameter of the grout body (Xanthakos 1991).

There are different approaches for estimating the bearing capacity of anchors. Analytical and empirical attempts to integrate the progressive failure mechanism were e.g. made by Ostermayer (1974) and Barley (1995). Selected examples that are employed for comparison to the numerical results are presented in this section.

### 2.2.1 Shear strength

This approach estimates the shear strength of the soil and sums it up along the grout surface. It is calculated according to Equ. (2-1), which basically estimates the force acting perpendicular to the grout surface caused by the overburden of the soil and derives the bearing capacity by multiplying by the friction coefficient, which is the tangent of  $\varphi$ . Parameter  $a_f$  is a factor to convert the vertical stress  $\sigma'_v$  to the stress acting normal to the grout surface. Some authors use the earth pressure coefficient at rest  $K_0$  and some much higher values for its determination. Fig. 2.3 explains the setting of the anchor. In general, this approach is only rarely applied these days, as it overestimates the bearing capacity in deep-set anchors and underestimates it for shallow anchors (Witt 2011). However, it is used when the calculation is conducted with the Hardening soil model in PLAXIS.

$$T_f = a_f \cdot \gamma \cdot h \cdot \tan\varphi \cdot A_M \quad (2-1)$$

$T_F$	[kN]	bearing capacity
$a_f$	[-]	factor for conversion to normal stress on lateral surface
$\gamma$	[kN/m <sup>3</sup> ]	unit weight
$h$	[m]	overburden
$\varphi$	[°]	friction angle
$A_M$	[m <sup>2</sup> ]	grout surface

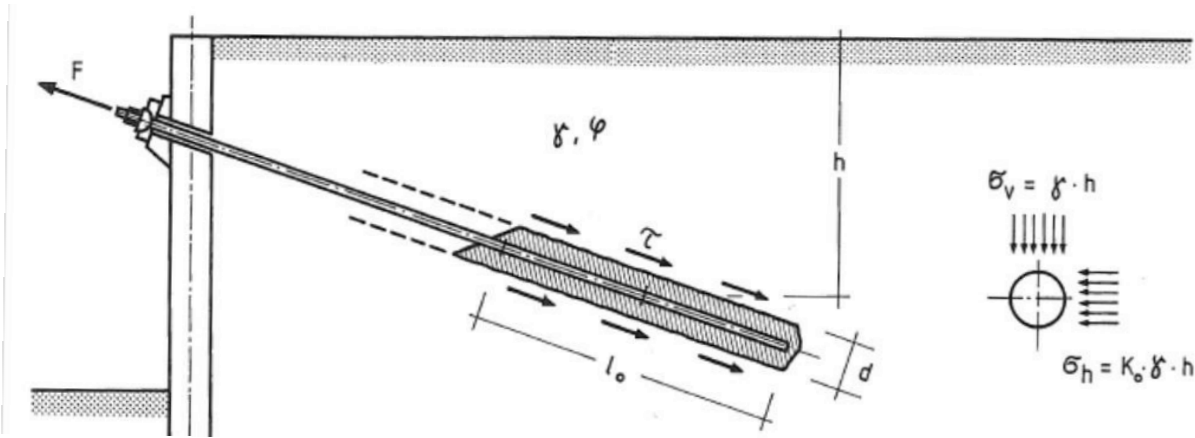
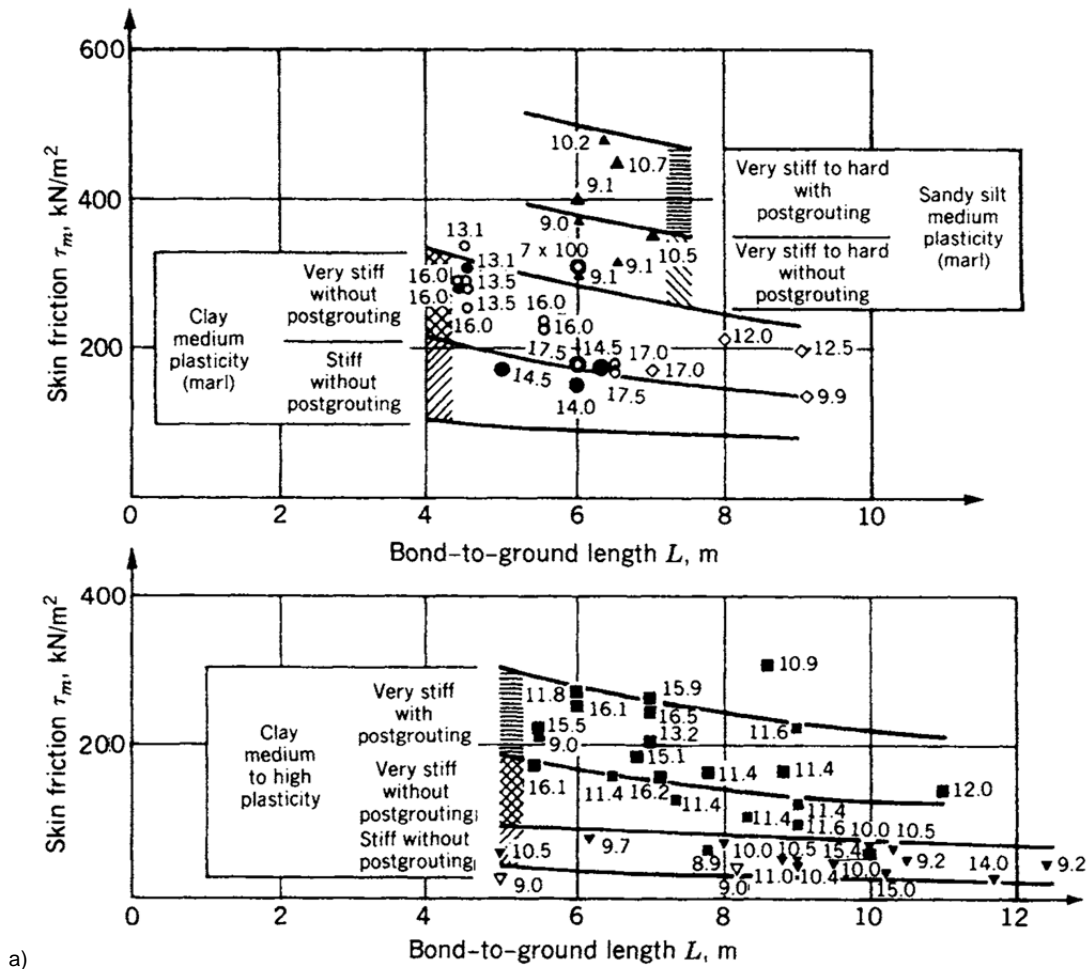


Fig. 2.3. Sketch for determination of the bearing capacity (Witt 2011)

### 2.2.2 Ostermayer's nomograms

As already mentioned, Ostermayer (1974) empirically and analytically integrated the findings about the progressive failure mechanism into load-bearing assessment of anchors. Fig. 2.4 shows the charts he proposed for the skin friction in cohesive soils in correlation with fixed anchor length. The influence of post-grouting, soil type, stiffness and plasticity is considered.



Failure load was reached	Failure load was not reached	Post-grouting	Type of soil	$W_L\%$	$I_p\%$	$I_c\%$
▲	△	Without	Silt, very sandy (marl) medium plasticity	~ 45	~ 22	~ 1.25
▲	△	With				
●	○	Without	Clay (marl) medium plasticity	32-45	14-25	1.03-1.14
●	○	With				
●	○	Without				
●	○	With				
	◇	Without	Silt medium plasticity	23-28	5-11	0.7-0.85
■		Without	Clay medium to high plasticity	48-58	23-35	1.1-1.2
■		With				
▼	▽	Without				

b)

Fig. 2.4. Correlation between fixed anchor length and skin friction in cohesive soil: a) diagrammatic representation, b) legend (Ostermayer 1974)

### 2.2.3 Undrained shear strength

Xanthakos (1991) proposed a theoretical approximation for anchor capacity, as demonstrated in Equ. (2-2). The undrained shear strength is applied along the grout surface instead of the friction. Furthermore, an adhesion factor  $a_{ad}$  is introduced in order to account for different soil types. For stiff clays, exhibiting undrained shear strengths  $c_u$  of about 95 kN/m<sup>2</sup>, this value was found to be between 0.28 and 0.45, which generally decreases with increasing shear strength (Xanthakos 1991).

$$T_f = \pi \cdot D \cdot L \cdot a_{ad} \cdot c_u \quad (2-2)$$

$D$	[m]	diameter
$L$	[m]	fixed length
$a_{ad}$	[-]	adhesion factor
$c_u$	[kN/m <sup>2</sup> ]	average undrained shear strength over fixed length

Barley (1997) proposed a similar estimation of the bearing capacity (see Equ. (2-3)), but replaced the adhesion factor  $a$  by an efficiency factor  $f_s$ . It does not only account for different soil types, but also for the progressive failure mechanism by being contingent on the length of the fixed length. For very stiff clays, he suggested the empirically perceived Equ. (2-4). It matches fairly well with the diagrammatic presentation of the ultimate medium skin friction against fixed length proposed by Ostermayer (1974), as shown in Fig. 2.4. For illustration, the efficiency factor is the ratio between the area  $A$ , as indicated in Fig. 2.3, and area calculated by the fixed length times the ultimate bond stress  $\tau_{ult}$ .

$$T_f = \pi \cdot D \cdot L \cdot f_s \cdot c_u \quad (2-3)$$

$D$	[m]	diameter
$L$	[m]	fixed length

$f_s$	[-]	efficiency factor
$c_u$	[kN/m <sup>2</sup> ]	undrained shear strength

$$f_s = 1.6 \cdot L^{-0.57} \quad (2-4)$$

$L$	[m]	fixed length
-----	-----	--------------

Koutsoftas and Ladd (1985) proposed an estimation for the undrained shear strength, taking the overconsolidation ratio  $OCR$ , the cohesion  $c'$  and the initial vertical stress  $\sigma'_{v0}$  into account, as represented in Equ. (2-5).

$$c_u \approx c' + (0.22 \pm 0.03) \cdot OCR^{0.8} \cdot \sigma'_{v0} \quad (2-5)$$

$c'$	[kN/m <sup>2</sup> ]	cohesion
$OCR = \sigma'_{vp} / \sigma'_{v0}$	[-]	overconsolidation ratio
$\sigma'_{vp} / POP$	[kN/m <sup>2</sup> ]	vertical pre-consolidation stress/ pre-overburden pressure
$\sigma'_{v0}$	[kN/m <sup>2</sup> ]	initial vertical stress

It has to be mentioned that the estimations of the bearing capacity do not consider the grout in the free length. Thus, it is assumed that only the fixed length transfers the load from grout to soil.

### 2.3 Grouting

It is widely acknowledged that pressure grouting has a substantial effect on the anchor pull-out capacity. According to Witt (2011), the overall bearing capacity can be increased by 20 % to 50 %. The reason is the increase in radial stress due to cavity expansion and the enlarged diameter, along which more skin friction can be mobilised in terms of ultimate bearing capacity. Ostermayer (1974) determined a dependency between the post-grouting pressure and the skin friction, which is diagrammatically presented in Fig. 2.5. Several factors influence the resulting skin friction, such as soil conditions and boring technique.

It is called pressure grouting when it is applied right after anchor installation and post-grouting when the cement mortar has time to cure before the pressure is applied. As a result, it cracks during this process. If no external pressure is applied, as it is always the case in free length, gravity grouting takes place by the weight of the grout. The pressures are usually in a range of 5-15 bar (Witt 2011).

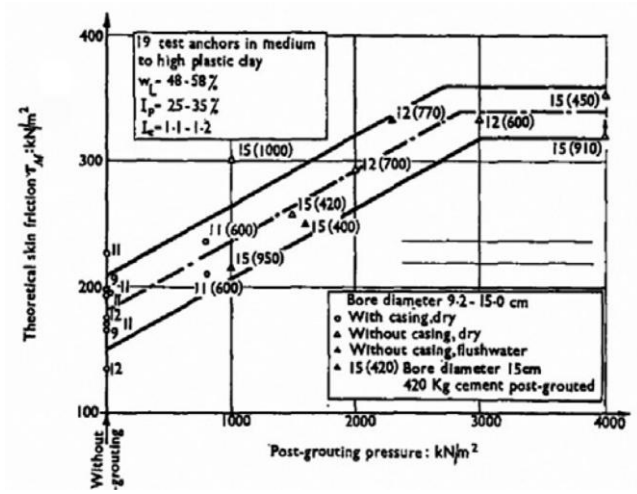


Fig. 2.5. Dependency between post-grouting pressure and skin friction (Ostermayer 1974)

### 3 Constitutive models

This section deals with the material models employed in the numerical simulations. Especially for those that are well-known, it is restricted to a brief overview, as the respective references provide in-depth explanations. For this reason, mathematical relationships are not represented. Stress-strain curves are one major basis for describing material behaviour. Examples and their characterisation are given in Fig. 3.1. The used models and their respective incorporated material behaviour are listed in Tab. 3.1.

Tab. 3.1. Application and material behaviour of applied constitutive models

Application	Constitutive model	Abbreviation	Material behaviour	
Tendon	Linear elastic	LE	Linear elastic	
Grout	Mohr-Coulomb	MC	Elasto-plastic	Linear elastic perfectly plastic
	Shotcrete model	SC		Strain hardening and softening in compression and softening in tension
Soil	Hardening soil model	HS		Strain hardening
	Multilaminate soil model	MLSM		Strain hardening in deviatoric and volumetric loading and softening in deviatoric loading

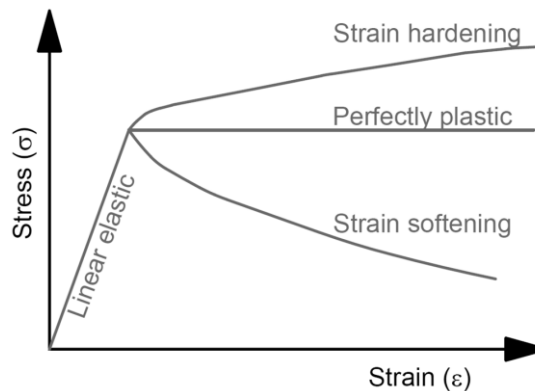


Fig. 3.1. Stress-strain curves of different material behaviours

#### 3.1 Mohr-Coulomb model (MC)

The Mohr-Coulomb (MC) model is employed for simulating the grout in selected cases, thus exhibiting a linear elastic perfectly plastic behaviour. Just as all other described material models in this chapter, strain is comprised of reversible elastic and irreversible plastic deformations. Detailed information about the implementation in PLAXIS is given by Brinkgreve et al. (2014 a).

The Mohr-Coulomb failure criterion is a means of defining shear strength and is also used in other constitutive models applied in the present thesis; it is e.g. shown in Fig. 3.2.

Compared to the other employed constitutive models, only a small number of material parameters are necessary for conducting numerical studies. In the course of their determination in section 4.2.2, further details are given for its application.

## 3.2 Shotcrete model (SC)

The Shotcrete model (SC) is the second constitutive model that is employed for simulating the grout in the numerical studies of the present thesis. It is developed at Graz University of Technology (Schädlich and Schweiger 2014 b) as user-defined soil model for PLAXIS. Originally, it was created to simulate shotcrete lining in conventional tunnelling. However, as the main benefit is the formulation of the material behaviour of concrete, it can be applied to other cemented materials as well. In the present case, it is employed for grout material in order to assess the influence of cracking on the behaviour of the anchor. For this purpose, strain hardening and softening are implemented in this elastoplastic constitutive model, which is explained in this chapter. Moreover, the SC model features time dependent stiffness and strength as well as creep and shrinkage. However, this material behaviour is not taken into account, as the grout is supposed to be cured and having reached final strength and stiffness at the time it is loaded.

The SC model applies a Mohr-Coulomb yield surface  $F_c$  for deviatoric loading that rotates about the point  $\sigma_{rot}$ . Failure is governed by a Mohr-Coulomb failure line. Furthermore, a Rankine yield surface  $F_t$  is featured for tensile loading (see Fig. 3.2).

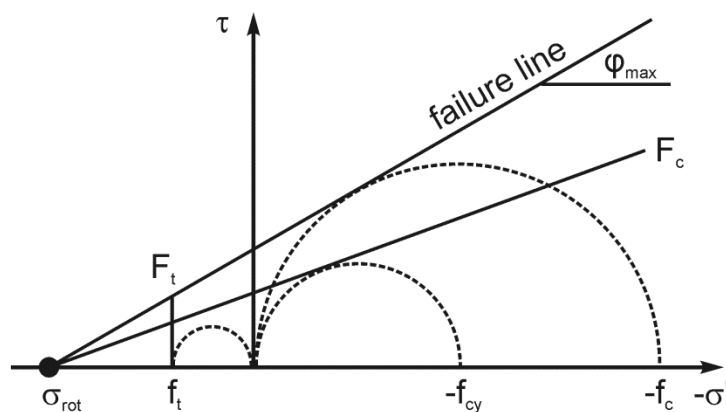


Fig. 3.2. Yield surface and failure line (Schädlich and Schweiger 2014 b)

### 3.2.1 Compression hardening and softening

Concrete exhibits plastic behaviour under compressive stress before reaching its peak strength  $f_c$ . The yield surface  $F_c$  equals the Mohr-Coulomb failure line at full mobilisation, after which the compressive strength decreases to a residual level. Thus, the stress-strain curve can be divided in four sections, as shown in Fig. 3.3. The minor principal plastic strain  $\varepsilon_3^p$  at the abscissa is normalised by the plastic peak strain in uniaxial compression  $\varepsilon_{cp}^p$ , resulting in a hardening/softening parameter  $H_c$ . The reason is the featured time dependency that could change the plastic peak strain.

Part I is characterised by quadratic strain hardening along with mobilisation of the yield surface. Subsequently, linear strain softening occurs in Part II. As strength reduction is assumed to be caused by the destruction of inter-particle bonds, cohesion softening is implemented. Thus, softening is simulated by a parallel shift of the fully mobilised Mohr-Coulomb failure envelope. This section is governed by the input value for the fracture energy in compression  $G_c$  and the normalised failure

strength in compression  $f_{cfn}$ . Part III exhibits linear strain softening again, followed by the constant, user-defined residual strength in Part IV.

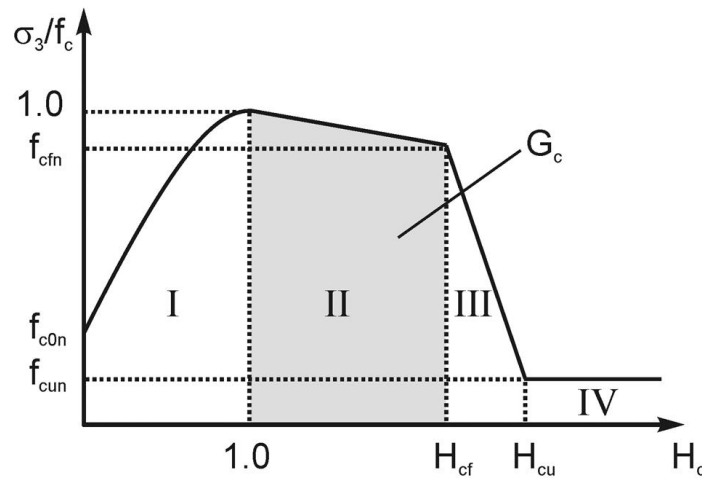


Fig. 3.3. Normalized stress-strain curve in compression (Schädlich and Schweiger 2014 b)

### 3.2.2 Tension softening

The material behaviour of the SC model is assumed to be linear elastic in tensile loading until the tensile strength  $f_t$  is reached. Subsequently, linear strain softening occurs to the residual tensile strength  $f_{tu}$  (see Fig. 3.4). Once it is reached, no further softening occurs.

Similar to compression softening, a normalised tension softening parameter  $H_t$  is introduced, which indicates the ratio between the major principle plastic strain  $\varepsilon_1^p$  and the plastic ultimate strain in uniaxial tension  $\varepsilon_{tu}^p$ . The latter is derived from the input value of the fracture energy in tension  $G_t$ .

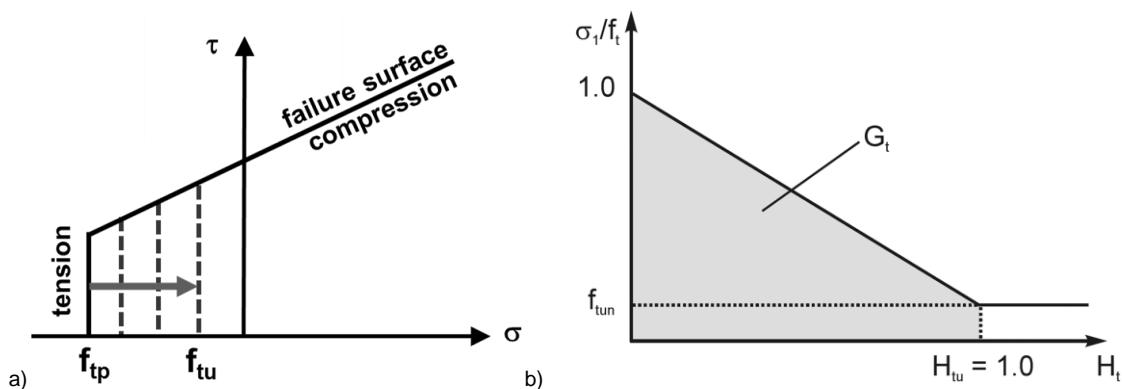


Fig. 3.4. Tension softening: a) yield surface, b) normalized stress-strain curve in tension (Schädlich and Schweiger 2014 b)

When the peak tensile or compressive strength is reached in the MC model, it stays at that level, whereas it decreases to the residual level in the SC model. Furthermore, the strain behaviour can be adapted to the applied cemented material. These are the main advantages of employing the SC model in the present case, as it considers the state of cracked concrete.

### 3.3 Hardening soil model (HS)

The Hardening Soil (HS) model is employed in any of the calculation models for at least parts of the soil. However, in many of them it is restricted to areas that are not subject to high strains, as it is the case in the shear band that develops along the grout surface. Unlike the MLSM that is applied in those areas, it is not capable of simulating strain softening, but the computational effort is much lower.

This advanced elastoplastic constitutive model simulates shear hardening as a result of primary deviatoric loading and compression hardening in oedometer and isotropic loading (Brinkgreve et al. 2014 a). Thus, it employs a shear and a cap yield surface. The Mohr-Coulomb failure criterion is applied as well. The model distinguishes between stiffness in primary loading and in elastic unloading/ reloading. Furthermore, stress dependency of soil stiffness is implemented.

### 3.4 Multilaminate soil model (MLSM)

The multilaminate soil model (MLSM) is developed at Graz University of Technology by Galavi (2007) and Schädlich (2012). It is implemented as user-defined soil model (UDSM) in PLAXIS in three different versions: the basic model with cohesion and friction strain softening and the Hvorslev model with and without regularisation. The second one is applied in the present thesis and briefly described in this chapter. A more detailed description is given by Schädlich (2012). It is an elastoplastic soil model that limits shear strength in heavily overconsolidated soils by a Hvorslev surface with subsequent strain softening. The model also features small strain stiffness that is not taken into account in this thesis.

This chapter describes the behaviour of stiff soil, its implementation in a constitutive model and the multilaminate framework. The required parameters and their calibration are discussed in the course of material parameter definition for the calculation model in section 4.2.3 and sensitivity analyses of those parameters of the anchor in section 5.5.

#### 3.4.1 Behaviour of stiff soil

The behaviour of stiff soil differs from soft soil, as it is characterised by a lower initial void ratio and a higher shear strength that can be further enhanced by inter-particle bonding and cementation (Schädlich 2012). Furthermore, it often exhibits anisotropic shear strength and stiffness. Although this applies to highly overconsolidated clay and dense sand, they cannot be described by the same mathematical formulations. Thus, this model can only be employed for highly overconsolidated clay. Its behaviour is schematically illustrated in Fig. 3.5 in drained triaxial compression in comparison to the normally consolidated state. The overconsolidated soil exhibits small initial contraction that is followed by expansion. The peak strength is mobilised at maximum dilatancy and reaches the critical stress ratio  $M_{cs}$  when additional shearing does not result in further volumetric strain. On the contrary, normally consolidated state exhibits solely contractant behaviour.

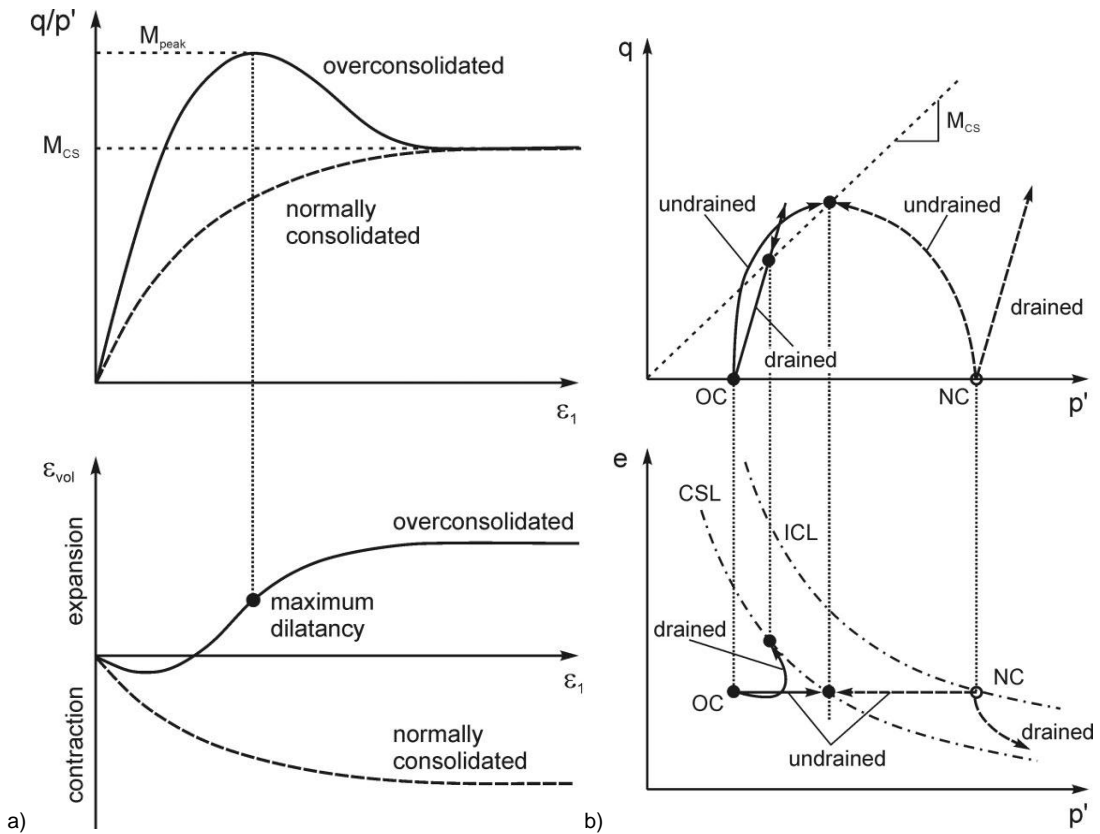


Fig. 3.5. Behaviour of overconsolidated clay: a) stress-strain behaviour and dilatancy, b) schematic stress paths and volumetric behaviour (Schädlich and Schweiger 2014 a)

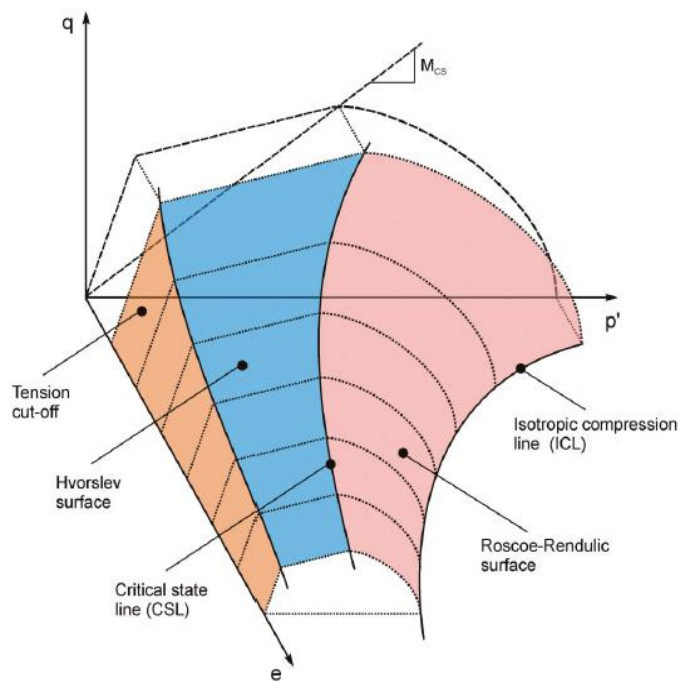


Fig. 3.6. 3D state boundary surface (Schädlich 2012)

The stress paths and the respective volumetric behaviour in drained and undrained conditions are illustrated in Fig. 3.5b. The overconsolidated paths go beyond the critical stress ratio  $M_{CS}$ , which is only reached after development of excess pore pressures in undrained conditions or loosening of the material in drained conditions. These illustrations are merged into the surfaces in the three-dimensional  $e$ - $p'$ - $q$  space in Fig. 3.6 that separate admissible and non-admissible states. The void

ratio and the overconsolidation ratio (OCR) define the location within these surfaces. This also determines the behaviour of the soil, as at low confining pressure pronounced dilatancy and shear strength higher than critical prevail while the same soil contracts at high stress levels. Irrespective of that, if sufficient deviatoric loading is applied to the soil, the stress path will reach the critical state line (CSL). Shear strength is limited by the Hvorslev surface at the left (“dry”) side of the CSL and by the Roscoe-Rendulic surface at the right (“wet”) side (see Fig. 3.6).

The described behaviour of stiff soil is usually considered by increasing the friction angle  $\varphi'$  in dense sands or the cohesion  $c'$  in overconsolidated soil, respectively, and still using a Mohr-Coulomb failure criterion. However, this approach does not reproduce strain softening during the transition to normally consolidated soil at high stress levels. As a result, the load bearing capacity in case of high strains is overestimated. This may not be relevant for many load conditions. However, in the case of the progressive failure mechanism, which is subject of the present thesis, shear strength is fully mobilised and failure is approached. Furthermore, the post-peak behaviour is necessary to be considered, as parts are softened before others have reached peak shear strength along the slip surface.

### 3.4.2 Multilaminate framework

The multilaminate framework is based on the principle that the behaviour of soil as a matter of particles and their interaction. Thus, the macro-mechanical behaviour is based on the micro-mechanical scale. Since calculating in this micro-mechanical scale would lead to an enormous computational effort, it has to be simplified. In a multilaminate model, these limitations can be avoided by considering soil as a continuum with potential sliding planes. The continuum delivers the elastic and the sliding planes the plastic deformations. The MLSM has a selectable number of sliding planes, so-called integration planes with pre-defined orientation, as can be seen in Fig. 3.7. The behaviour of the soil is formulated on these planes that exist in each stress point. However, unlike stress and strains, the parameters are globally determined instead on that microscopic level. The global three-dimensional stress state can be derived by the sum of the local two-dimensional stress states at planes. Integration of the local strains over all planes leads to the macroscopic strain response to the stress increment.

However, the Hvorslev yield surface and this kind of constitutive model in general can also be implemented in a model based on macroscopic stress and strains in a similar way. The reason for the application of this approach is strain softening that causes severe mesh dependency. It can be overcome by a non-local strain regularisation technique. A weighting factor is assigned to each plane in order to account for its influence with regard to the volume. Different weighting functions are implemented in the MLSM for this non-local approach. It is based on the assumption that the behaviour of a local stress point depends on a particular volume surrounding it.

Furthermore, as the yield surfaces and plastic potential are defined individually on the integration planes, initially isotropic material becomes anisotropic after loading, intrinsically capturing plastic flow induced anisotropy.

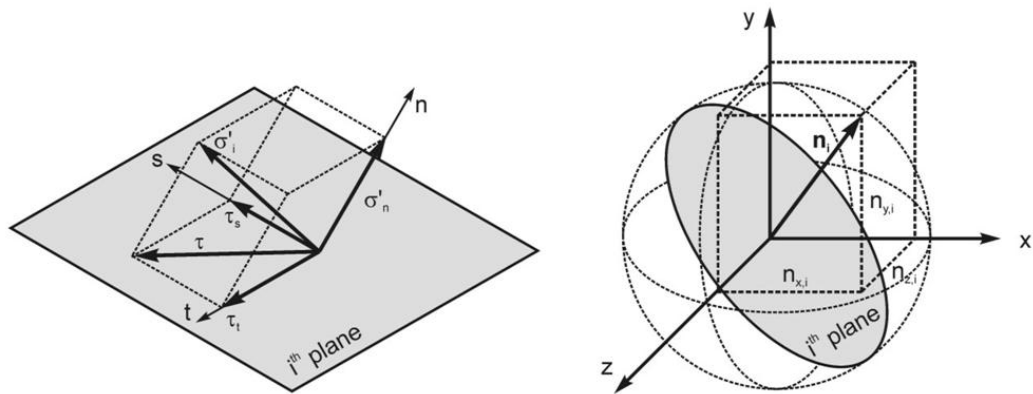


Fig. 3.7. Definition of local stress components and integration plane orientation (Schädlich and Schweiger 2014 a)

### 3.4.3 Yield function, softening and plastic potential

For the implementation in a constitutive model, three yield surfaces are employed, which are displayed in Fig. 3.8. The cap yield surface  $f_{cap}$  for normal compression and the cone yield surface  $f_{cone}$  for deviatoric loading separate the elastic region from the plastic domain. Their mobilisation is formulated according to strain hardening plasticity in deviatoric and volumetric loading, as change of the yield surface is driven by the change of local plastic strains.

Fully associated plastic flow is assumed for the elliptic volumetric hardening surface  $f_{cap}$ . The cap plastic potential equals the yield function. Its position is defined by the current pre-consolidation stress  $\sigma'_{nc}$  at the  $\sigma'_n$ -axis and the intercept of the cap shape parameter  $M_{cp}$  with the  $\tau$ -axis (see Fig. 3.8) that is defined in an iterative procedure in order to ensure that the stress state at rest  $K_{0,nc}$  is met.

A non-associated plastic potential function is assumed for the linear shear hardening surface for deviatoric loading  $f_{cone}$  and the Hvorslev yield surface  $f_{HV}$ .

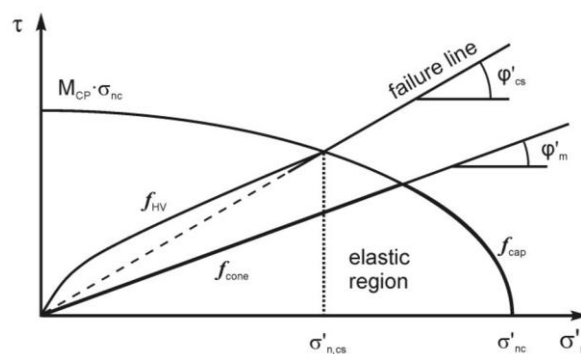


Fig. 3.8. Local yield surfaces (Schädlich 2012)

The location of the Hvorslev surface is defined by the intercept of the CSL and the cap yield surface and the Hvorslev surface inclination  $\varphi'_e$  that is found out to be approximately  $3^\circ$  to  $6^\circ$  below the critical state friction angle  $\varphi'_{cs}$  (Schädlich 2012). Therefore the normalised intercept with the  $\tau$ -axis  $c'_{HV}$  is no independent material parameter. This is shown in Fig. 3.9, which is adjusted to the multilaminate framework by normalisation with the equivalent stress  $\sigma'_{ne}$  at the local normal compression line as it decreases with  $\sigma'_n$ . The shape of the Hvorslev surface is particularly sensitive to the power exponent  $m$  and the stiffness ratio  $E_{ul}/E_{oed}$ .

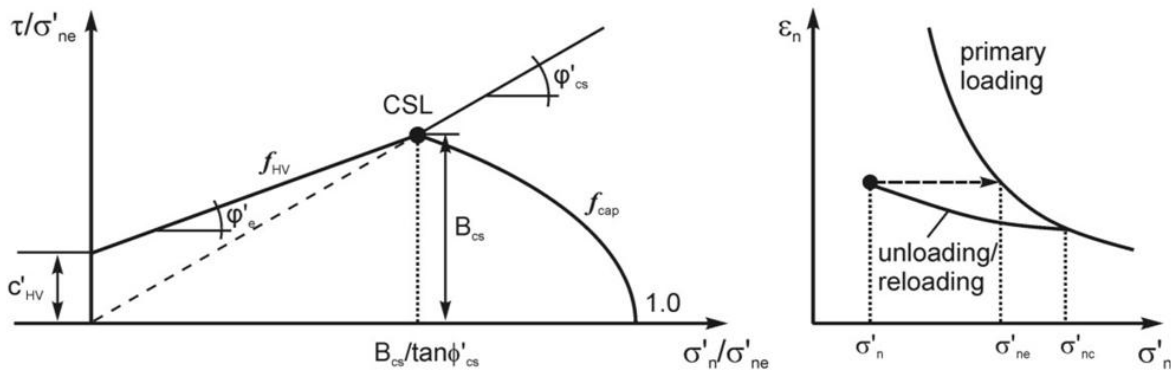


Fig. 3.9. Normalised Hvorslev surface on integration plane (Schädlich 2012)

The Hvorslev yield surface acts as a strength boundary surface, which only gets activated once the local stress path reaches it. Yet, unlike the Modified Cam Clay model, the strain hardening deviatoric yield surface induces plastic strains also for stress states below that surface.

Hardening at the cap yield surface enlarge the pre-consolidation stress  $\sigma'_{nc}$  and negative (compressive) plastic normal strains occur. On the contrary, positive plastic normal strains, caused by dilatancy at the Hvorslev surface, reduce the pre-consolidation stress  $\sigma'_{nc}$ . Hence, the softening and hardening rule are equal. The relation between mobilised shear stress and non-local damage strain is shown in Fig. 3.10.

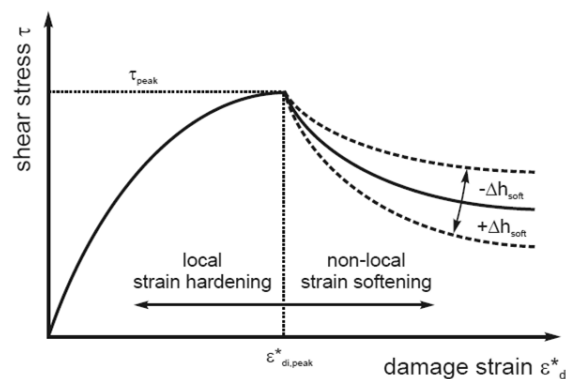


Fig. 3.10. Difference in approaches of strain hardening and softening (Schädlich 2012)

As already mentioned, a non-associated plastic potential function is assumed for the cone and Hvorslev surface. For the former, it equals the cone yield function with the mobilised friction angle  $\phi'_m$  being replaced by the mobilised angle of dilatancy  $\psi_m$ . Thus, the direction of plastic strain increment is controlled by the angle of dilatancy  $\psi_m$ . It depends on the mobilised friction angle  $\phi'_m$  below the critical state line and the maximum angle of dilatancy  $\psi_{max}$  above it, which is the difference between the critical state line and the Hvorslev surface at the current local stress state. These relationships are illustrated in Fig. 3.11. At full mobilisation, the cone yield function equals the one of the Hvorslev surface. Afterwards,  $\psi_{max}$  is reduced with increasing stress level and proceeding softening. If sufficient deviatoric loading is applied, critical state is reached at which point no dilation occurs and the mobilised friction angle equals the critical state friction angle. As a result, dilatant behaviour is an outcome of the model that depends on the overconsolidation ratio.

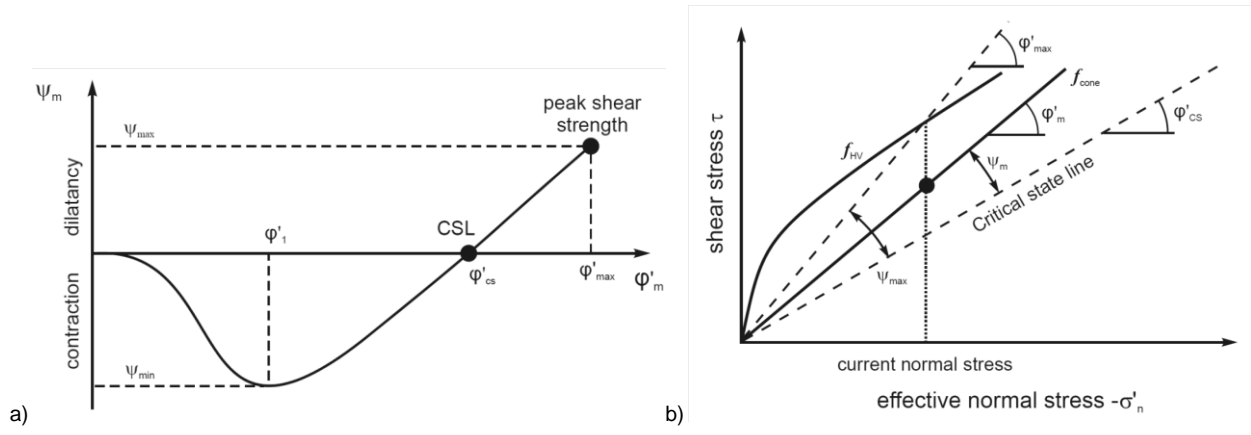


Fig. 3.11. Dilatancy: a) mobilisation, b) mobilised and maximum angle of dilatancy (Schädlich 2012)

## 4 Calculation model

This chapter describes the basic assumptions, geometries and material parameters for the basic calculation model. Only slight alterations are conducted for the advanced models that are explained in section 6.2.

### 4.1 Model geometries and assumptions

In order to be able to create a FE-model, the system has to be idealized, which is explained in this section. All FE-calculations in this thesis are carried out with PLAXIS 2D AE.02. Whenever PLAXIS is mentioned, it is referred to this version. Moreover, two user-defined soil models (UDSM) are utilised. The version named “mms\_hv” of the MLSM and “scm\_v8.0” of the SC model are integrated in PLAXIS for this purpose.

The encountered task principally requires a three-dimensional model in order to reproduce the existing stress distribution. In order to save calculation time and modelling effort, an axisymmetric model implemented in the 2D version of PLAXIS is chosen. In PLAXIS, the only possible axis of symmetry is the vertical axis Y. The difference between plane strain and axial symmetry is depicted in Fig. 4.1. Thus, the anchor is vertical instead of inclined.

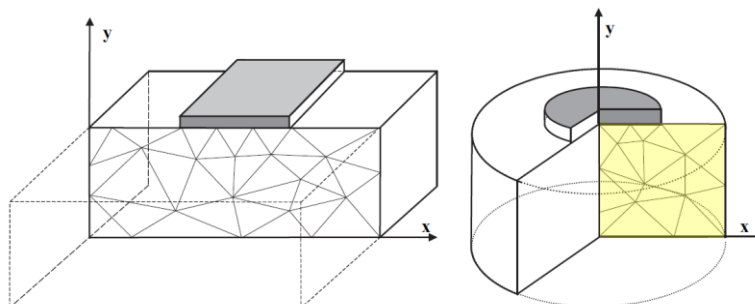


Fig. 4.1. 2D – axial symmetry (Brinkgreve et al. 2014 b)

Tab. 4.1. Parameters and results of the initial stress state

Approximated perpendicular initial stress state		
Stress at ground surface	kN/m <sup>2</sup>	0.00
Stress at the distal end of the anchor	kN/m <sup>2</sup>	190.00
Total anchor length	m	21.00
Soil unit weight	kN/m <sup>3</sup>	18.50
Input soil unit weight	kN/m <sup>3</sup>	9.20

The conversion from the inclined to the vertical system is shown in Fig. 4.2. The most important effect of this simplification is the initial stress state. Particularly in back analyses of anchor loading, special care has to be taken reproducing the stress state in the vertical model, since the stress perpendicular to the axis of the anchor has a major impact on its ultimate bearing capacity. This was taken into account by evaluating the initial stress state, as shown in Fig. 4.2 (“Approximated perpendicular initial stress on anchor  $\sigma_n'$ ”), and transferring it to the vertical axis. The cross for the initial stress shows an overconsolidated state, since this type of soil is used for the analyses. This stress state is turned in

Fig. 4.2b, but simulated as isotropic for simplification purposes. The implementation in PLAXIS was realized by reducing the soil unit weight and setting the earth pressure coefficient at rest  $K_0$  to 1.0. Hence, the initial deviatoric stress is zero. Yet, stiffness and stress acting perpendicular to the anchor are increasing with depth, but to a lesser extent. The overburden at the anchor head is set to 4 m and the inclination is  $15^\circ$ . The results of this approximation are listed in Tab. 4.1.

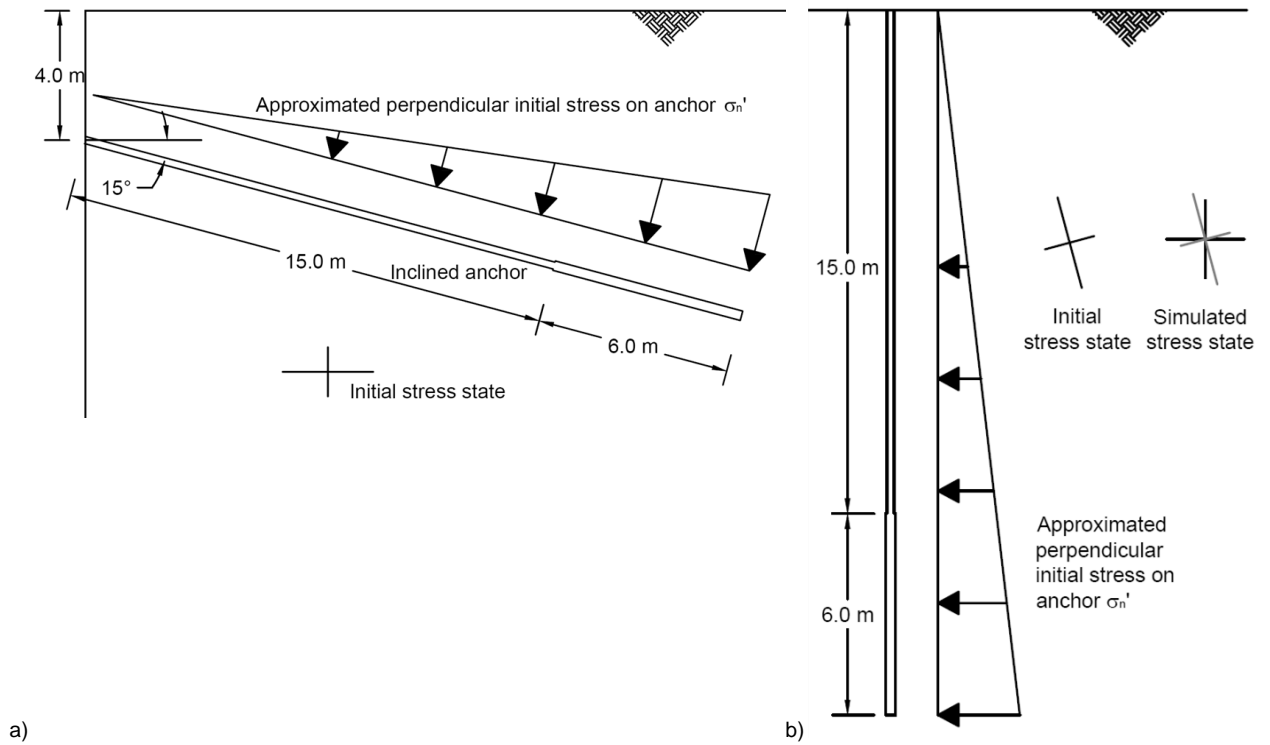


Fig. 4.2. Conversion from the inclined to the vertical system: a) inclined, b) vertical

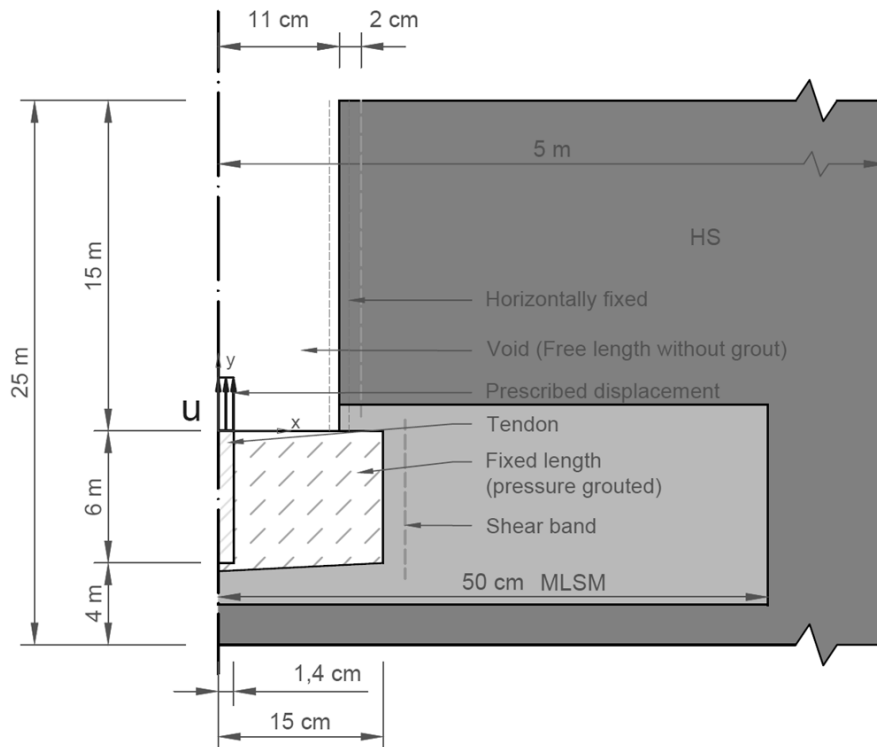


Fig. 4.3. Basic model geometries (horizontally scaled up 50 times)

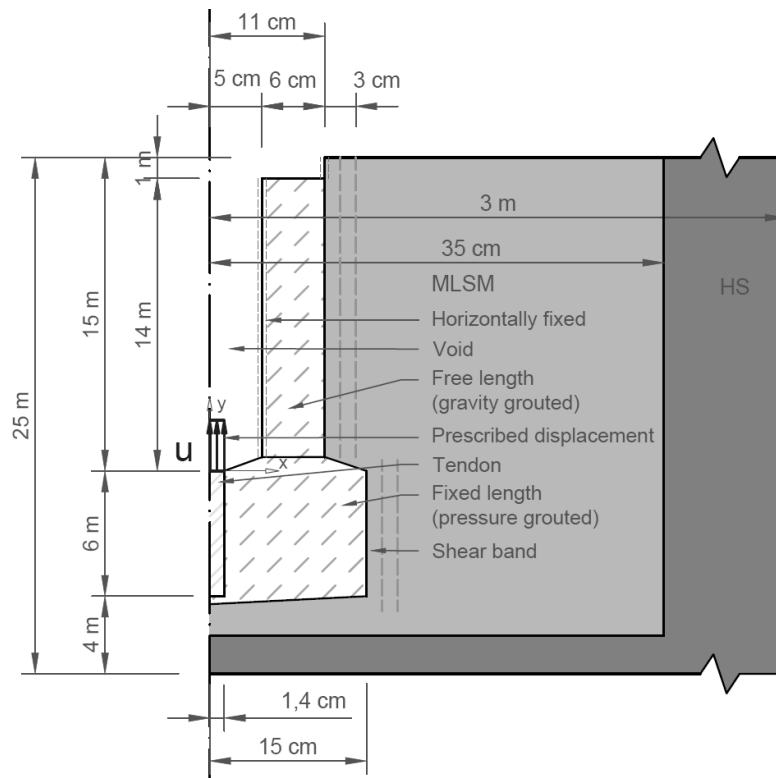


Fig. 4.4. Advanced model geometries (horizontally scaled up 50 times)

Plastic analysis is used with staged construction as the loading type. The anchor load tests are displacement controlled. Prescribed displacements of 0.4 cm are assigned to the tendon at the top of the fixed length in each calculation phase, as the tendon is not modelled in the free length.

6-noded triangular elements are chosen, since 15-noded elements take significantly more calculation time. The analyses are performed in drained conditions with the phreatic level below the model.

Fig. 4.3 and Fig. 4.4 depict the geometries the way the model is implemented in PLAXIS. They show the plane of the calculation models, which is rotating around axis Y, indicated by yellow shading in Fig. 4.1. These figures are horizontally scaled up 50 times for better visualisation. The difference between them is the grout in the free length. The anchor free length is usually filled with the same cement mortar as the fixed length and only in some cases flushed out afterwards. Thus, as opposed to the usual model assumptions, the load transfer in terms of shear stress between grout and soil is not limited to the fixed length. Nevertheless, basic analyses in this thesis are carried out without it in order to separate the impact of factors like parameters and geometries on the system of the anchor. Adding the grout in the free length results in a significant increase in calculation time. The reason for the higher computation effort is not solely the additional grout stress points, but the extended area for the application of the MLSM. This is necessary in order to simulate the progressive failure in this part as well. Particular attention should be given to the layer of elements for strain softening along the grout, indicated by the dashed line (see Fig. 4.3 and Fig. 4.4). This is of importance for the MLSM, as a regular, sufficiently small arrangement of finite elements has to be created. The width of this shear band is set to 2 cm, which is equal to approximately 13 % of the radius of the fixed length. Restrictions are imposed by the mesh fineness and its quality, respectively. The influence of the width and other related input parameters are given in section 5.5. The constitutive models itself are

described in chapter 3. The MLSM is applied in the areas around the grout in a radius of 0.5 m. The soil adjacent to the MLSM, in which no shear band is supposed to develop, is modelled with the HS model.

The fixed length is 6 m and the free length is 15 m. The model has a radius of 5 m and is 25 m in height, whereof 15 m are above the fixed length and 4 m below. The origin of ordinates is at the proximal end of the fixed length. The borehole has a radius of 11 cm, which is extended to 15 cm via pressure grouting in the area of the fixed length. Fig. 4.3 and Fig. 4.4 include detailed dimensioning of the models. Moreover, the major geometries and assumptions are summarized in Tab. 4.3.

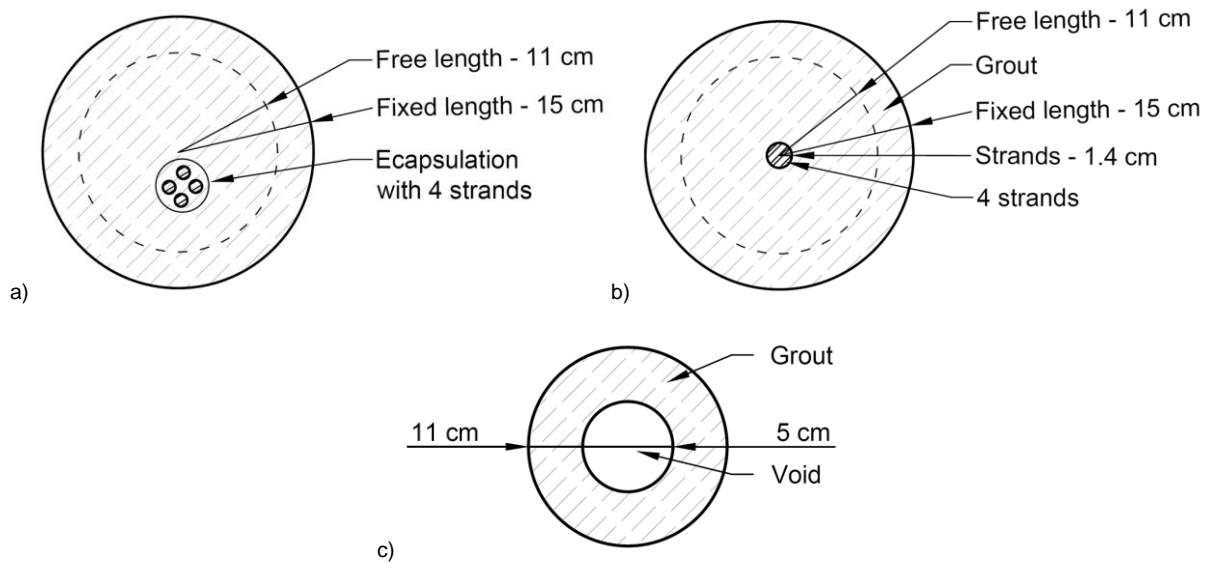


Fig. 4.5. Discretisation of the cross section: a) schematic section of fixed length, b) discretised section fixed length, c) discretised section free length

Tab. 4.2. Axial stiffness and force at failure – free length with and without void and comparison of free and fixed length

Axial stiffness and force at failure – free length with and without void			
Radius void	$r_{void}$	cm	5
Radius free length	$r_{free}$	cm	11
Area 4 strands	$A_{strands}$	cm <sup>2</sup>	6
Area free length	$A_{free}$	cm <sup>2</sup>	374
Area of the modelled grout	$A_{grout}$	cm <sup>2</sup>	302
Decrease in axial stiffness and force at uniaxial failure		%	-19
Axial stiffness and force at failure – free length and fixed length			
Radius fixed length	$r_{fixed}$	cm	15
Area fixed length	$A_{fixed}$	cm <sup>2</sup>	705
Increase in axial stiffness and force at uniaxial failure		%	+134

A void with a radius of 5 cm is arranged in the free length, which is depicted in Fig. 4.5c. The grout around it is horizontally supported. The gap size is defined on the basis of other objects and imperfections contained in the grout, such as the tendon, injection hoses, soil and air intrusions. Although the material of the grout in the fixed and free length is the same, the main difference is grouting. The free length is only gravity grouted instead of pressure grouted, as in the fixed length. This results in a decrease in axial stiffness  $EA$  and in the force at failure. The modelled void causes a decrease of 19 % in both, compared to the condition with grout in the void, as calculated in Tab. 4.2.

In contrast, the axial stiffness and the force at failure increase by 134 % in the fixed length compared to the modelled free length. In order to avoid singularities, constant expansion of the grout body from fixed length to free length is defined (see Fig. 4.4).

Both Fig. 4.5 a and b depicture a cross section of the fixed length with the difference of shape and location of the tendon. In the calculation model, the four single strands acting in the fixed length are located on the axis and modelled as one continuum. Thus, the eccentricity is neglected.

Tab. 4.3. Main geometries and properties

	Geometries and boundary conditions		
	Unit	Basic model	Advanced model
Free length	m	15.00	
Fixed length	m	6.00	
Nodes per elements	nodes	6.00	
Real body weight soil	kN/m <sup>2</sup>	18.50	
Modelled body weight soil	kN/m <sup>2</sup>	9.20	
Radius borehole	m	0.11	
Radius after grouting	m	0.15	
Radius void free length	m	0.11	0.05
Height grout in free length	m	0.00	14.00
Radius model	m	5.00	3.00
Height model	m	25.00	
Radius application MLSM	m	0.50	0.35
Shear band	m	0.020	2 x 0.015
Coefficient for earth pressure at rest $K_0$	-	1.00	
Support conditions	Bottom boundary	Vertically + horizontally fixed	
	Right edge	Horizontally fixed	

## 4.2 Material parameters

The settings and material parameters for the used constitutive models are listed and explained in this section. The tendon is modelled linear-elastically in any case. Two different material models are used to simulate the behaviour of each soil and grout in order to determine their impact individually on the system and save computation effort. MLSM and HS model are employed for the soil and SC and MC model for the grout. The constitutive models are described in chapter 3.

### 4.2.1 Tendon

The material parameters of the tendon and geometries are listed in Tab. 4.4. Four strands are chosen to be integrated in one fixed length. As the tendon is behaving linear-elastically, the stress in the tendon has to be checked in each calculation and compared to the yield strength.

Tab. 4.4. Material parameters – tendon

Tendon – Reference SC / MC and FreeL SC / MC			
Parameter	Symbol	Unit	Value
Material model	-	-	LE
Young's modulus	$E_{tendon}$	kN/m <sup>2</sup>	195 000 000
Poisson's ratio	$\nu$	-	0.30
Single area strand	$A_{strand}$	m <sup>2</sup>	0.00015
Strands per fixed length	-	-	4
Total area 4 strands	$A_{strands}$	m <sup>2</sup>	0.0006
Radius continuum of 4 strands	$r_{strands}$	m	0.0140
Yield strength	$f_{yk}$	kN/m <sup>2</sup>	1 670 0
Force at yield point (4 strands)	$R_{p0.1k}$	kN	984

### 4.2.2 Grout

The grout is modelled with both Mohr-Coulomb and Shotcrete constitutive model in different calculations. The former saves calculation time but does not simulate the behaviour of the system as accurate as the latter. The material parameters chosen for the Mohr-Coulomb material model are listed in Tab. 4.5. The cohesion is determined using the friction angle  $\varphi'$  and the uniaxial compressive strength  $UCS$ , as pictured in Fig. 4.6.

Tab. 4.5. Material parameter grout body – Mohr-Coulomb model

Grout body – Mohr-Coulomb model – Reference MC and FreeL MC			
Parameter	Symbol	Unit	Value
Material model	-	-	MC
Young's modulus	$E$	kN/m <sup>2</sup>	30 000 000
Uniaxial compressive strength	$UCS$	kN/m <sup>2</sup>	25 000
Poisson's ratio	$\nu$	-	0.20
Cohesion	$c'_{ref}$	kN/m <sup>2</sup>	5 829
Friction angle	$\varphi'$	°	40
Dilatancy angle	$\psi$	°	0
Tension cut-off (tensile strength)	$TCO (\sigma_t)$	kN/m <sup>2</sup>	2 000

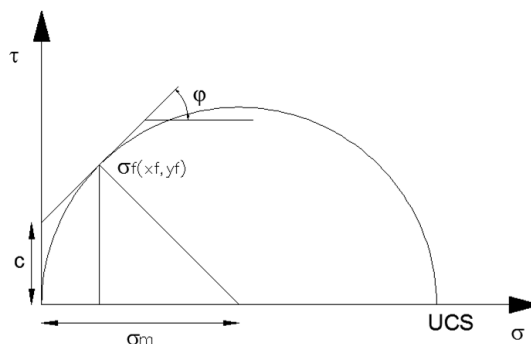


Fig. 4.6. Mohr-Coulomb failure line for concrete

Tab. 4.6 gives a full account of the input parameters for the Shotcrete model. As already mentioned in the model description, any kind of time dependency is neglected. Parameters number 8 to 18 are taken from Schädlich and Schweiger (2014 b) based on experimental data. The compressive fracture energy  $G_c$  is set to 8 kN/m in the basic model only, on which this parameter has no impact, and later

on changed to 50 kN/m according to the given recommendations in the advanced model. The impact of alterations of certain parameters are analysed in the next chapters.

Tab. 4.6. Material parameter grout body – Shotcrete model

Grout body - Shotcrete model – Reference SC and FreeL SC				
No	Parameter	Symbol	Unit	Value
1	Young's modulus at a shotcrete age of 28 days	$E_{28}$	kN/m <sup>2</sup>	30 000 000
2	Poisson's ratio	$\nu$	-	0.20
3	Uniaxial compressive strength	$f_c$	kN/m <sup>2</sup>	25 000
4	Ultimate uniaxial tensile strength	$f_t$	kN/m <sup>2</sup>	2 000
5	Dilatancy angle	$\psi$	°	0.00
6	Time dependency of elastic stiffness	$E_1/E_{28}$	-	1.00
7	Time dependency of strength	$f_{c,1}/f_{c,28}$	-	1.00
8	Normalized initially mobilised strength (compression)	$f_{c0,n}$	-	0.15
9	Normalized failure strength (compression)	$f_{cf,n}$	-	0.95
10	Normalized residual strength (compression)	$f_{cu,n}$	-	0.10
11-13	Uniaxial plastic failure strain at 1h, 8h, 24h	$\varepsilon_{cp}^P$	-	-0.0010
14	Fracture energy in compression	$G_{c,28}$	kN/m	8 / 50
15	Residual strength level	$f_{tu,n}$	-	0.05
16	Fracture energy in tension	$G_{t,28}$	kN/m	0.15
17	Equivalent length (if no regularization is used)	$L_{eq}$	m	-
18	Increase of $\varepsilon_{cp}$ with increase of $p'$	$a$	-	16.00
19	Maximum friction angle	$\phi^{max}$	°	40.00
20	Ratio between creep and elastic strains	$\phi^{cr}$	-	0.00
21	Time for 50% of creep strains	$t_{50}^{cr}$	d	0.00
22	Final shrinkage strain	$\varepsilon_{\infty}^{shr}$	-	0.00
23	Time for 50% of shrinkage strains	$t_{50}^{shr}$	d	0.00
24	Safety factor for compressive strength	$\gamma_{fc}$	-	1.00
25	Safety factor for tensile strength	$\gamma_{ft}$	-	1.00
26	Time for full hydration (usually 28 days)	$t_{hydr}$	d	0.00

### 4.2.3 Soil

The highly overconsolidated clay is modelled with both MLSM and HS model. The latter is applied in areas where no strain softening occurs in order to save calculation time. Thus, it has no interface to the shotcrete model. As this is where the focus is set on, the HS model plays only a minor role in the behaviour of the simulation model. Its input parameters are listed in Tab. 4.7.

The parameters for the soil stiffness and strength were taken from calibrations to triaxial tests of highly overconsolidated Brno clay, conducted by Miča et al. (2011). They were later verified during a back analysis of a deep excavation. Although the soil is highly overconsolidated with a pre-overburden pressure (POP) of 1 800 kN/m<sup>2</sup>, the coefficient of earth pressure at rest  $K_0$  is set to 1 for the given reasons in section 4.1. The critical state friction angle  $\phi'_{res}$  is employed in the HS model.

The relevant input parameters for the MLSM are listed in Tab. 4.8. The tangential modulus from oedometer test  $E_{oed,ref}$  in the HS model is more than twice as high as the value in the MLSM. The reason is the position of the Hvorslev surface, which is a function of the ratio between  $E_{ur,ref}$  and  $E_{oed,ref}$ .

Tab. 4.7. HS – parameters surrounding soil

Surrounding soil – HS – Reference SC / MC and FreeL SC / MC			
Parameter	Symbol	Unit	Value
Constitutional model	Model	-	Hardening Soil
Type of behaviour	Type	-	Drained
Secant modulus from triaxial test at reference pressure	$E_{50,ref}$	kN/m <sup>2</sup>	11 860
Tangential modulus from oedometer test at reference pressure	$E_{oed,ref}$	kN/m <sup>2</sup>	11 860
Unloading / reloading modulus at reference pressure	$E_{ur,ref}$	kN/m <sup>2</sup>	36 170
Reference pressure	$p_{ref}$	kN/m <sup>2</sup>	100
Poisson's ratio	$\nu$	-	0.20
Cohesion	$c'_{ref}$	kN/m <sup>2</sup>	6
Friction angle	$\varphi'_{res}$	°	20
Dilatancy angle	$\psi$	°	-
Stress dependency index	$m$	-	0.55
Earth pressure coefficient in normal consolidation	$K_{0,nc}$	-	0.66
Earth pressure at rest	$K_0$	-	1.00
Pre-overburden pressure	$POP$	kN/m <sup>2</sup>	1 800
Unit weight	$\gamma$	kN/m <sup>3</sup>	9.20

The Hvorslev model with regularisation is selected with the switch to activate model features  $switch_{HV}$ . This requires the input of the internal length for non-local regularisation  $L_{cal}$ . The determination of this value along with the softening parameter  $h_{soft}$  are explained in section 5.5, as they are mesh-dependent and cannot be calibrated at stress point level. The reason is the development of shear bands that cause inhomogeneity inside the sample. On the contrary, the shear hardening parameter  $A_{mat}$  can be calibrated to triaxial test results at stress point level with the PLAXIS SoilTest Tool.

The Hvorslev surface inclination  $\varphi_e$  is set to 16°, since its value is approximately 3° to 6° below the critical state friction angle  $\varphi_{res}$  (Schädlich 2012), which is 20° in this case. The earth pressure coefficient in normal compression  $K_{0,nc}$  is determined with  $1 - \sin(\varphi_{res})$ , incorporating the critical state friction angle  $\varphi_{res}$ .

The number of integration planes  $n_{cp}$  is set to 21 which is, besides 33, a recommended value (Schädlich 2012). Although a higher number of planes deliver a higher accuracy, the computational effort increases as well, which is the prevailing factor in such an extensive model. The switch for non-local weighting functions  $WF$  is selected to be 0, hence the Galavi weighting function is utilised, since it delivers good regularisation (Schädlich 2014). As more numerically stable results are obtained if the stiffness depends on the effective mean stress  $p'$ , the switch for stiffness dependence  $switch_{p/\sigma}$  is set to 0.

Tab. 4.8. MLSM – parameters Reference model

Soil proximity grout – MLSM - Reference SC / MC and FreeL SC / MC				
No	Parameter	Symbol	Unit	Value
1	Oedometric stiffness at reference pressure	$E_{oed,ref}$	kN/m <sup>2</sup>	5 425
2	Un/reloading stiffness at reference pressure	$E_{ur,ref}$	kN/m <sup>2</sup>	36 170
3	Reference pressure	$p_{ref}$	kN/m <sup>2</sup>	100
4	Power exponent for stress-dependency of stiffness	$m$	-	0.55
5	Poisson's ratio in un/reloading (isotropic)	$\nu'_{ur}$	-	0.20
6	Shear hardening parameter	$A_{mat}$	-	0.015
7	Switch to activate model features	$switch_{HV}$	-	1.00
14	Failure ratio	$R_f$	-	0.95
15	Earth pressure coefficient in normal consolidation	$K_{0,nc}$	-	0.66
16	Number of integration planes	$n_{CP}$	-	21
22	Switch for stiffness dependence	$switch_{p/\sigma}$	-	0
25	Hvorslev surface inclination	$\varphi_e$	°	16.0
26	Switch for non-local weighting functions	$WF$	-	0
32	Maximum substep size stress	$Stepsize$	kN/m <sup>2</sup>	5
34	Initial value of $\sigma_{nc}$	$\sigma_{nc0}$	kN/m <sup>2</sup>	-1 800
42	Critical state friction angle	$\varphi_{res}$	°	20
46	Internal length for non-local regularisation	$L_{cal}$	m	0.04
48	Maximum # stresspoints for non-local regularisation	$MaxPoint$	-	500
50	Softening parameter	$h_{soft}$	-	100
			$h_{soft}/L_{cal}$	2 500

## 5 Basic model computations

This chapter covers calculations of the basic model without grout in the free length. Sensitivity analyses are carried out in order to evaluate the model, the influence of individual parameters on the whole system and the overall behaviour. Hence, a series of models are created and compared to a so-called “Reference model” and also to each other.

The models *Reference MC* and *Reference SC* form the foundation for the sensitivity analyses in the basic model conducted in this chapter. Their difference is the constitutive model employed for the grout (MC and SC model) in order to determine their impact and separate it from the MLSM. The denotation of the models gives an indication of the used constitutive model for the grout. Tab. 5.1 gives an overview of the used material models in these two simulation models. Their material parameters applied in the calculations are listed and explained in section 4.2. The alterations made in the further performed analyses are pointed out individually within their description.

Tab. 5.1. Reference models: employed material models

	<i>Reference SC</i>		<i>Reference MC</i>	
	Abbreviation	Material model	Abbreviation	Material model
Grout	SC	Shotcrete model	MC	Mohr-Coulomb model
Proximity grout	MLSM	Multilaminate soil model		
Surrounding soil	HS	Hardening soil model		
Tendon	LE	Linear elastic		

### 5.1 Overview of performed analyses

This section gives an overview of the analyses performed in this chapter. Numerical analyses on the models without grout in the free length are conducted and the behaviour of the overall system is examined. The investigated models are loaded till failure of the anchor, indicated by the state when all stress points along the fixed length are in residual state. Thus, the post-peak behaviour is captured as well.

The following analyses have in common that the load-displacement curve at the top of the fixed length is taken as reference, since this is the interface to the field as the anchor load tests result in the same. Furthermore, it is a key indicator of the stiffness and strength of the system as a whole. The peak of this curve, known as the ultimate bearing capacity of the anchor, and the respective displacement are the prevailing factors in the comparison. Moreover, the shear stress distribution of several load steps in the soil is plotted along the grout body in order to gain an additional impression of the progressive failure and influences of various changes in the model upon it. In each case, the cross section for this analysis is at a distance of 1 cm to the surface of the grout body with the intention of capturing the most stress points. In general, the analyses are focussed on the grout – ground interface, since this is the area of the prevailing failure mechanism.

Although it is clear that superposition cannot be applied in the present, highly non-linear case, the influence of different variations in geometries and parameters are analysed separately. The following four main objectives are the incentives for the analyses:

- **Evaluation of the geometries / mesh:**  
Especially the slender geometries embedded in a comparatively long simulation model and the application of the MLSM place high demands on the mesh quality.
- **Reduction in calculation time:**  
The MLSM in combination with the SC model take relatively long computation time. Hence, effort is made to optimize the calculation process, especially with regard to larger models.
- **Assessment of the behaviour and the interaction of the used material models:**  
Since the material models are highly advanced and the system's response is non-linear, the behaviour and the interaction of the overall model have to be thoroughly evaluated. A qualitative assessment is conducted by means of comparison with expectations, laboratory and field tests.
- **Range investigation:**  
Determining the influence of single parameters on the whole system, is the main objective of this basic model. Since the material models feature a relatively large number of input parameters, there is a high amount of possible combinations. A thorough analysis is very time consuming, thus the list of analyses is restricted to the once that are estimated to be the most influencing and imply the highest uncertainties.

All these specified aims have in common that they pursue the target of rating the impact of modifications.

Tab. 5.2 gives an overview of the conducted analyses. The name of the models has added either SC or MC, indicating the material model used for the grout and therefore implying the respective reference model. Moreover, there is an extra column for this reason. Each conducted model is compared to the respective reference model in terms of the changed input parameters for the analysis, giving the value of the reference model and the changed one. The analyses are divided in the following eight main classifications:

- **Reference:**  
Contains the basic models for the comparison to the other models.
- **Mesh evaluation and computation:**  
A mesh sensitivity analysis is conducted and the impact of the computation process is analysed.
- **MLSM:**  
Softening parameters are outlined and the general impact of the model is demonstrated.

- **SC:**

The overall influence of this material model on the calculation is presented, additional analyses are integrated in other categories.

- **Geometry:**

Impacts of the chosen geometries are evaluated.

Tab. 5.2. Basic model: overview of performed analyses and changed parameters

Category	Model name	Grout	Soil	Description/ Parameter changed	Value Reference	New value				
Reference	Reference SC	SC	MLSM	-	-	-				
	Reference MC	MC	MLSM	-	-	-				
Mesh & calculation	Fine mesh MC	MC	MLSM	Number of elements	3 917	15 889				
	Fine mesh SC/HS	SC	HS	Number of elements	3 917	14 516				
	15-noded MC	MC	MLSM	Nodes per element	6	15				
MLSM	<i>hsoft</i> 70/ <i>Lcal</i> 0.07 (1000) MC	MC	MLSM	<i>hsoft</i> , <i>Lcal</i> ; <i>hsoft</i> / <i>Lcal</i>	-	m	100 / 0.04	2500	70 / 0.07	1 000
	<i>hsoft</i> 70/ <i>Lcal</i> 0.04 (1750) MC	MC	MLSM						70 / 0.04	1 750
	<i>hsoft</i> 144/ <i>Lcal</i> 0.04 (3600) MC	MC	MLSM						144 / 0.04	3 600
	<i>hsoft</i> 144/ <i>Lcal</i> 0.02 (7200) MC	MC	MLSM						144 / 0.02	7 200
	<i>hsoft</i> 72/ <i>Lcal</i> 0.02 (3600) MC	MC	MLSM						72 / 0.02	3 600
	<i>hsoft</i> 500 MC	MC	MLSM						500 / 0.04	12 500
	No Regularization SC	SC	MLSM	<i>switch<sub>HV</sub></i>	-	1	2			
	SC/HS	SC	HS	HS instead of MLSM, SC	-	-				
	MC/HS	MC	HS	HS instead of MLSM, MC	-	-				
	<i>E soil low</i> MC	MC	MLSM	<i>E<sub>oed,ref</sub></i> , <i>E<sub>50,ref</sub></i> , <i>E<sub>ur,ref</sub></i>	100%	20%				
	<i>E soil low hsoft</i> 500 MC	MC	MLSM		100%	20%				
	Dilatancy 1° MC	MC	MLSM	<i>ψ</i>	°	0	1			
Dilatancy 3° - DCO 0.6 MC	MC	MLSM	<i>ψ</i> / DCO	°	0	100	3	0.6		
SC	<i>G<sub>t</sub></i> 0.5 SC	SC	MLSM	Fracture energy <i>G<sub>t</sub></i>	kN/m	0.15	0.5			
	<i>E low</i> SC	SC	MLSM	SC Stiffness <i>E<sub>2B</sub></i>	kN/m <sup>2</sup>	30 000 000	20 000 000			
Geometry	MLSM radius MC	MC	MLSM	-	m	0.5	1.2			
	Radius model MC	MC	MLSM	-	m	5	2.5			

## 5.2 Computation

Thorough consideration should be given to the computation settings, especially in the calculations combining the two user-defined soil models. The iteration procedure settings are listed in Tab. 5.3. The range set by the maximum and minimum number of iterations is widened, because it prevents up- and downscaling of the step size. This results in a smoother load-displacement curve and fewer load steps. Furthermore, a large step size creates higher out-of-balance forces, which take more computational effort to reach the tolerance again. The Arc-length control option must be deactivated, since both MLSM and SC model generate declines in the load-displacement curves at different load levels. It can be traced back to local failure mechanisms due to strain softening, such as cracks simulated by the SC model. These local failures are overcome after several unloading steps. Meanwhile, the displacement is either kept the same or slightly increased. Since the load is reduced and the stress is redistributed, the number of stress points in failure decreases. Reducing the maximum load fraction per step to 10 % of the total load applied in the particular phase decreases the size of the unloading steps in many cases, because the initial steps are smaller.

Tab. 5.3. Iteration procedure settings

Iteration procedure parameters	
Max. number of iterations	60
Desired min. number of iterations	5
Desired max. number of iterations	55
Max. load fraction per step	0.10
Tolerance	1 %
Arc-length control type	Off
Max steps	5 000

The following calculation phases are set:

- Initial phase:  $K_0$ -procedure
- Initialize MLSM
- Initialize tendon and shotcrete
- Nil step
- Several phases of prescribed displacements of 0.4 cm each

The displacements are reset to zero before the anchor loading starts.

### 5.3 Mesh sensitivity analysis

The mesh also has a significant impact on the calculation time and its accuracy. High demands are placed on mesh quality by using slender continuum elements. However, despite the computer capabilities available these days, the mesh fineness required by this approach demands a trade-off between calculation times and the validity of information on local behaviour, especially when taken into account the amount of studies. The main attributes of the compared meshes are listed in Tab. 5.4.

Tab. 5.4. Basic model: mesh sensitivity analysis

Mesh sensitivity analysis			
Model	Unit	Reference model	Fine mesh
Number of elements	-	3 917	15 889
Average element size	m	0.1786	0.0887

The mesh fineness in the clusters of the two material models, SC and MLSM, are separately analysed. Thus, the other constitutive model is replaced by the MC or the HS model with the respective parameters as given in section 4.2. The mesh was refined up to the maximum with the result of approximately 3 % deviation with the MLSM and 0.5 % with the SC model. Moreover, a calculation with 15-noded elements with the same mesh as in the reference model and the MLSM was performed, which gives even lower deviations. As a result, the mesh is sufficiently fine (see Tab. 5.5). The reason for the high difference in load bearing capacity between the two analyses of the mesh sensitivity is the different approach in the models used for the soil, HS and MLSM. This issue is discussed in section 5.4.

Tab. 5.5. Results – mesh sensitivity analysis

MC/MLSM mesh sensitivity				
Model	Displacement [m]	Difference	Bearing capacity [kN]	Difference
<i>Fine mesh MC</i>	0.098	-	664	-
<i>Reference MC</i>	0.102	+3.8 %	683	+2.8 %
<i>15-noded MC</i>	0.096	-2.6 %	651	-2.1 %
SC/HS mesh sensitivity				
SC/HS	Displacement [m]	Difference	Bearing capacity [kN]	Difference
<i>SC/HS</i>	0.0093	-	396	-
<i>Fine mesh SC/HS</i>	0.0093	±0.0%	394	-0.5%

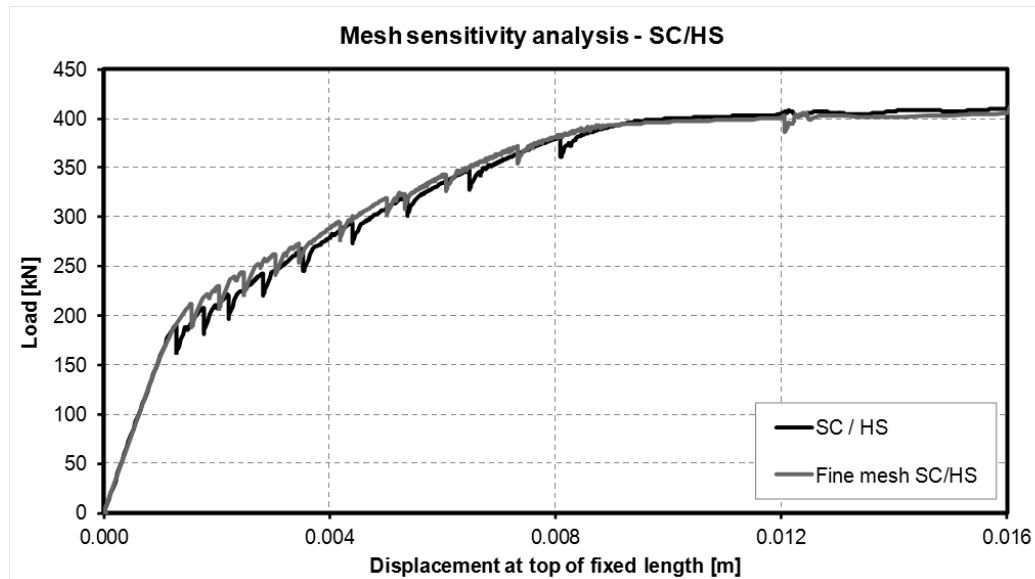


Fig. 5.1. Mesh sensitivity SC: comparison of load-displacement curves

The mesh sensitivity analysis of the SC model shows the same amount of unloading steps with little offset in their occurrence in the course of load application, as can be seen in Fig. 5.1. Their meaning is discussed in section 5.7.

The used mesh for the models without grout in the free length is shown in Fig. 5.2a and the fine mesh in Fig. 5.2b. The mesh sensitivity analysis is performed separately in section 6.1. The two horizontal lines separate the area of application of pressure grouting, as described in section 6.9.

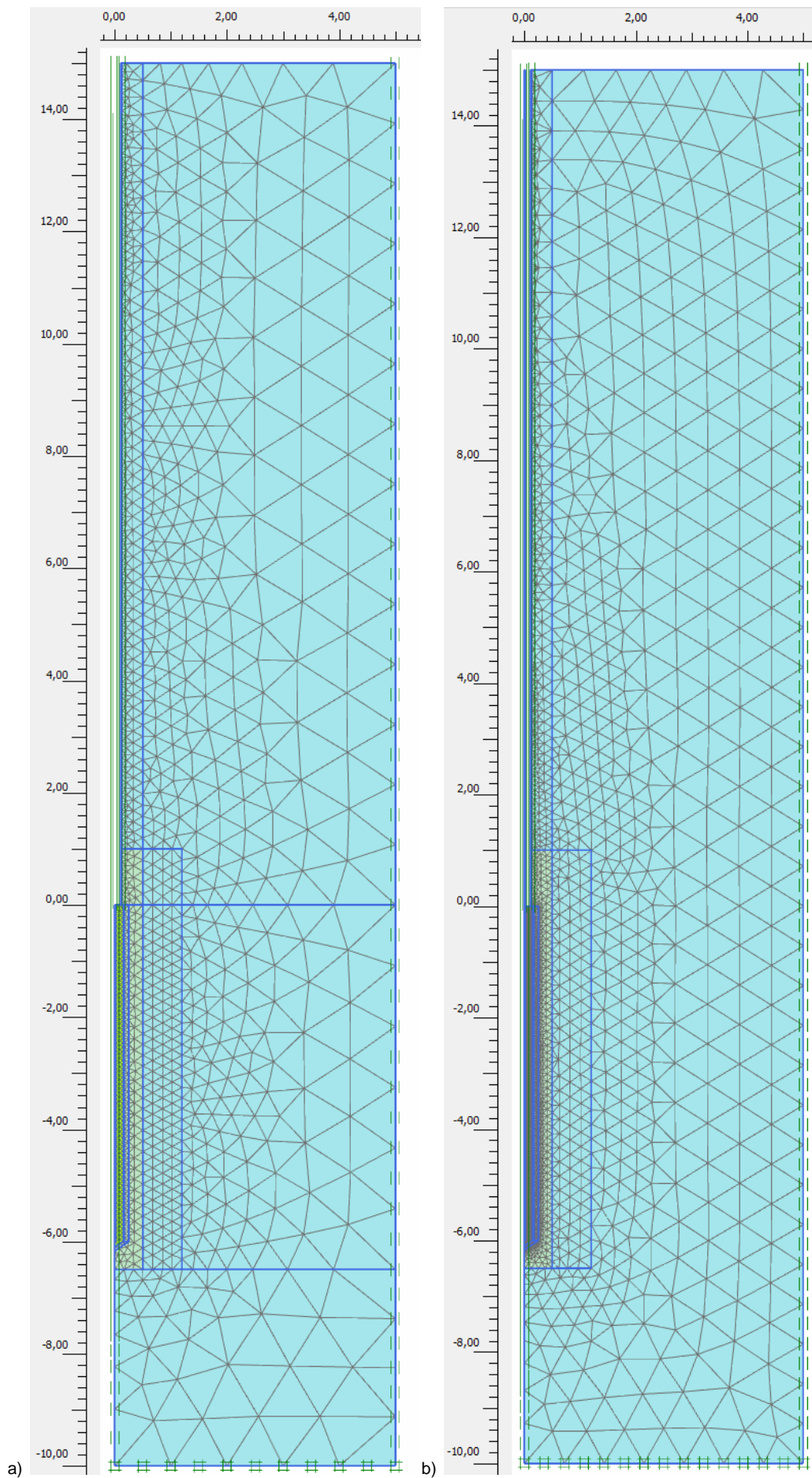


Fig. 5.2. FE-mesh: a) used mesh, b) fine mesh

A detail of the mesh used for the model *Reference MC* at the top of the fixed length is shown in Fig. 5.3a. The models *Reference SC*, *Reference MC* and all models based on these, employ this mesh. In comparison, the refined mesh of the model *Fine mesh MC* is shown in Fig. 5.3b.

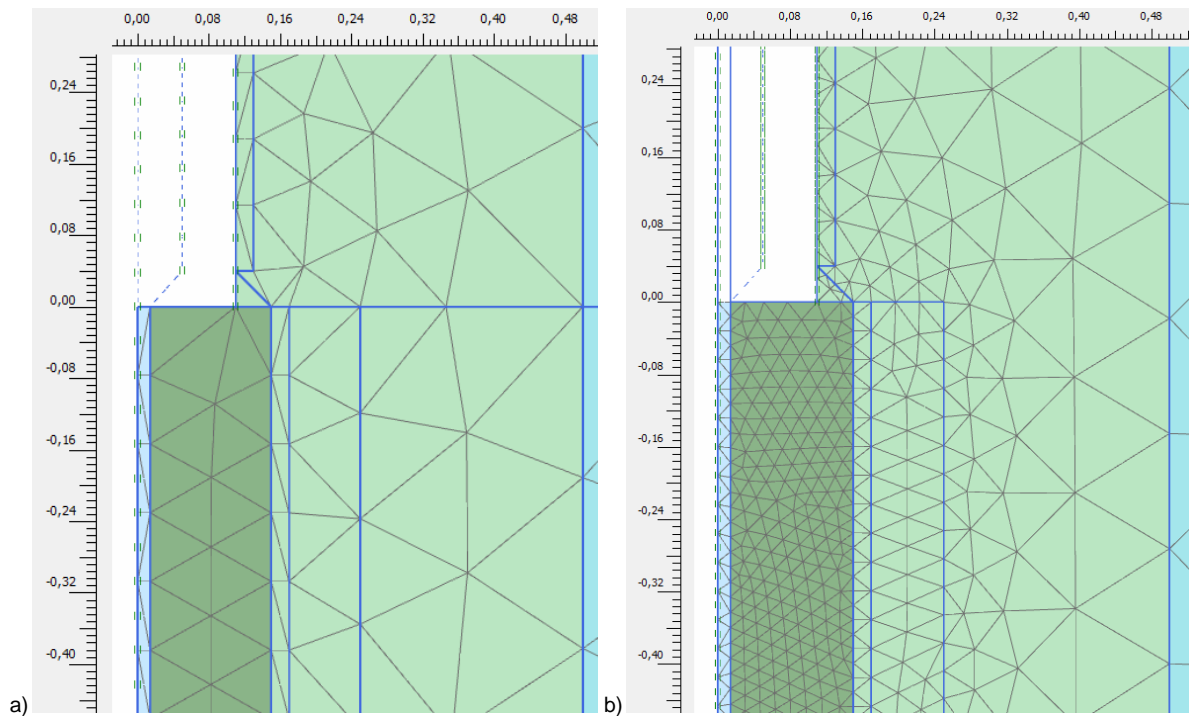


Fig. 5.3. Comparison of different mesh fineness: a) *Reference MC*, b) *Fine mesh MC*

## 5.4 Reference model (MC)

The *Reference MC* model represents a basis for further analyses. It features the geometries without grout in the free length, described in section 4.1, and the parameters listed in section 4.2. The MC model is used as constitutive model for the grout. This reference model is analysed first in order to compare the alterations of further models afterwards. Unless otherwise stated, all analyses in this section are obtained from *Reference MC*.

The effective principal stresses in the soil and the grout are shown separately in Fig. 5.4. The initial, isotropic stress state of the soil is changed by the applied shear stress. Peak stresses occur in the soil at top of the fixed length as compressive force is imposed on the soil in this area. The stress peak develops in the grout in the adjacent area. Apart from that, principal stresses are evenly distributed especially when compared to those occurring with the application of the SC model at the peak of the load-displacement curve, which can be compared in Fig. 5.26c.

The shear stress  $\tau_{mob}$  along the fixed length at different anchor load levels is illustrated in Fig. 5.5a. The curves are named after their respective displacement at top of fixed length. The reason is the post-peak load decline, which is why the same anchor load can occur more than once in the load-displacement curve. The selected load levels are delineated with dotted lines in Fig. 5.8. Integrating these curves of shear stress results in a slightly lower value than the total anchor force in the respective load level, since the soil on top of the fixed length between the borehole diameter and the

grouted diameter takes up load as well. The lowest represented load level of 345 kN at a displacement of 0.4 cm shows an increase in shear stress at the proximal and the distal end of the fixed length. This behaviour has already been examined e.g. by Evangelista and Sapio (1978) and Zong-Ze et al. (1995) in experiments.

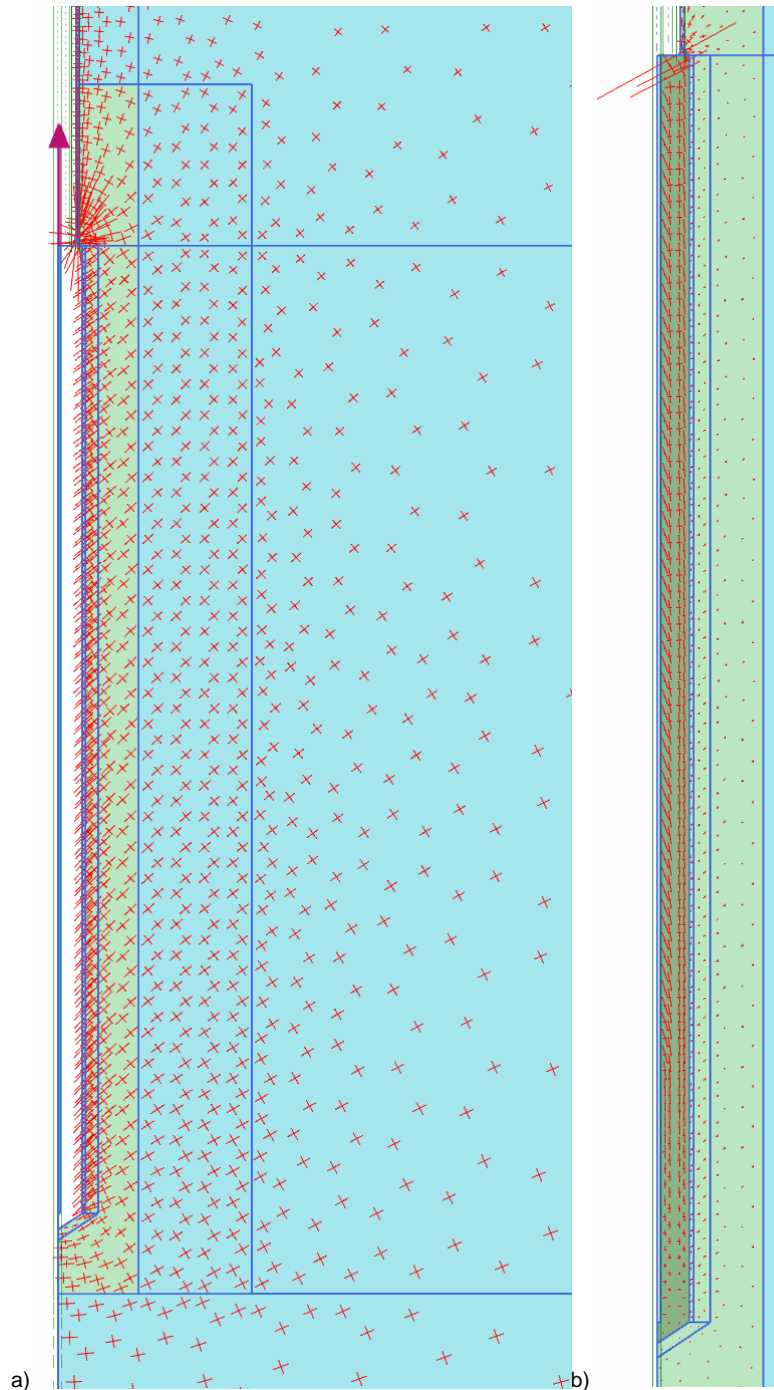


Fig. 5.4. Effective principal stresses without grout in the free length: a) along grout, b) in the grout modelled with MC

The peak at the top of the fixed length is the start of the progressive failure, which can be seen in the other two load levels in Fig. 5.5a. When reaching the Hvorslev surface, softening is initiated and thus, along with the propagation of the failure points, the reduction of the pre-consolidation pressure evolves as well. Softening has already started at a load of 345 kN, indicated by the decrease in shear stress at the top. High oscillations occur when the soil softens, because the stress points taken into

account for these curves are at different distances to the grout (see also Fig. 5.6). Softening progresses further to the bottom till failure of the anchor is reached. Since there is also a stress peak at the end of the fixed length, softening starts there as well. At a displacement of 1.6 cm, the peak load is reached, although not all of the stress points along the fixed length are in residual state. However, the anchor cannot take up more load. Fig. 5.5b shows the stress acting perpendicular to the grout surface at the same load levels. The reason for its increase along with load progression is dilatant behaviour of the highly overconsolidated soil, which is explained in section 5.6.

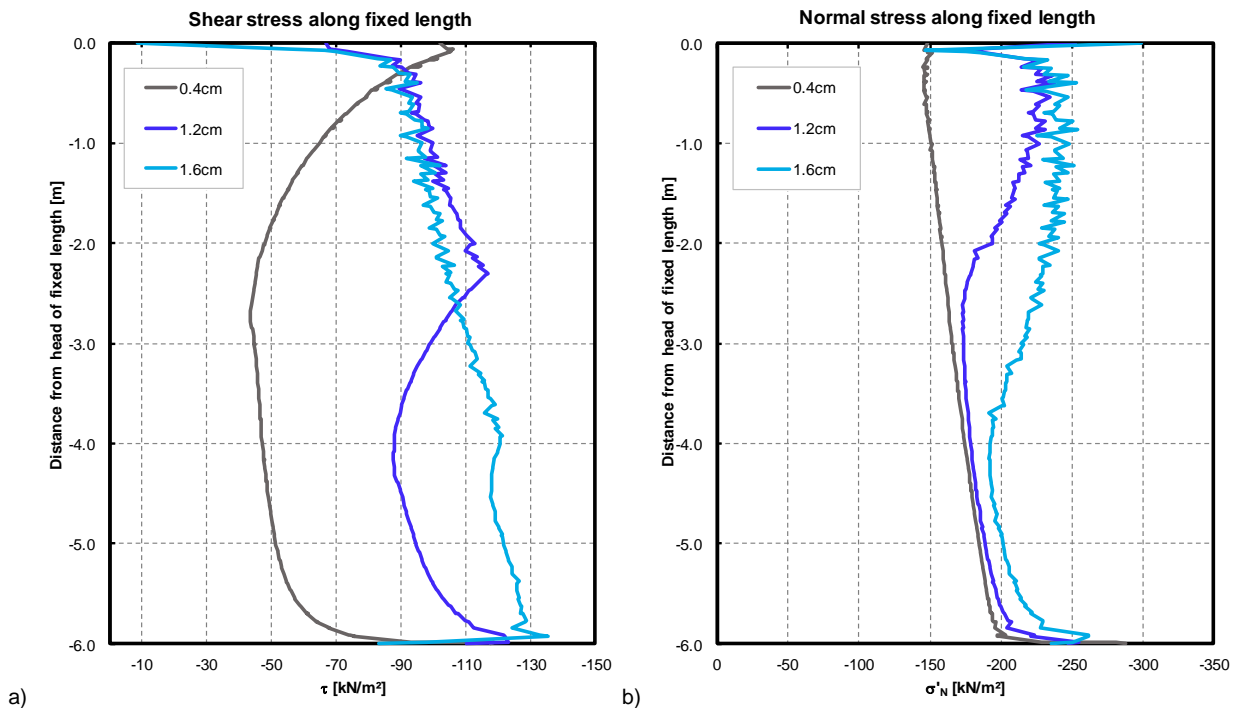


Fig. 5.5. Reference MC: stress along fixed length at different load levels and cross-sections: a) shear stress, b) normal stress

The influence of the location of the cross-section for the analysis of the shear stress and result smoothing conducted by PLAXIS is evaluated in Fig. 5.6 for the load level at a displacement of 1.2 cm. The notation of the curves indicates the distance to the grout body. In general, the curves with result smoothing at a distance of 1 cm show the smallest oscillations, which is why the analyses are conducted that way unless otherwise stated.

The mobilised friction angle  $\varphi'_{mob}$  along the fixed length at different displacements is calculated according to the Mohr-Coulomb failure criterion (see Equ. (5-1)) and displayed in Fig. 5.7. It must be noted that this equation and the calculated angle does neither describe the location of the Hvorslev surface nor its friction angle. This analysis is conducted at a distance to the grout of 3 mm without result smoothing, as it distorts the results otherwise. The friction angle reaches a peak value of approximately  $32^\circ$ . It is worth mentioning that this is no user input but an outcome of the MLSM. The soil next to the grout is completely softened to the normally consolidated state at the end of the load-displacement curve, as the input value for the critical state friction angle  $\varphi'_{res}$  of  $20^\circ$  is reached.

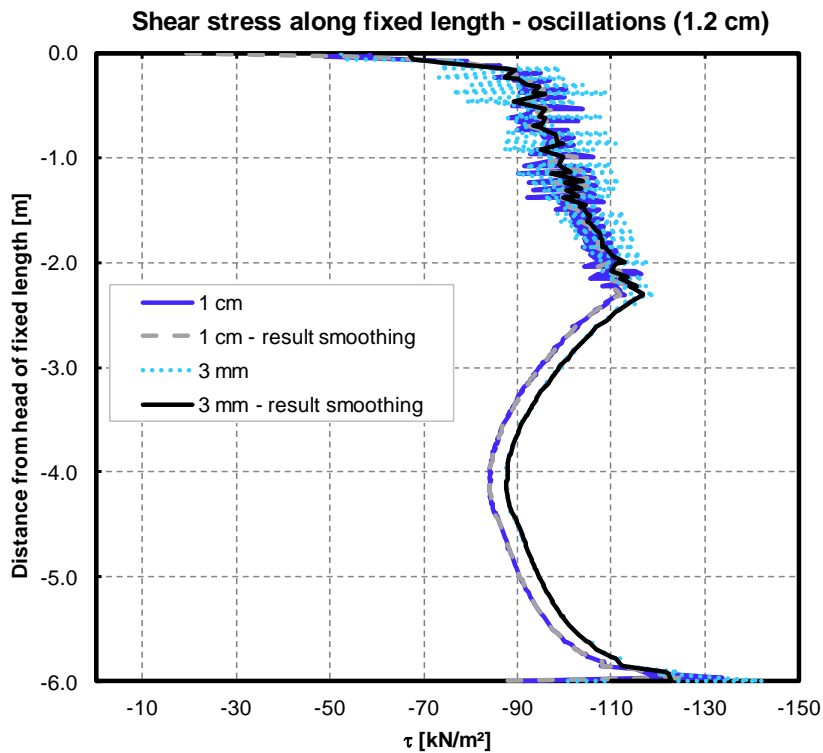


Fig. 5.6. Oscillations

$$\tan(\varphi'_{\text{mob}}) = \frac{\tau_{\text{mob}} - c'}{\sigma'_N} \quad (5-1)$$

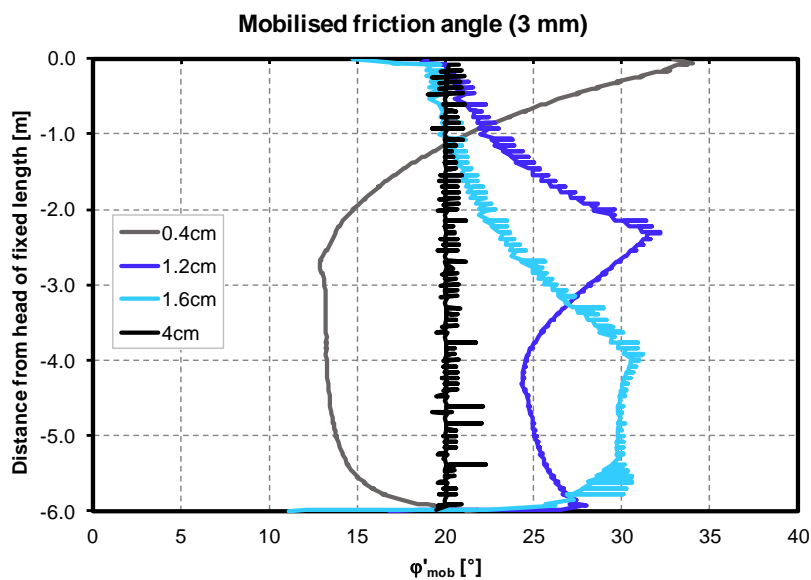


Fig. 5.7. Reference MC: Mobilised friction angle along fixed length in a cross-section at a distance of 3 mm to the grout body

Fig. 5.8 shows the load displacement curve of the model *Reference MC* with marked load levels for the analyses in this section. This curve differs from those obtained from anchor load tests, since the reference point for the displacement is at the top of the fixed length, thus not capturing the strain of the tendon in the free length. The post-peak behaviour is discussed in the following sections. The force at yield point of the tendon, as specified in Tab. 4.4, is not reached in this calculation.

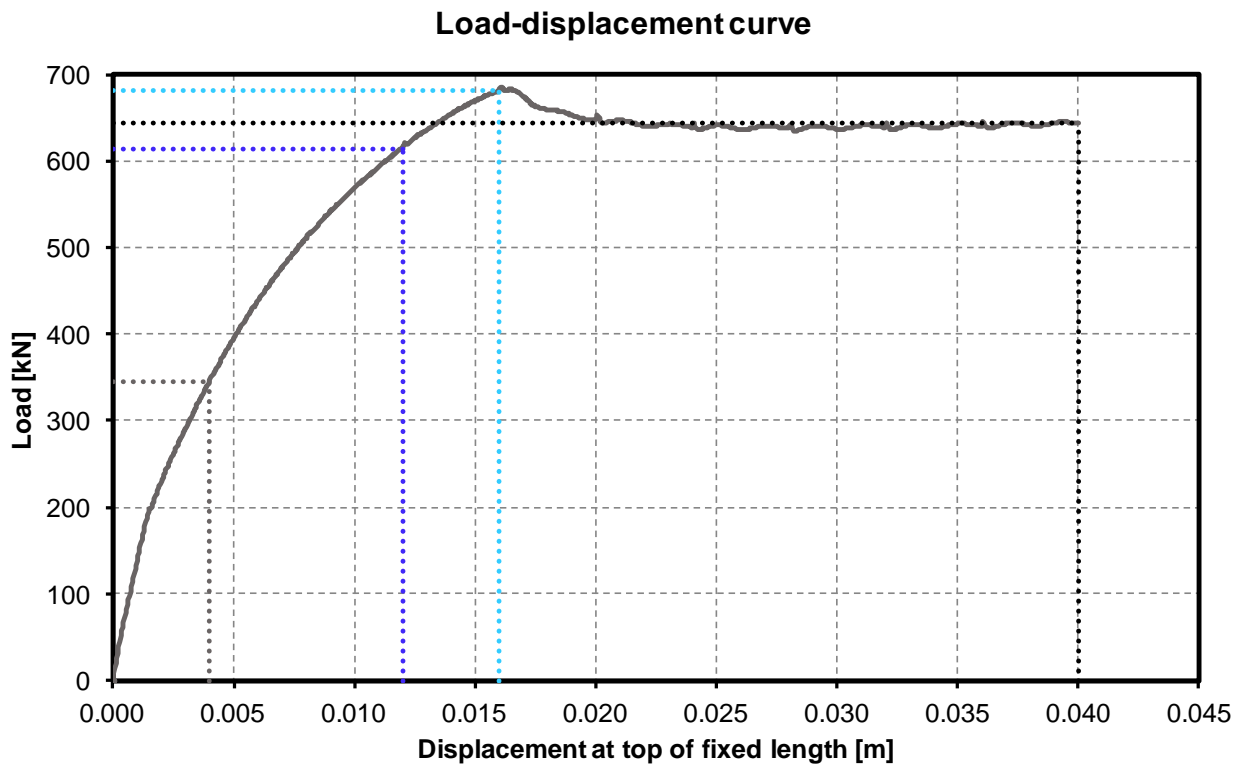


Fig. 5.8. Reference MC: load-displacement curve at top of fixed length (continuous) and load levels for Fig. 5.5 (dotted)

Several points in the surrounding soil of the grout with the MLSM are selected in order to compare the stress and strain behaviour at the proximal and distal end and the centre of the fixed length. Their coordinates are listed in Tab. 5.6. The origin of ordinates is located in the axis of symmetry at the head of the fixed length (see Fig. 4.3). In addition, the coordinates of a cross-section are specified, which is at the elevation of the points at the proximal end of the fixed length to a radius of 60 cm to the axis Y, thus being perpendicular to the fixed length. Those points and the cross-section are illustrated in Fig. 5.9.

It is worth mentioning that whenever stresses of the MLSM are plotted, they are in terms of macroscopic stresses corresponding to integration of the stress states in the local planes. The response to stresses in this particular case is almost entirely acting on one particular plane. Thus, the representations are attenuated by the other planes, which are staying almost the same.

Tab. 5.6. Location of selected stress points and cross-section for comparison

Point		x	y
TOP	K	0.15	-0.10
	L	0.17	-0.09
CENTRE	U	0.15	-3.10
BOTTOM	V	0.15	-5.72
Cross-section		0.15	-0.10
		0.60	-0.10

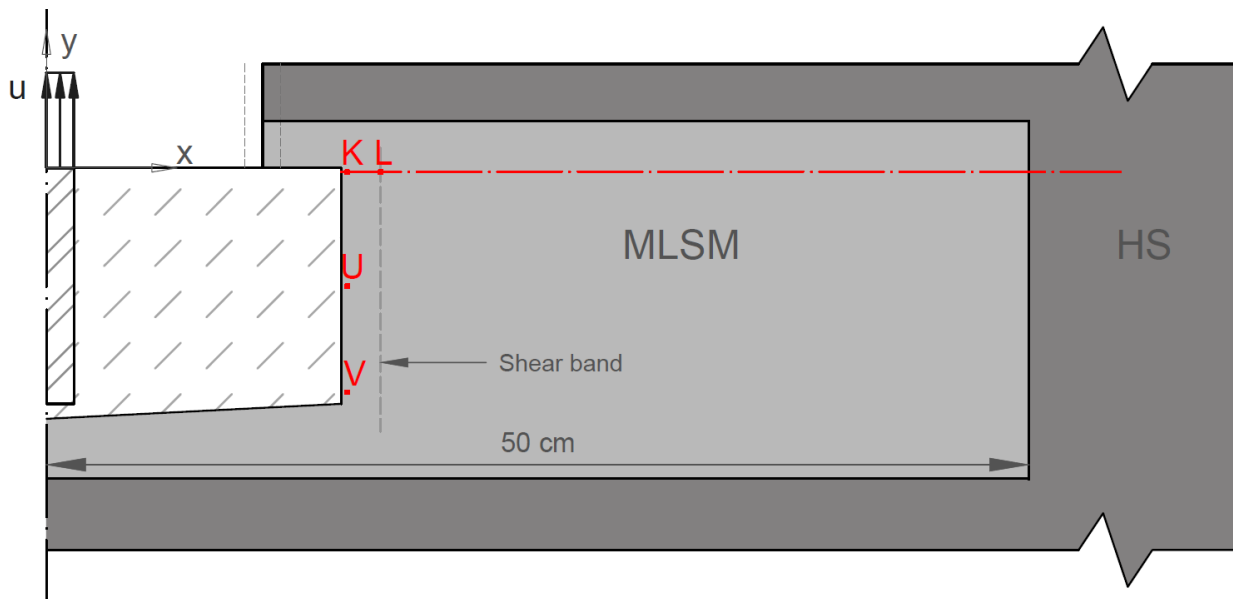


Fig. 5.9. Points and cross-section for analysis

The shear stress in the soil in point K at top of the fixed length is analysed in Fig. 5.10a. The mobilised shear stress  $\tau_{mob}$  is plotted against the displacement at top of the fixed length, showing a mobilisation till the Hvorslev surface, at which point the shear strength is reached. Subsequently, the shear stress decreases, because softening starts in this point. The corresponding volumetric and shear strain behaviour is represented in the graph below (see Fig. 5.10c). The volumetric strain acts almost exclusively in the direction of axis X, which is analysed in detail in section 5.6. As no relative displacement between grout and soil is possible in this model and nearly all of the displacement occurs in the defined shear band, the shear strain in point K is extremely high. This is demonstrated in Fig. 5.10d, showing the displacements at different load levels along the defined cross-section. The mobilised shear stress  $\tau_{mob}$ , which is basically equal to the shear stress  $\sigma_{xy}$  acting on global plane X and pointing in direction Y, vs. the shear strain  $\gamma_{xy}$  are plotted in Fig. 5.10d.

Fig. 5.10b shows the mobilised shear stress  $\tau_{mob}$  along the cross-section. The peak value at a displacement of 0.4 cm corresponds to the value at the peak of the mobilised shear stress in point K. Subsequently, the shear stress declines till the residual state, which is demonstrated by the mobilised shear stress at a displacement of 4 cm at the top of the fixed length. Although it has already reached this state in the displayed curve and is supposed to stay at the same value thereafter, the shear stress still declines with further displacement of the fixed length. After point K has reached the peak value, the surrounding soil mobilises further shear stress.

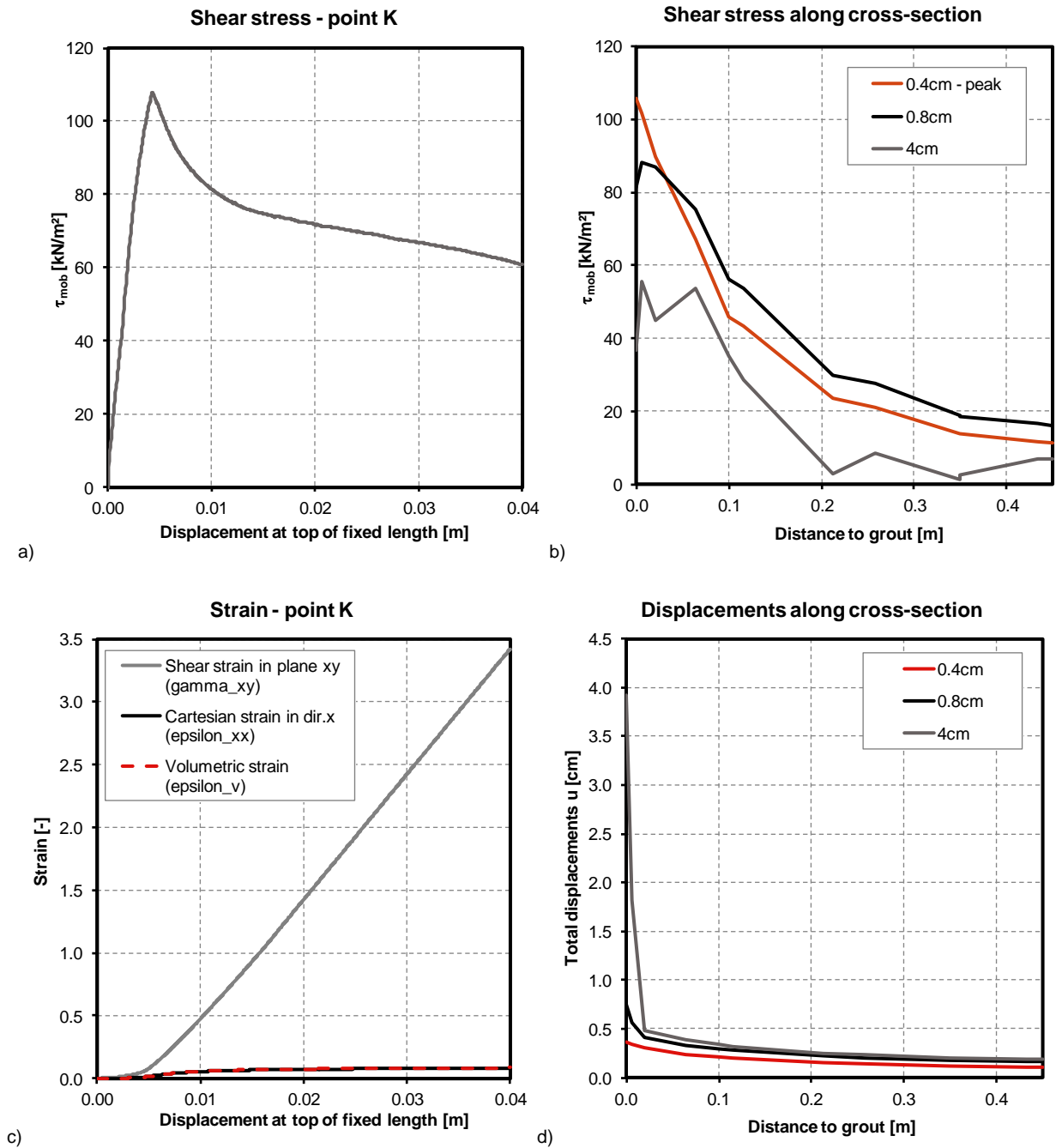


Fig. 5.10. *Reference MC*: stress-strain behaviour at point K: a) mobilised shear stress vs. displacement at top of fixed length, b) shear stress in section perpendicular to grout body at point K, c) volumetric and shear strain vs. displacement at top of fixed length, d) displacements along cross-section

As anticipated, the points next to the centre and the bottom of the fixed length reach the peak later in the loading procedure and exhibit slightly higher shear strength (see Fig. 5.11). Those points have already reached the residual value of the shear strength, indicated by the flattened curve. Point L is a little further away from the grout body than point K, thus having a slightly lower mobilised peak shear stress.

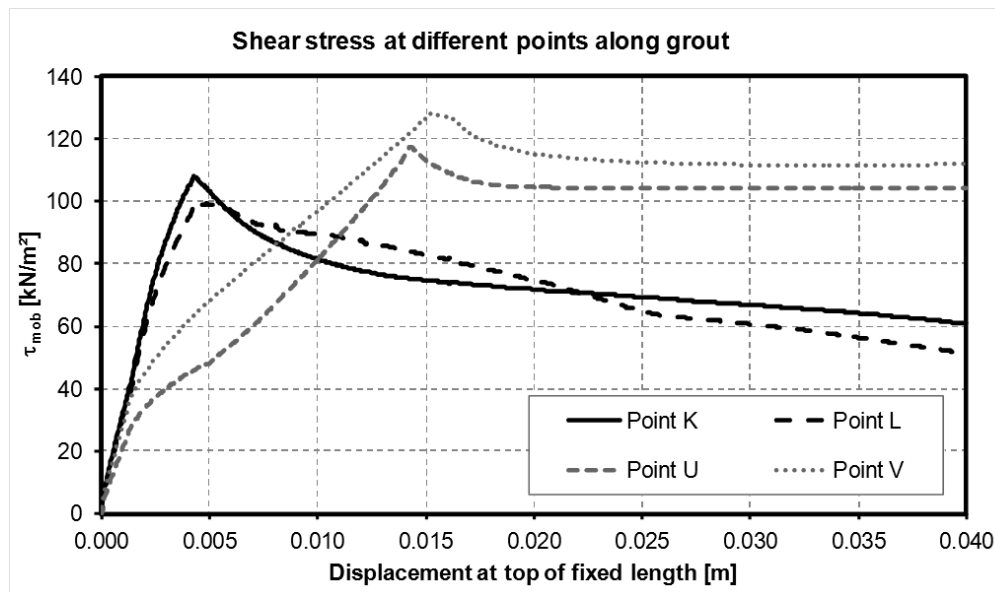


Fig. 5.11. *Reference MC*: Comparison of the shear stress vs. displacement at top of fixed length in the soil: top (K, L), centre (U) and bottom (V) of the fixed length

## 5.5 Softening – MLSM

As already mentioned, the softening parameters necessary for the MLSM cannot be calibrated at stress point level. Therefore, a study on the effects of these parameters is performed on the model itself instead of calibrating them to triaxial test data in a three-dimensional simulation of a triaxial test.

As can be seen from Fig. 5.3a, an additional line, parallel to the grout, is arranged at a distance of 2 cm in order to determine the shear band and an even distribution of elements within this area. Therefore, the element edges normal and perpendicular to the shear band are 2 cm and 7 cm, respectively. This is an acceptable compromise between accuracy and calculation time, as already demonstrated in section 5.3.

In the applied Hvorslev model with regularisation, softening is governed by the ratio of the internal length for non-local regularisation  $L_{cal}$  and the softening parameter  $h_{soft}$ . The former determines a domain which is considered during the regularisation and depends on the mesh. Galavi (2007) recommends setting it equal to or greater than the element size. Furthermore, the number of stress points in non-local regularisation, which can be obtained from a state variable in PLAXIS output, is suggested to be greater than 100. Thus, smaller values of  $L_{cal}$  result in faster softening, as strain regularisation is confined to stress points closer to the shear band.

The softening parameter  $h_{soft}$  coupled with the internal length  $L_{cal}$  determine strain softening. Higher values result in faster reduction of the pre-consolidation pressure  $\sigma'_{nc}$ . As a result, less deviatoric stress can be mobilized.

In order to evaluate the effect of these softening parameters on the simulation of the anchor, several variations of them are calculated and compared hereafter. The softening parameters are modified in the model without grout in the free length and the MC model for the grout (*Reference MC*) in this comparison. In addition, the reference model using the SC model (*Reference SC*), the 15-noded

elements model (*15-noded MC*) and *Fine mesh MC* are compared. Tab. 5.7 gives a comprehensive account of the input parameters and the results.

The load-displacement curves of the reference model (*Reference MC*) and the one with the highest softening ratio (*hsoft 500 MC*) are shown in Fig. 5.12. The only difference in terms of input values between them is the softening parameter  $h_{soft}$ , which is increased by 5. This decreases the ultimate load bearing capacity by 15 %. The sharper decline in the stress-strain behaviour (see Fig. 5.13) has the same impact on the post-peak load-displacement curve as well. The two presented curves do not have the same residual bearing capacity, although they feature the same critical state friction angle  $\varphi_{res}$ .

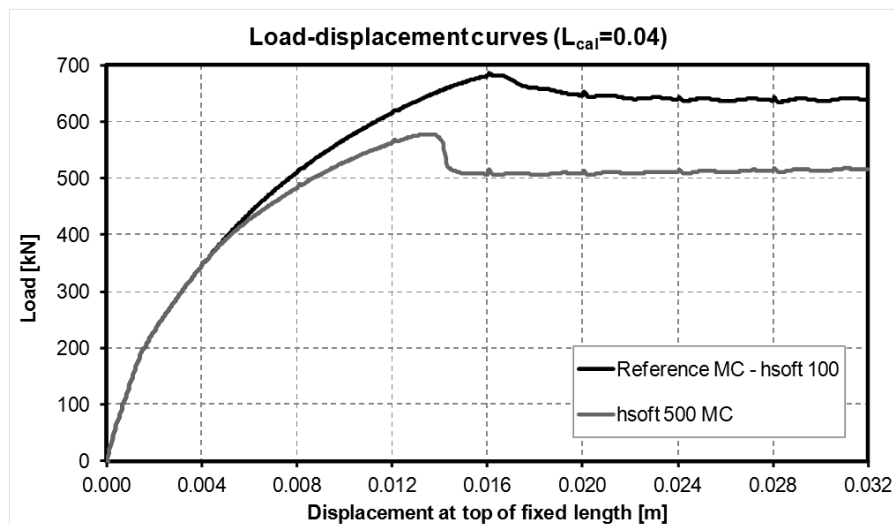


Fig. 5.12. Comparison of load-displacement curves

Within softening ratios  $h_{soft} / L_{cal}$  of 1 000 to 12 500, the ultimate bearing capacity ranges from 579 kN to 711 kN, which is an increase of 23 % (cf. Tab. 5.7). It is valid that the higher this ratio, the lower is the ultimate bearing capacity  $F_{max}$  and the higher the displacement at failure  $u_{max}$ . Still, the same softening ratio, but different values, does not result in exactly the same bearing capacity, because the mesh stays the same and a different number of stress points is taken into account for the non-local regularisation. In any case, the recommended number of stress points for non-local regularisation of 100 is not reached in a cross-section right next to the grout.

The comparison of the deviatoric stress  $q$  of the local point K in the shear band against the shear strain  $\gamma_{xy}$  shows the influence of different softening parameters (see Fig. 5.13). The higher the softening ratio, the higher the decrease in deviatoric stress from the peak value  $q_{max}$  to the residual value at failure of the anchor  $q_{res}$ . The decrease varies from 13 % to 63 %, which is listed in Tab. 5.7.

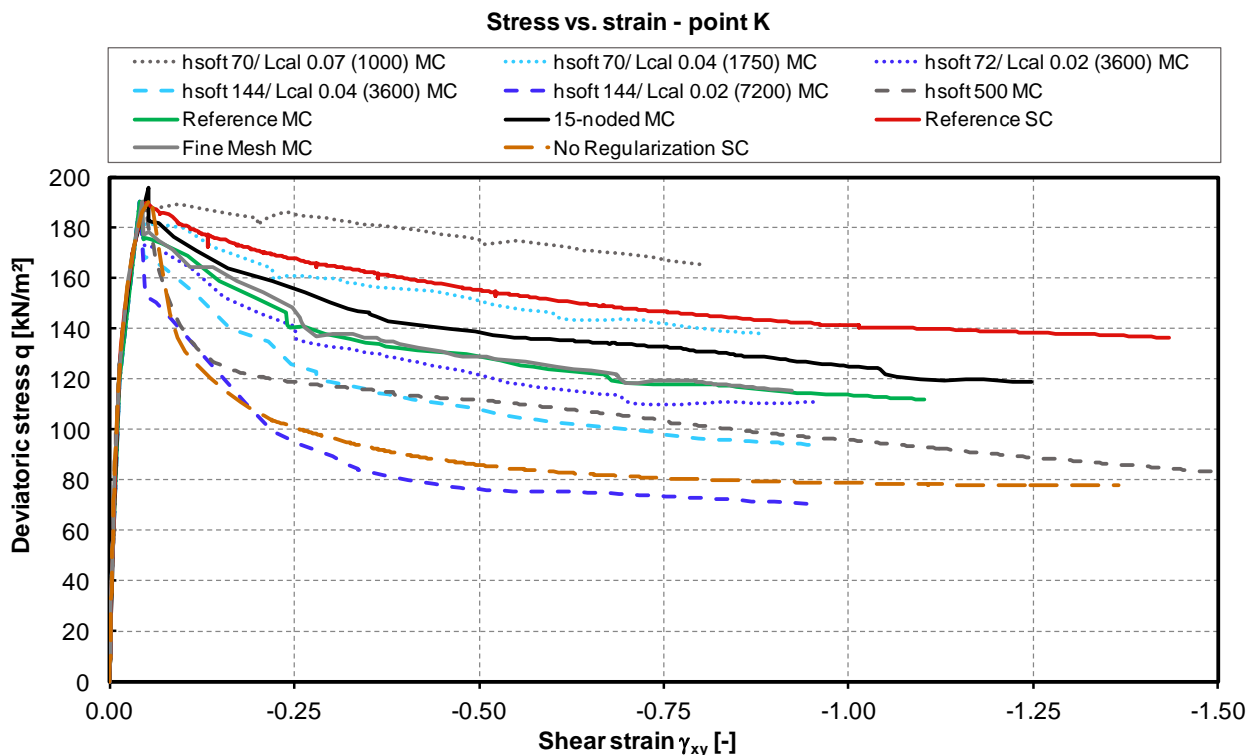


Fig. 5.13. Softening behaviour in point K: deviatoric stress vs. shear strain

The SC model has a remarkable impact on the deviatoric stress  $q$  vs. shear strain  $\gamma_{xy}$  curves, as the selected stress points of the models incorporating the SC model show a less pronounced decrease in shear stress compared to the equivalent model with MC. This subject is discussed in section 5.7 in detail.

The plot of the pre-consolidation stress  $\sigma'_{nc}$  at integration plane  $n_{cp}$  number 1 at a displacement of the anchor head of 7 cm is shown at the bottom of the list. This displacement and plane are picked, because they are the decisive ones. The notation of the vector  $n_i$ , which is perpendicular to the plane (see Fig. 3.7), starts in the direction of axis X and the shear stress is highest in this vertical plane along axis Y. This pre-consolidation stress indicates how far softening has progressed. The top 1.4 m of the fixed length are displayed and results smoothing is turned on. The plot of the model *Reference SC* shows that softening is further progressed than in the other models. It can also be seen in a  $q$ - $u$  graph in one stress point that the peak is reached earlier. The scale on the left indicates the value of the pre-consolidation stress. It is evident that the red parts show hardening, since it refers to a pressure of -2 000 kN/m<sup>2</sup>, which is lower than the initial value of the pre-overburden pressure of -1 800 kN/m<sup>2</sup>.

If no regularisation is used,  $L_{cal}$  has no influence on the calculation. In this case, softening spreads gradually from one stress point to the next one, perpendicularly to the shear band. At the same anchor load level of the compared model, softening has spread furthest without the regularisation (see Tab. 5.7). In stress point K, closest to the grout, the deviatoric stress decreases sharply when reaching the Hvorslev surface, as seen in Fig. 5.13. Therefore, among the compared models, this one exhibits the lowest load bearing capacity.

Tab. 5.7. Comparison of softening parameters – input parameters and results

Comparison softening parameters													
Name	Input parameters											No regularisation SC	
	h <sub>soft</sub>	L <sub>cal</sub>	h <sub>soft</sub> /L <sub>cal</sub>	h <sub>soft</sub> 70/L <sub>cal</sub> 0.04 (1750)	h <sub>soft</sub> 70/L <sub>cal</sub> 0.07 (1000)	h <sub>soft</sub> 72/L <sub>cal</sub> 0.02 (3600)	h <sub>soft</sub> 144/L <sub>cal</sub> 0.04 (3600)	h <sub>soft</sub> 144/L <sub>cal</sub> 0.02 (7200)	h <sub>soft</sub> 500	Reference MC	15-noded MC		Reference SC
Softening parameter	-	m	0.07	70	70	72	144	144	500	100	100	100	100
Internal length for non-local regularisation		m	0.07	0.04	0.04	0.02	0.04	0.02	0.04	0.04	0.04	0.04	0.04
Softening ratio		1/m	1 000	1 750	3 600	3 600	7 200	7 200	12 500	2 500	2 500	2 500	2 500
Stress points in non-local regularisation		m	39	17	5	16	5	5	17	17	17	77	77
Deviatoric stress - Point K	q <sub>max</sub>	kN/m <sup>2</sup>	190	190	190	190	190	190	190	190	190	190	190
	q <sub>res</sub>	kN/m <sup>2</sup>	166	138	111	94	71	71	72	112	119	136	115
Displacement at peak	Decrease		-13%	-28%	-42%	-51%	-63%	-63%	-62%	-41%	-39%	-28%	-39%
	u <sub>max</sub>	mm	0.104	0.101	0.099	0.097	0.094	0.094	0.088	0.102	0.096	0.104	0.098
Difference			2.2%	-0.4%	-2.8%	-5.1%	-7.3%	-7.3%	-13.7%	-	-6.1%	2.2%	-3.7%
	F <sub>max</sub>	kN	711	690	670	653	639	639	579	683	651	674	664
Ultimate bearing capacity			4.1%	1.1%	-1.9%	-4.4%	-6.5%	-6.5%	-15.3%	-	-4.7%	-1.2%	-2.7%
Difference													
Pre-consolidation stress (7cm)													
σ <sub>nc</sub>													

## 5.6 Dilatancy and peak friction angle – MLSM

In order to determine the impact of the MLSM, it is replaced by the HS model in the model *Reference MC* and compared to it. It is worth mentioning that the material set for the HS model features the critical state friction angle  $\varphi_{res}$ . As anticipated, the load-displacement curves show a significant difference of approximately 42 % in the ultimate bearing capacity (see Tab. 5.8). Even with a much higher softening rate, as in the model *hsoft 500 MC*, the difference is 31 %. It is caused by the peak shear strength located at the Hvorslev surface that is not captured in the HS model. The reason for the marginal increase in load after failure of the model without the MLSM is the soil at the top of the fixed length that still takes up load slowly (see Fig. 5.14). Another calculation with a soil stiffness reduced to one fifth is compared, which has no impact on the load bearing capacity but the displacement at peak is significantly higher.

Tab. 5.8. Comparison of the load bearing capacity and the respective displacement at top of the fixed length

Model	Displacement at peak [m]	Difference	Bearing capacity [kN]	Difference
<i>Reference MC</i>	0.016	-	686	-
<i>E soil low MC</i>	0.029	+80 %	684	+0 %
<i>MC/HS</i>	0.008	-50 %	400	-42 %
<i>hsoft 500 MC</i>	0.014	-16 %	579	-16 %
<i>E soil low hsoft 500 MC</i>	0.025	+85 %	587	+1 %

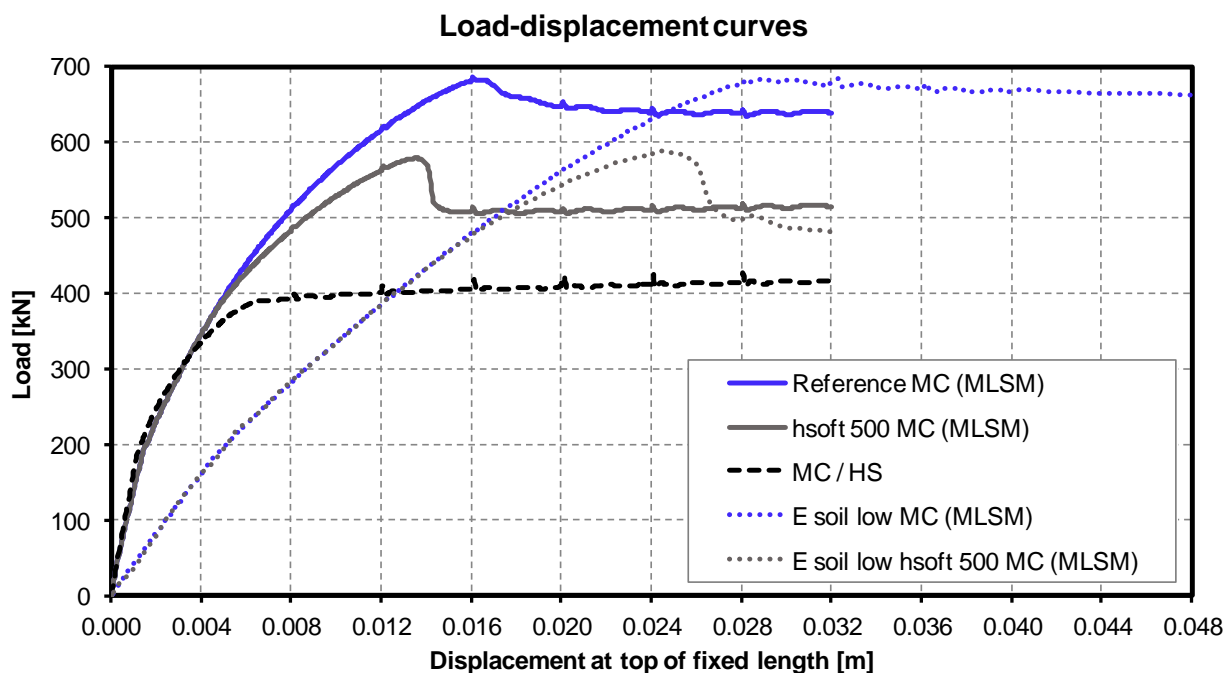


Fig. 5.14. Comparison of the load-displacement curves with the MLSM and the HS model featuring the critical state friction angle and models with a low soil stiffness

In order to reproduce the ultimate bearing capacity obtained with the HS model, a calculation according to the approach in section 2.2.1 and Equ. (2-1) is carried out. Basically, it solely takes the friction into account. However, the cohesion along the grout surface and the small vertical load acting on top of the fixed length is considered as well. Since the stress perpendicular to the fixed length is already known, the factor for conversion to normal stress on lateral surface  $a$  equals 1. The total

force acting normal to the anchor multiplied by  $\tan(\varphi_{res})$  as the coefficient of friction summed up with the cohesion and the vertical pressure results in the same load according to the simulation (see Tab. 5.9). As the strength of the grout is not exceeded in the present conditions, the attributed of the grout have no impact on the load bearing capacity. The strength of the soil is the prevailing factor in this case.

Tab. 5.9. Calculation according to static approach with the critical state friction angle

Calculation with the critical state friction angle			
1	Load perpendicular to fixed length	kN	955
2	Friction along fixed length	kN	348
3	Cohesion along fixed length	kN	34
4	Vertical load on top of fixed length	kN	7
5	Sum (2-4)	kN	389
6	Load according to simulation (MC/HS)	kN/m <sup>2</sup>	400

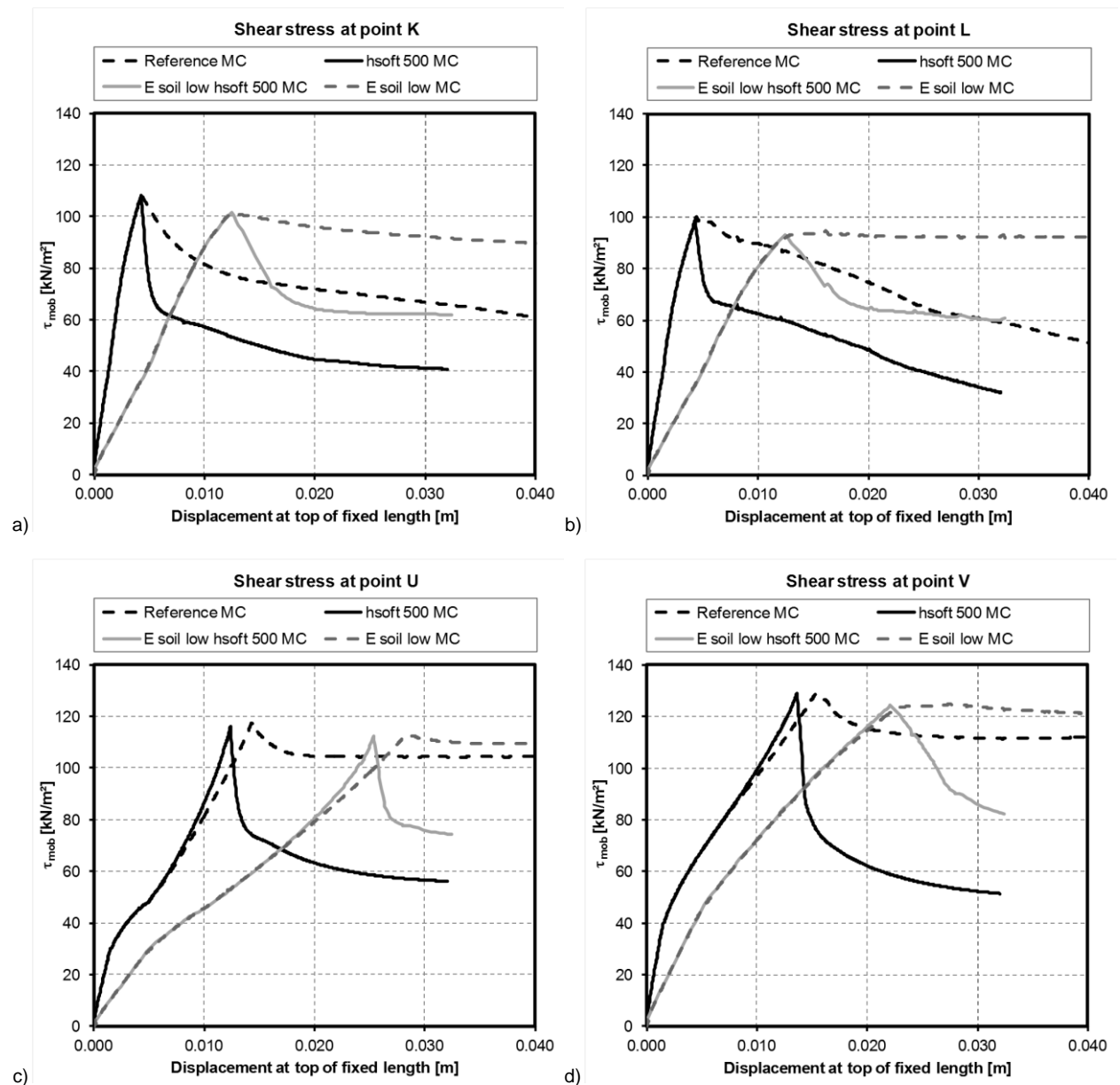


Fig. 5.15. Comparison of the shear stress at different points along the fixed length in the MLSM vs. displacement at top of fixed length for different softening ratios and soil stiffness: a) point K (top), b) point L (top), c) point U (centre), d) point V (bottom) of the fixed length

Fig. 5.15 shows the shear stress at different points along the fixed length (see Tab. 5.6) in the MLSM close to the grout surface against the displacement at top of the fixed length for the four compared models in this chapter, incorporating the MLSM. The impact of different softening ratios and soil stiffness on the progressive failure mechanism can be derived. The peak shear strength is lower in all stress points at lower soil stiffness. Furthermore, the peak is reached at a smaller displacement at the bottom than in the middle of the fixed length when the soil stiffness is low. The drop in shear stress is also smaller compared to the models with higher soil stiffness.

As already mentioned, the reason for the higher bearing capacity in residual state with the MLSM is caused by dilatancy. This behaviour is analysed by comparing the same three models as above: *Reference MC*, *hsoft 500 MC* and *MC/HS*.

Fig. 5.16a illustrates the strain development  $\varepsilon_{xx}$  perpendicular to the fixed length at a distance of 1 cm along the fixed length. The distribution of the respective pre-consolidation stress  $\sigma'_{nc}$  is compared in Fig. 5.16b, almost showing the same image, as they strongly interact. The pre-consolidation stress is an indicator of softening and along with this, the volume of the soil increases. Consequently, the radial stress acting on the anchor rises. This result of dilatant behaviour is shown in Fig. 5.17a with the comparison of the post-peak normal stress distributions along the fixed length. The models incorporating the MLSM exhibit significantly higher normal stress, which increases with a lower softening ratio. The normal stress develops simultaneously with the strain and pre-consolidation stress (pre-peak behaviour: cf. Fig. 5.5).

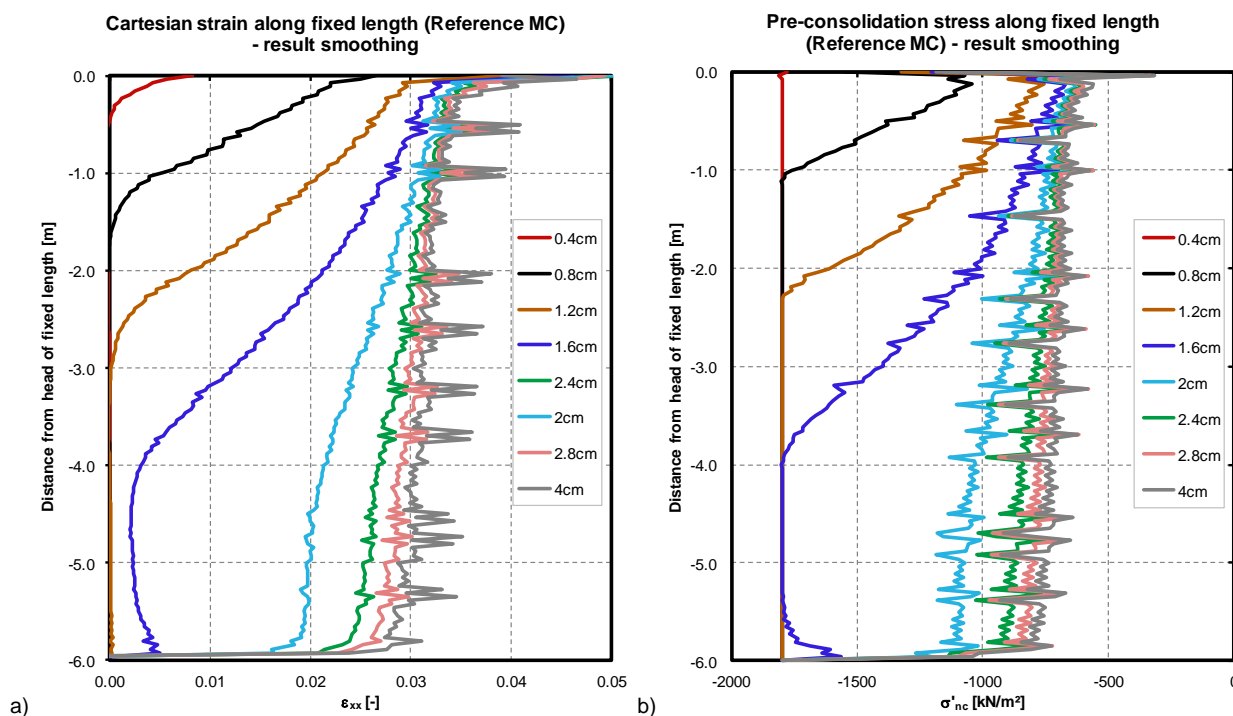


Fig. 5.16. *Reference MC*: a) Cartesian strain development  $\varepsilon_{xx}$ , b) pre-consolidation stress development along fixed length

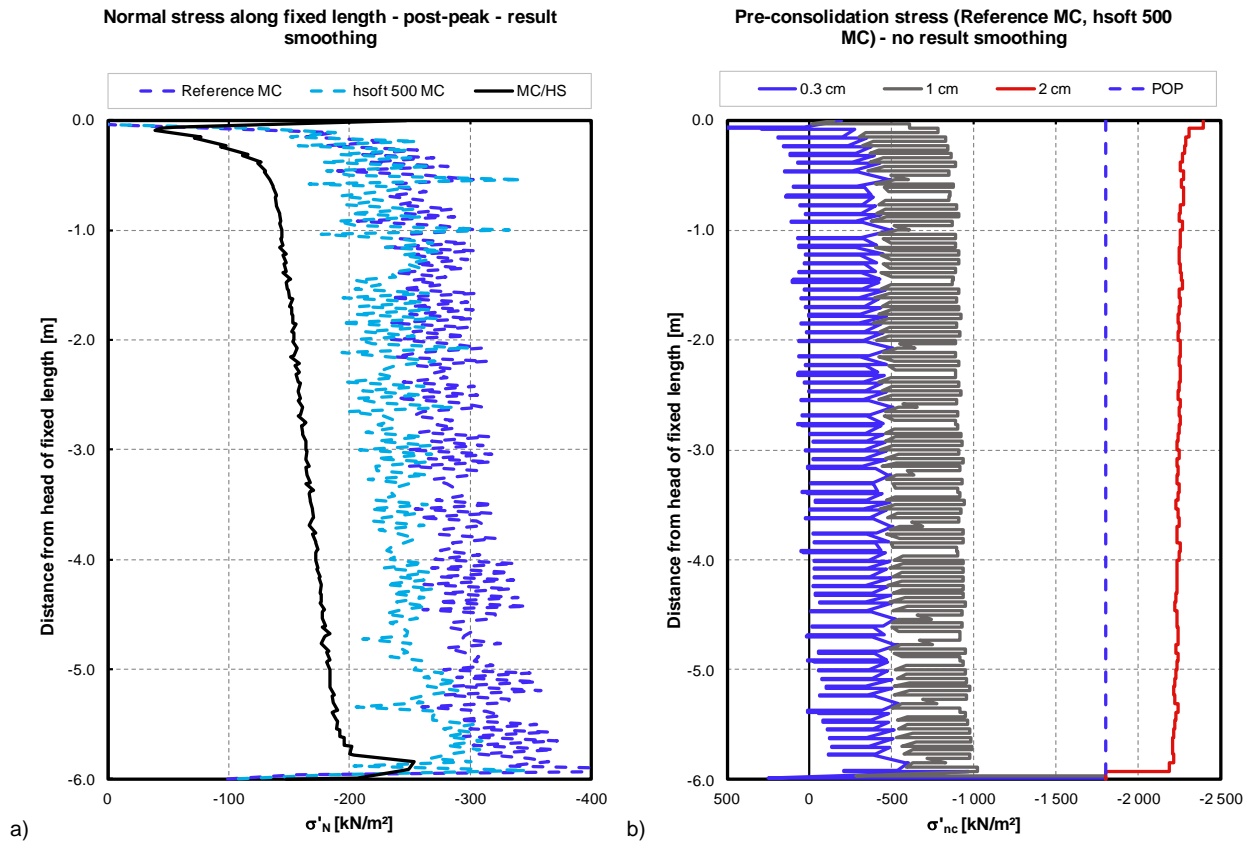


Fig. 5.17. Reference MC, hsoft 500 MC, MC/HS: a) Normal stress acting on fixed length (post-peak), b) Normal pre-consolidation stress at three cross-sections at indicated distance along fixed length and POP

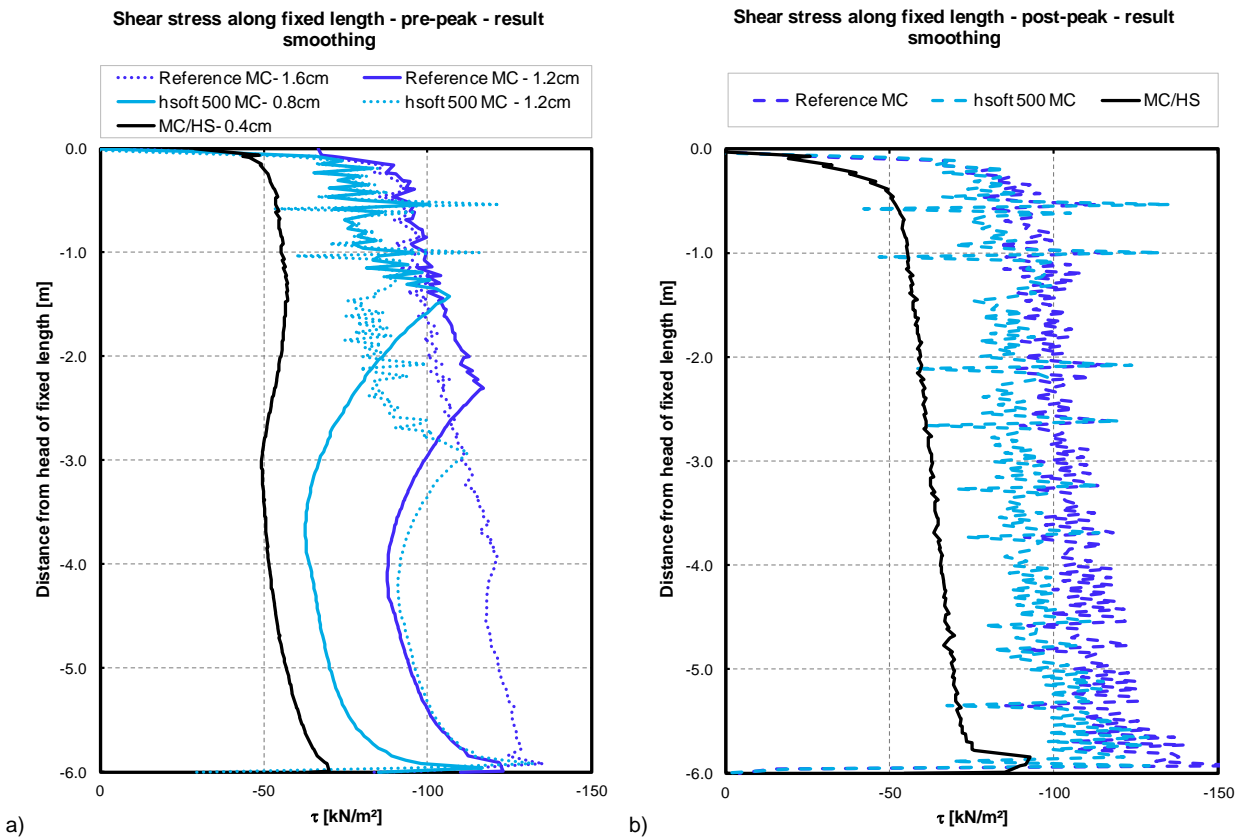


Fig. 5.18. Reference MC, hsoft 500 MC, MC/HS: Shear stress along fixed length: a) pre-peak, b) post-peak

The pre-consolidation stress distribution in the residual state at a displacement of 4 cm at the top of the fixed length in Fig. 5.16b has still not reached the normally consolidated state when this stress is

zero. However, the soil close to the grout body has already reached the critical state friction angle  $\varphi_{res}$  of  $20^\circ$ , as shown in Fig. 5.7. The reason for this deviation is the present pressure in the soil, the used result smoothing and the location of the cross-section at a distance of 1 cm to the grout body, where the soil has not completely softened so far.

As a means of comparison, the pre-consolidation stress at three cross-sections along the fixed length is displayed in Fig. 5.17b without result smoothing. The notation of the curves indicates the distance to the grout body. It can be seen, that some captured stress points exhibit a pre-consolidation stress of zero. These curves are similar for the models *Reference MC* and *hsoft 500 MC*. In addition, the pre-consolidation stress right at the edge of the pre-defined shear band at a distance of 2 cm to the grout ( $X = 0.170$ ) is displayed. It shows clearly that hardening has occurred in this part as the initial POP is lower than the current pre-consolidation stress, which is also a consequence of dilatancy.

The state at failure still shows an increase in shear and normal stress towards the end of the fixed length (see Fig. 5.17 and Fig. 5.18). The reason is the increase in shear strength with higher stress at the bottom and smaller strain, hence less softening and dilatancy.

Fig. 5.18 shows the shear stress distribution along the fixed length of the three compared models, divided in pre- and post-peak. The model with the lower softening ratio (*Reference MC*) exhibits a slightly higher mobilised shear stress. However, the calculated mobilised peak friction angle  $\varphi'_{mob}$  according to Equ. (5-1) in the compared models are equal although the stresses are not (see Fig. 5.19 and Fig. 5.7). This is possible because the normal and shear stress are both higher in the model *Reference MC*.

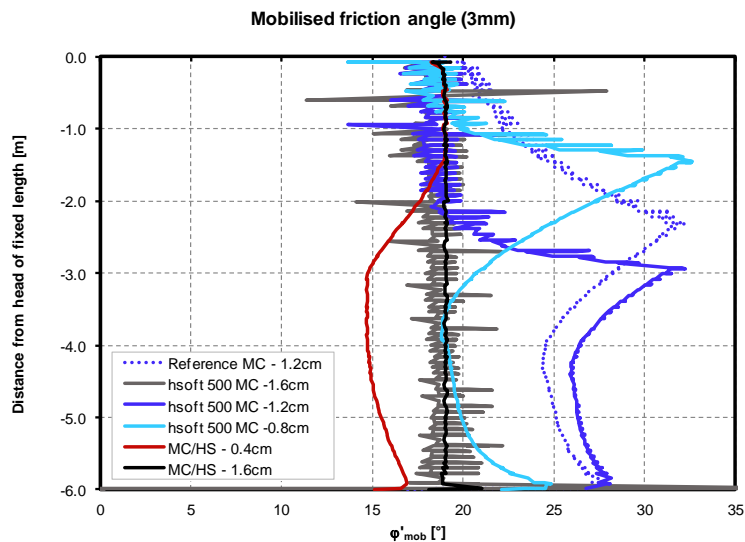


Fig. 5.19. *Reference MC*, *hsoft 500 MC*, *MC/HS*: Mobilised friction angle along fixed length

Fig. 5.20a illustrates the Cartesian and volumetric strain in the soil next to the top of the fixed length (point K) in the model *Reference MC* against the displacement at top of the fixed length. As already mentioned, the volumetric strain is almost entirely in direction X, perpendicular to the grout body. It is compared to the Cartesian strain of the models with low soil stiffness and higher softening ratio in

Fig. 5.20b, since the behaviour differs significantly. As anticipated, the models with lower soil stiffness exhibit higher volumetric strain. On the contrary, it is decreased with a higher softening ratio.

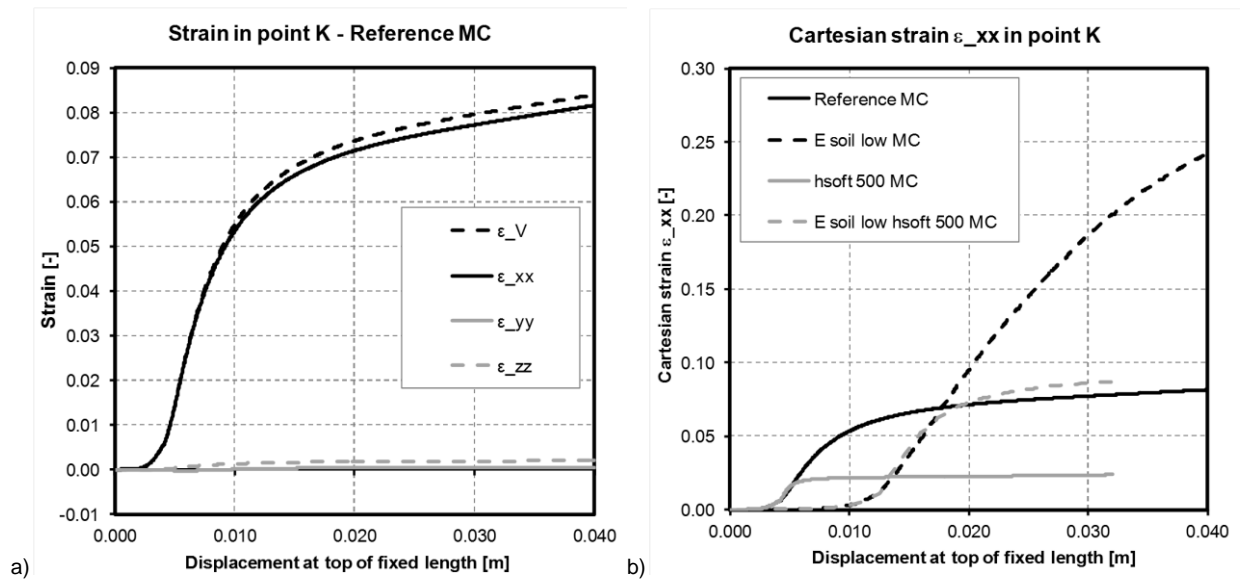


Fig. 5.20. Strain in point K vs. displacement at top of fixed length for different softening ratios and soil stiffness: a) *Reference MC*: Cartesian and volumetric strain, b) *Reference MC*, *E soil low MC*, *hsoft 500 MC*, *E soil low hsoft 500 MC*: Cartesian strain  $\varepsilon_{xx}$

As already mentioned, the ultimate load bearing capacity is not affected by the decrease in soil stiffness to one fifth. The shear stress along the fixed length appears to be almost the same (see Fig. 5.21a). However, the shear stress is more uniformly distributed in soft soil and the peak has progressed further in the stiff soil when reaching the ultimate load bearing capacity. As anticipated, the normal stress resulting from dilatant behaviour differs. Shortly before the peak of the load-displacement curve at a displacement of 1.2 cm in the model *hsoft 500 MC*, the normal stress has already reached its final value. On the contrary, the normal stress increase in the soft soil at the same stage has only spread along the upper 2 m of the fixed length (see Fig. 5.21b).

The mobilised peak friction angle is almost the same in the soft and stiff soil. However, the residual angle is reached in the stress points along the fixed length in the soft soil at the same time (see Fig. 5.22).

In conclusion, it is neither the ratio of the stiffness between soil and grout nor one of them separately that has an impact on the load bearing capacity. Yet, the progressive failure mechanism is affected, whereas the stiffness increases along with the POP, which in turn influences the load bearing capacity.

This dilatant behaviour is intrinsically determined by the MLSM without any additional user input. Efforts were made to reproduce this behaviour with the HS model. Two simulations based on the model *MC/HS* are prepared, one with a dilatancy angle  $\psi$  of  $1^\circ$  and another one with  $3^\circ$  and an additional setting for the maximum void ratio  $e$  of 0.6. This adjustment acts as a dilatancy cut-off (*DCO*). The value for the *DCO* is determined with the maximum strain caused by dilatancy in the MLSM, which is converted to the increase in void ratio, taken into account the default setting for the initial void ratio of 0.5.

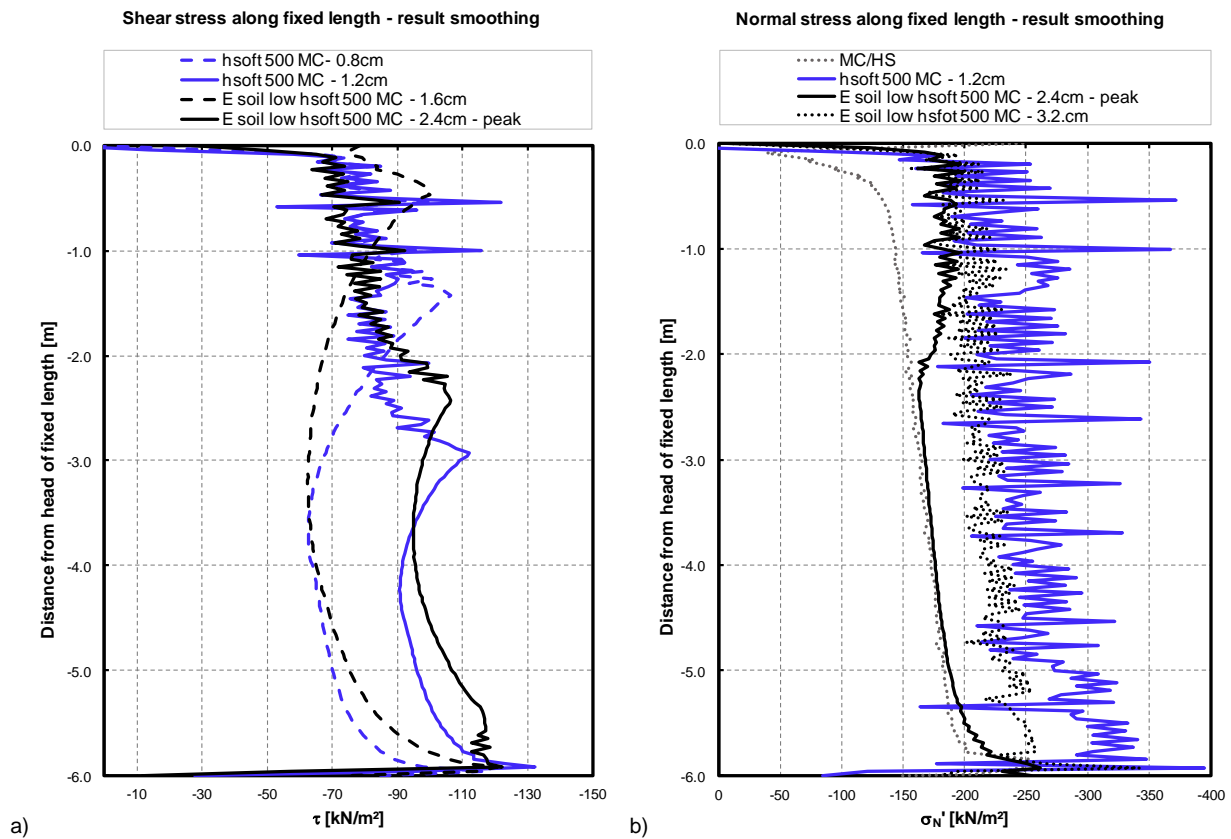


Fig. 5.21. Stress along fixed length of *hsoft 500 MC*, *E soil low hsoft 500 MC*: a) shear stress, b) normal stress

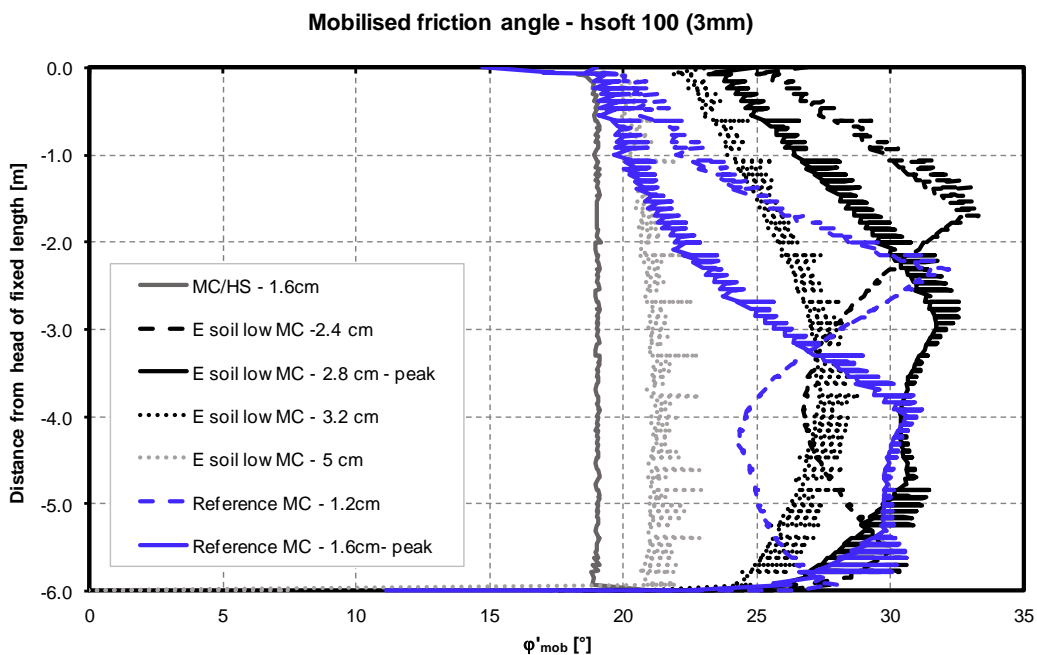


Fig. 5.22. *E soil low MC*: mobilised friction angle along fixed length

The resulting load-displacement curves are compared to the models *Reference MC* and *MC/HS* in Fig. 5.23. Without DCO activated, dilatancy causes a steady increase in load, whereas DCO reduces this behaviour. Still, the load increases slightly, although it is flattened.

Fig. 5.24 a and b show the shear and normal stress development along the fixed length. Starting from the point where the curve is flattened, the stress distribution oscillates. DCO does not work properly, as higher void ratios than the set value occur.

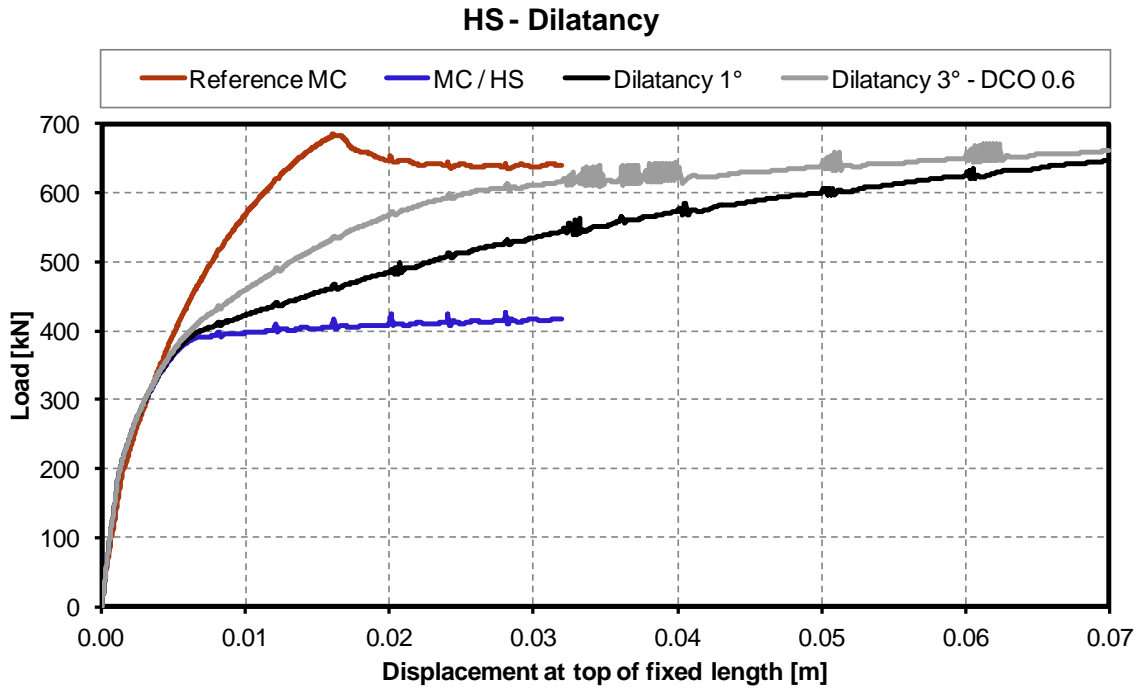


Fig. 5.23. Load-displacement curves with HS model and dilatancy / DCO

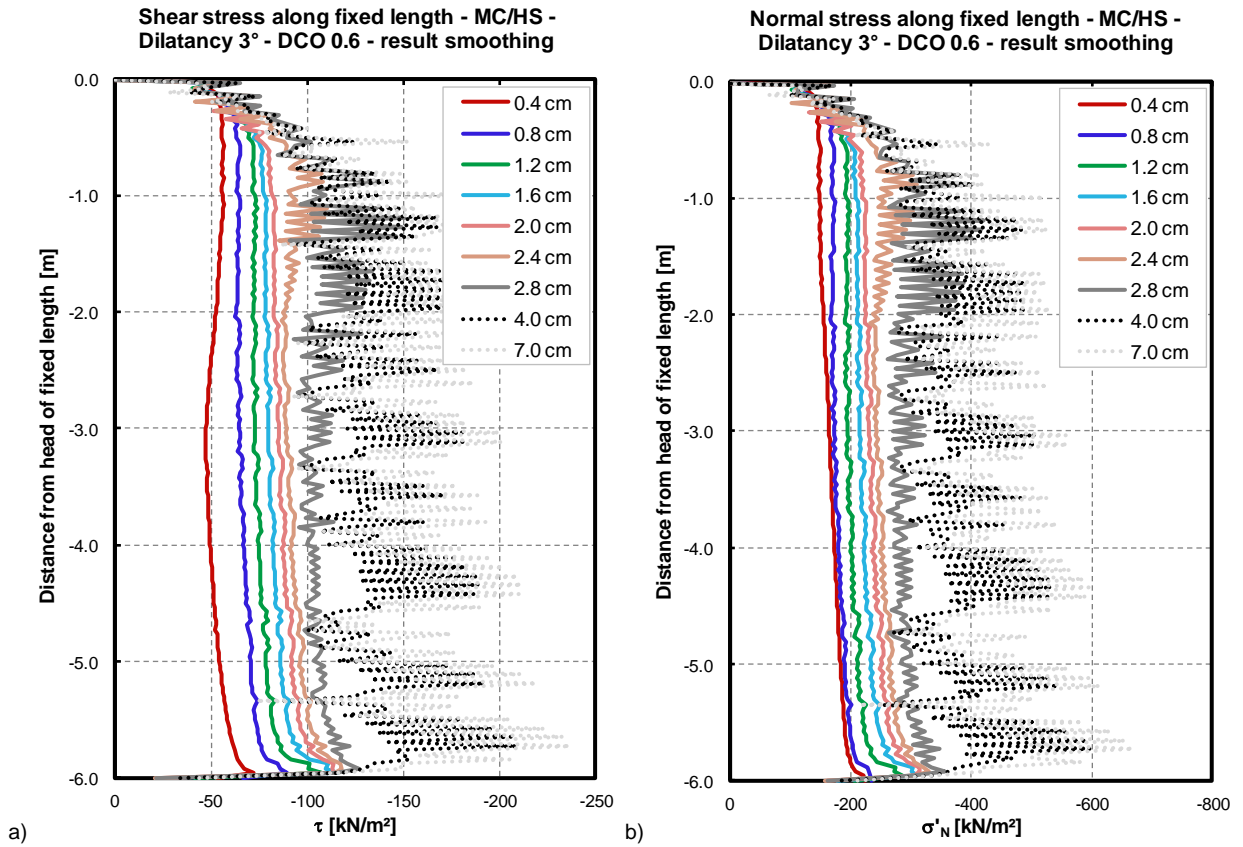


Fig. 5.24. Dilatancy 3° - DCO 0.6 MC: a) shear stress development, b) normal stress development along fixed length

## 5.7 Tension softening – SC model

The shotcrete model has only a minor impact on the load bearing capacity of the anchor in this basic model without grout in the free length, as Fig. 5.25 implies. It shows the load-displacement curves of the model with both Shotcrete and Mohr-Coulomb model as grout material. Since the former features strain softening, it implicates a reduction in stiffness in this type of loading. However, even this effect is insignificant in this anchor load. Based on this analysis, one is tempted to neglect strain softening and hardening of the grout. Nonetheless, it is taken into account, since further and more complex investigations are carried out with a higher influence of that particular bearing behaviour.

In this section, the two models *Reference MC* and *Reference SC* are compared in terms of tension softening. Furthermore, two simulations were executed with the SC model, one with an increased fracture energy  $G_f$  and one with the Young's modulus  $E$  of the grout body cut by one third (values see Tab. 5.10). Additional analyses on the behaviour and influence of the SC model on the system are carried out with the advanced model in chapter 6, incorporating grout in the free length. Those analyses are focused on compression hardening and softening.

If using the SC model should be avoided but the same behaviour is wanted, the stiffness of the Mohr-Coulomb parameters could be fitted to the cracked state modelled with the SC model with the load-displacement curve of the SC model.

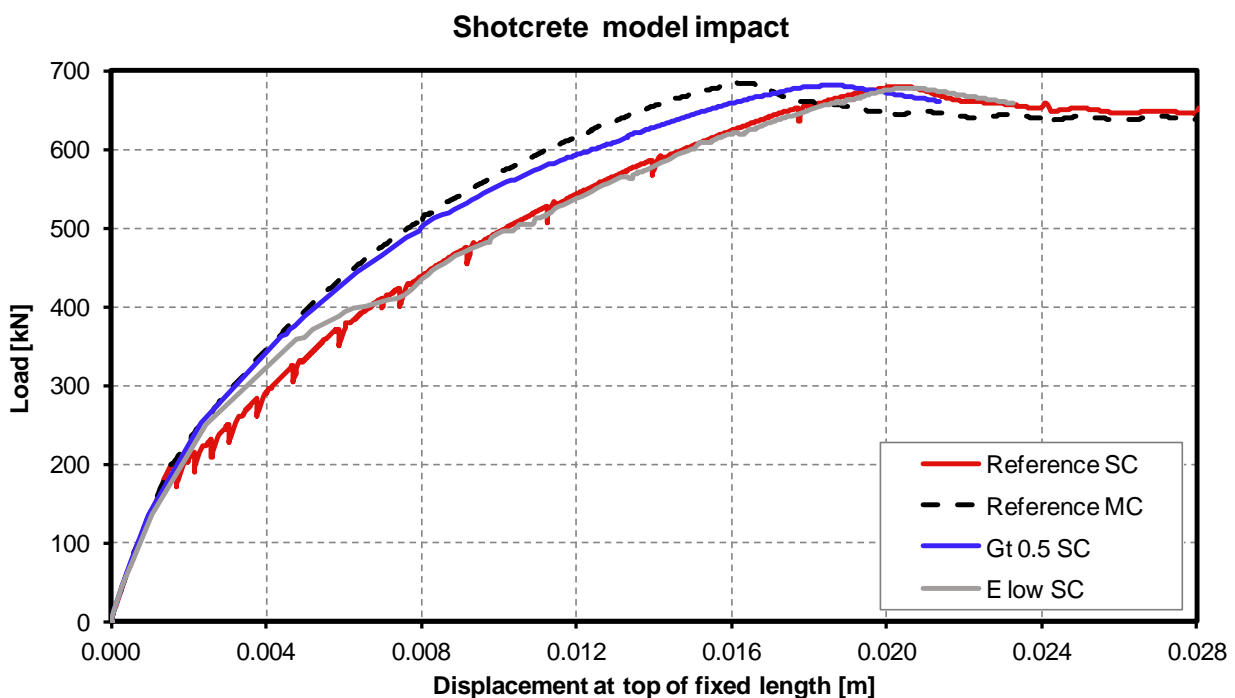


Fig. 5.25. Load- displacement curves: difference between SC (*Reference SC*) and MC material model (*Reference MC*) for grout body

Tab. 5.10. Changed parameters for comparison

Model	Changed parameter	Unit	Initial value	Changed value
<i>Gt 0.5 SC</i>	Fracture energy $G_f$	kN/m	0.15	0.50
<i>E low SC</i>	SC Stiffness $E_{28}$	kN/m <sup>2</sup>	30 000 000	20 000 000

Fig. 5.25 shows the load-displacement curves of the four compared models. Their peak load and respective displacements are listed in Tab. 5.11. None of the alterations of the SC model has an impact on the load bearing capacity, solely on the stiffness of the system.

Tab. 5.11. Comparison of the load bearing capacity and the respective displacement for the determination of the SC model impact

Model	Displacement [m]	Difference	Bearing capacity [kN]	Difference
<i>Reference SC</i>	0.020	-	680	-
<i>Reference MC</i>	0.016	-21.1 %	686	+0.9 %
<i>Gt 0.5 SC</i>	0.019	-8.4 %	681	+0.1 %
<i>E low SC</i>	0.021	+0.4 %	678	-0.3 %

The reason for the lower stiffness when using the SC model with the same stiffness input values as the MC model is the simulation of cracking of the grout. However, the grout is still a continuum. Therefore, cracks are hereinafter defined by the softening parameter  $H_t$  being higher than 1, which indicates that the major principal plastic strain exceeds the plastic ultimate strain in tension. Thus, the material is in residual state in this point. Fig. 5.26b shows a plot of the tension softening parameter in the grout at peak load. The scale ranges till 1, which means that the areas beyond this value are softened and in residual state. Tension softening has already progressed extensively in this state. Fig. 5.26b represents the same plot for the model *Gt 0.5 SC*. As anticipated, this model exhibits a more ductile behaviour. Thus, only a small proportion of the grout body is in residual state. In addition, the effective principal stresses are plotted for the model *Reference SC* (see Fig. 5.26c). The light regions in Fig. 5.26b, as indications for the residual state, and those in Fig. 5.26c with hardly any effective principal stresses concur with each other, because the tension is restricted to the residual strength level  $f_{tu,n}$  in these areas. On the contrary, the MC model solely features a tension cut-off (TCO), which prevents an increase in tensile forces, but does not decrease the strength (cf. Fig. 5.4).

Fig. 5.27 shows the impact of the SC model on the adjacent soil by comparing the shear stress of the models *Reference SC* and *Reference MC* at a load level of 356 kN. The occurrence of the oscillations in the not yet softened parts can be traced back to cracking in the grout, simulated by the SC model. Although this shear stress distribution does not display the same load level as in Fig. 5.26, the oscillations can be assigned to the softened parts in the grout. Moreover, the peak has progressed further in the model incorporating the SC model, because of high strains caused by the cracks.

Since the cement mortar used for the grout itself is not reinforced, as opposed to fiber concrete, the fracture energy  $G_{i,28}$  is significantly low. This can lead to numerical calculations that do not converge, although the model itself cannot fail physically. The load-displacement curve of the model *Reference SC* features several small, stepwise declines, called unloading steps hereinafter (see Fig. 5.25). Thus, arc-length control, which is implemented in PLAXIS, must not be activated as it would not deliver any reliable results in this case for the load bearing capacity of an anchor. The reason is the setting “Max. unloading steps” for downgrading, after which the calculation is cancelled and the error message “Soil body seems to collapse” occurs. The reason for this behaviour is strain softening in the SC model, as the unloading steps correlate with the appearance of cracks. It arises locally and

involves stress redistribution in the surrounding areas. Those unloading steps are displayed vertically in the load-displacement curve, because no further displacement occurs and only the anchor force is reduced.

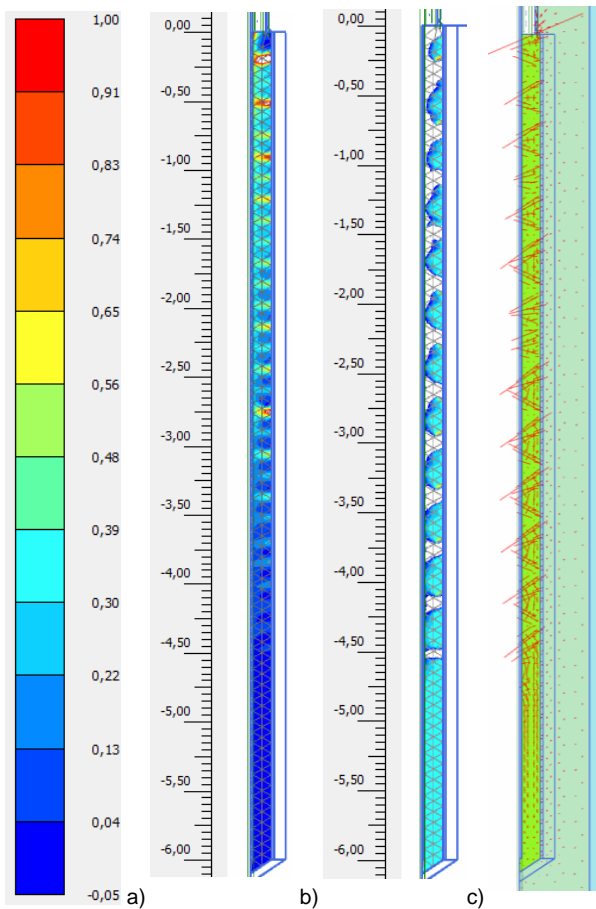


Fig. 5.26. Comparison tension softening (scaled from 0 to 1) of different values for the fracture energy  $G_f$  at peak load: a)  $G_t 0.5$  SC ( $G_f=0.5$ ), b) *Reference* SC ( $G_f=0.15$ ) and c) effective principal stresses (*Reference* SC;  $G_f=0.15$ )

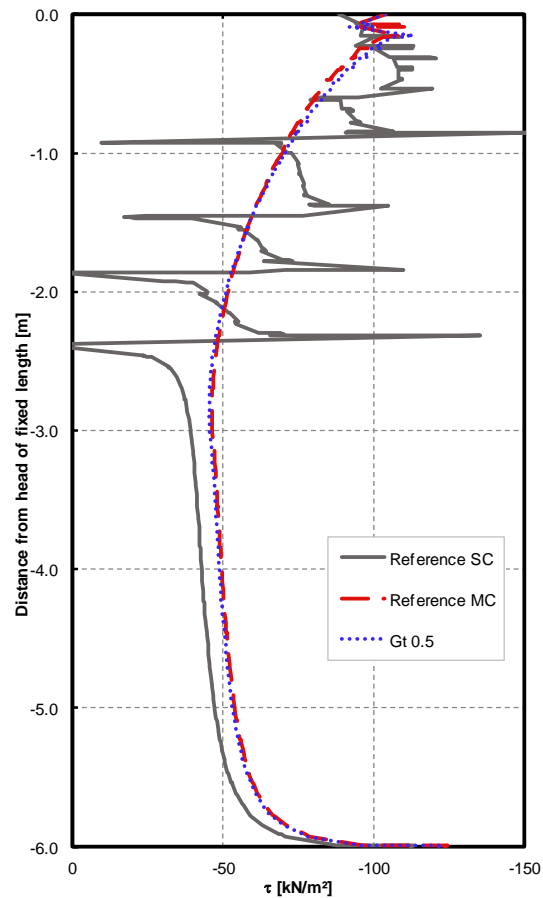


Fig. 5.27. Influence of the SC model on the shear stress in soil and variation of fracture energy in tension  $G_t$  (dashed: low; dotted: high) at a load level of 390 kN

During this unloading process, structural snap-back occurs, as the load is redistributed (Schädlich and Schweiger 2014 b). In order to reach equilibrium, not only the force has to be reduced, but also the displacement. However, this is not possible in the load advancement procedure in PLAXIS. Hence, the global error increases. Fig. 5.28 depicts the relationship between global error and calculation progression for the load-displacement curve in Fig. 5.25. The curve for the global error is referenced to the primary ordinate against the load steps on the abscissa and overlaid with the load to the secondary ordinate. The increase in global error coincides with the decline in load. The number of those unloading steps is consistent with the amount of cracks (see Fig. 5.26). It takes a number of steps after the global error increases significantly along with the crack initiation until the convergence is reached again and load increase carries on.

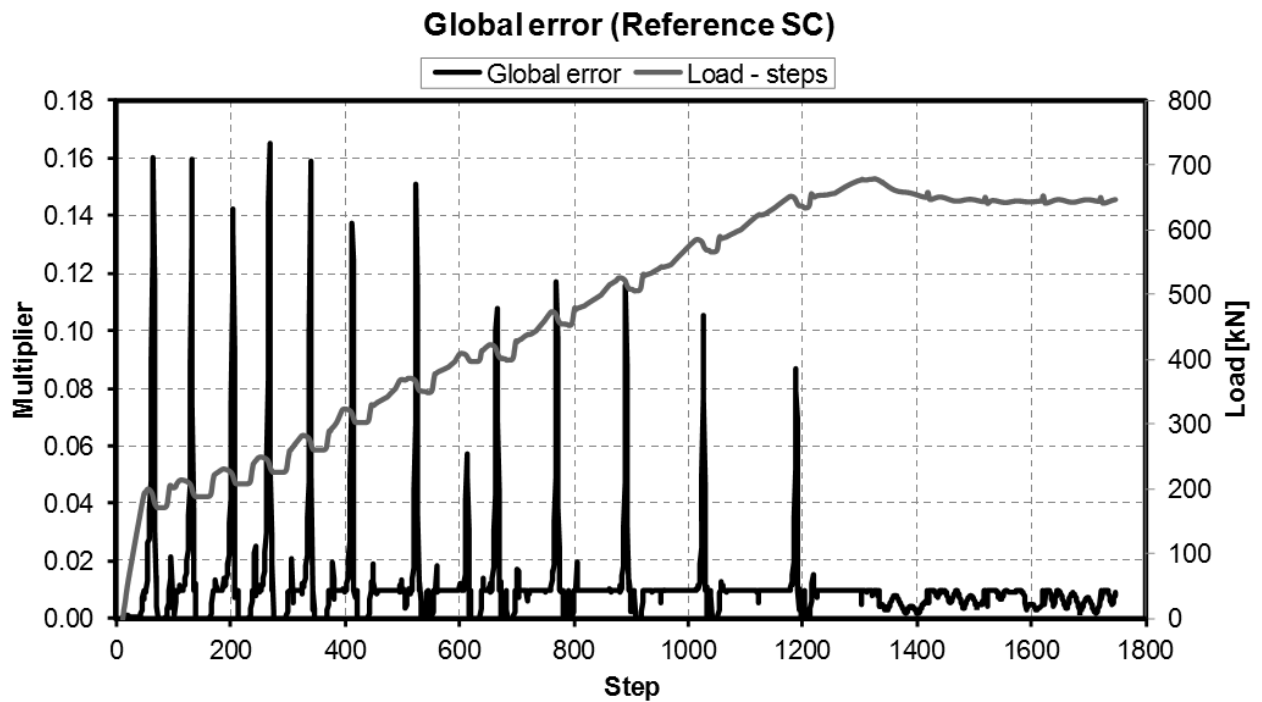


Fig. 5.28. *Reference SC*: Global error and anchor load vs. load steps

Another open issue of the SC model is crack alignment with mesh orientation (Schädlich and Schweiger 2014 b). A finer mesh would produce more evenly distributed cracks as the model exhibits a preferred crack alignment along element boundaries. Since a precise reproduction of the crack propagation is not the aim of the analyses in this chapter and it has no influence on the load bearing capacity, this issue can be neglected in these models.

The models *Reference SC* and *E low SC* exhibit almost the same load-displacement curve, the latter only behaves stiffer in the very beginning (see Fig. 5.25). The reason is that cracking starts later when the stiffness of the grout is lower. This can be investigated in Fig. 5.29, showing the shear stress in the soil along the grout body of the compared models at two different load levels. As opposed to the model *Reference SC*, the model featuring a lower stiffness of the grout does not show any signs of cracking at an anchor load of 388 kN. Yet, the shear stress of the two models is almost the same at a load of 511 kN. On the whole, cutting the stiffness by one third results in almost the same behaviour in this case.

The comparison of the softening behaviour in the MLSM in point K of different calculations in terms of deviatoric stress vs. shear strain in Fig. 5.13 shows the impact of the SC model on the progressive failure. The model *Reference SC* exhibits a smaller drop in deviatoric stress compared to the model incorporating the MC model instead of the SC model. The reason is the lower stiffness ratio of soil and grout, which is demonstrated by the models *E soil low MC* and *E soil low hsoft 500 MC* for a high change in this ratio in Fig. 5.15.

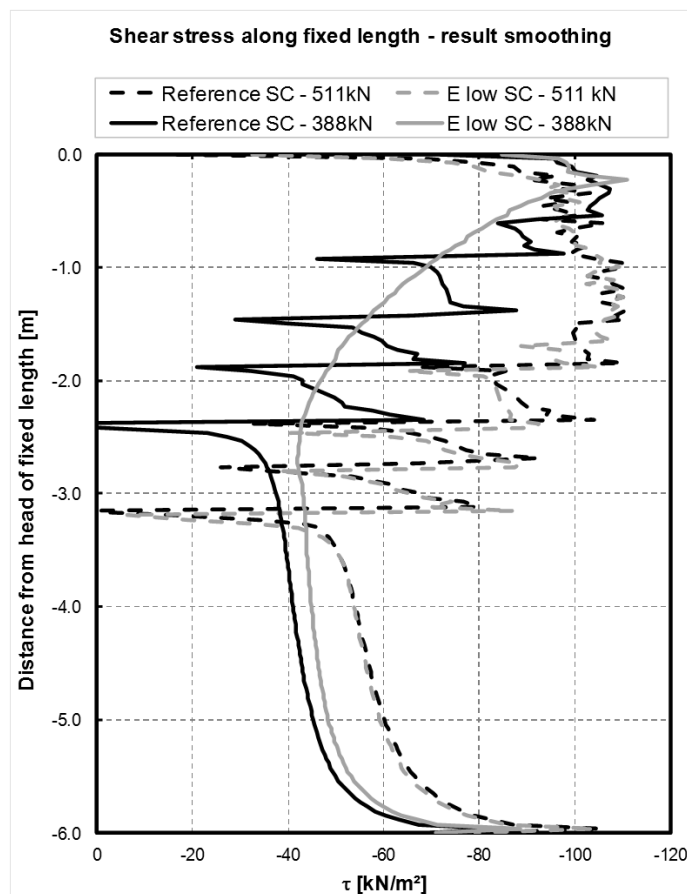


Fig. 5.29. Influence of Young's modulus on the shear stress in soil at two different load levels

## 5.8 Geometry impact

Additional analyses were carried out in order to determine the influence of two basic model geometries. The *Reference MC* model is taken for comparison, because the grout in both of them is modelled with the MC model and the free length is not filled. First of all, the radius of the area of the application of the MLSM is changed from a radius of 0.5 m in the reference model to 1.2 m. As anticipated, this change has no influence on the system, because the softening does not spread to the outer boundary of the MLSM and the stress points located there are not taken into account in non-local regularisation.

Furthermore, the overall radius of the model was decreased from 5 m to 2.5 m. This has also no significant influence on the results of the calculation. This outcome is of special interest in the consideration of the advanced models in order to reduce calculation time. The changes of the models and the results are summarized in Tab. 5.12 and compared to the reference model.

Tab. 5.12. Changes and results of the geometry modifications

Model	Dimensions reference	Modified dimensions	Change in load bearing capacity	Change in disp. at failure
	m	m	-	-
<i>MLSM radius MC</i>	0.5	1.2	+0.0 %	+0.3 %
<i>Radius model MC</i>	5	2.5	-0.1 %	+1.8 %

## 6 Advanced model computations

This section deals with the advanced model calculations, indicated by “FreeL” in the models’ designation, as they focus on simulating grout in the free length, its effects and the sensitivity to assumptions. The geometries are modelled as sketched in Fig. 4.4 and described in section 4.1. The properties of the grout in the free length are set equal to the fixed length, as the same material is placed in both areas in reality. Since the input is based on assumptions and simplifications, modifications in terms of geometries and properties are made in order to determine the modelling influence.

The model *FreeL SC* is the reference for the alterations concerning the free length (see Fig. 4.4). The behaviour of this model is analysed in this section. Moreover, it is compared to the model *FreeL MC* with the MC model as constitutive model for the grout.

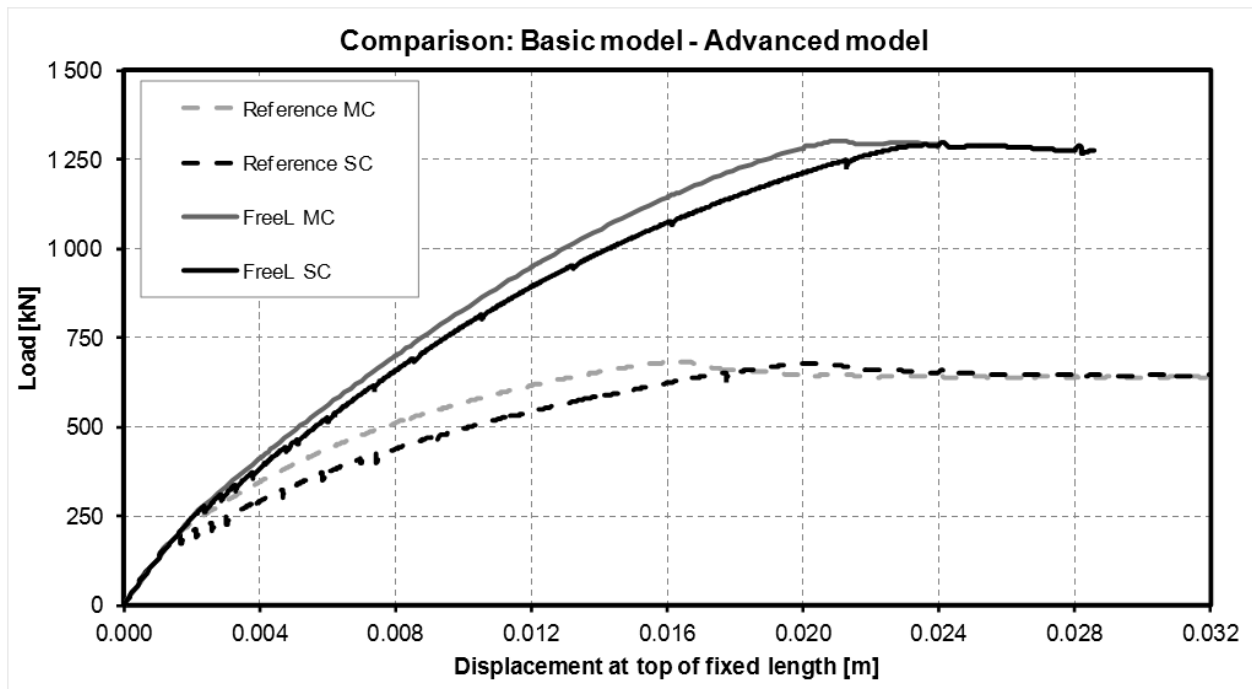


Fig. 6.1. Load-displacement curves for comparison of basic and advanced model

The load-displacement curves in Fig. 6.1 show the significant impact of the grout in the free length. The ultimate bearing capacity is increased by 90 % with both SC and MC model, as listed in Tab. 6.1. This value does not possess general validity but only applies to the present geometries and material properties. The grout set in the free length increases the stiffness of the whole system. The comparison between the application of the SC and MC model for the grout delivers the same prediction as in the basic model, since the SC model primarily influences the stiffness and maintains the load bearing capacity. The reason is that the capacity of the grout is intentionally not exceeded in both models, because the aim of the present thesis is to investigate the bearing capacity of the interface between soil and grout. As already mentioned in chapter 2, this is the location where failure generally occurs. However, the behaviour of the free length has to be observed and analysed in terms of material properties and geometries, as it is subject to many assumptions. Thus, this chapter focuses on the bearing capacity of the free length.

Tab. 6.1. Grout in free length: comparison of the load bearing capacity and the respective displacement at top of the fixed length

Model	Displacement at peak [m]	Difference	Bearing capacity [kN]	Difference
<i>Reference MC</i>	0.016	-	686	-
<i>FreeL MC</i>	0.021	+31 %	1304	+90 %
<i>Reference SC</i>	0.020	-	680	-
<i>FreeL SC</i>	0.024	+15 %	1 291	+90 %

The yield strength of the tendon is exceeded in these calculations. However, this has no impact on the calculations, since it is modelled linear-elastically.

## 6.1 Overview of performed analyses

The main aim of this chapter is to evaluate the influence of the grout in the free length and its sensitivity to changes in material parameters and geometries. Tab. 6.2 gives a comprehensive account of the performed analyses conducted in this chapter. Moreover, the respective values of the reference model and the new values assigned to the changed parameters are listed. The analyses are separated in seven categories. The classification is made according to the following specifications:

- **Reference:**  
Contains the models with different combinations of material models taken for comparison.
- **Mesh:**  
Evaluation of the generated mesh.
- **HS:**  
Comparison of the initial and residual state of the normal stress acting on the anchor, being changed by dilatancy.
- **Geometry:**  
Analysis of the influences of the chosen support conditions and the geometry of the grout in the free length.
- **Material:**  
Demonstration of the impact of SC model material parameters.
- **Bearing capacity grout:**  
Exceedance of the bearing capacity of the grout prior to the interface shear strength between grout and soil.
- **Grouting:**  
Evaluation of assumptions for the simulation of pressure grouting.

Tab. 6.2. Advanced model: overview of performed analyses and changed parameters

Category	Model name	Grout	Soil	Description/ Parameter changed	Value Reference		New value	
Reference	<i>FreeL SC</i>	SC	MLSM	-	-		-	
	<i>FreeL MC</i>	MC	MLSM	-	-		-	
	<i>FreeL SC/HS</i>	SC	HS	-	-		-	
	<i>FreeL MC/HS</i>	MC	HS	-	-		-	
Mesh	<i>FreeL- coarse SC</i>	SC	MLSM	Average element size [m]	0.078		0.179	
	<i>FreeL- coarse MC</i>	MC	MLSM	Average element size [m]	0.078		0.179	
	<i>FreeL- coarse SC/HS</i>	SC	HS	Average element size [m]	0.099		0.179	
HS	<i>FreeL- no dilatancy SC/HS</i>	SC	HS	Soil unit weight $\gamma$ [kN/m <sup>3</sup> ]	15.24		9.20	
Geometry	<i>FreeL- no support SC/HS</i>	SC	HS	No support in free length	-		-	
	<i>FreeL- width- no support SC/HS</i>	SC	HS	No support in free length Width free length [cm]	-		6.0 9.6	
Material	<i>FreeL- Gc SC/HS</i>	SC	HS	Compressive fracture energy $G_c$ [kJ/m]	50.00		8.00	
	<i>FreeL- strength low SC/HS</i>	SC	HS	Reduced strength $f_c, f_t$ [kN/m <sup>2</sup> ]	25 000	2 000	10 000	800
	<i>FreeL- strength Free SC/HS</i>	SC	HS	Reduced strength $f_c, f_t$ [kN/m <sup>2</sup> ]	25 000	2 000	10 000	800
	<i>FreeL- ecp low SC/HS</i>	SC	HS	Uniaxial plastic failure strain $\varepsilon_{cp}^p$ [-]	-0.0010		-0.0005	
	<i>FreeL- a 0 SC/HS</i>	SC	HS	Increase of $\varepsilon_{cp}$ with increase of $p' a$ [-]	16		0	
Bearing capacity grout	<i>FreeL- gamma x2 MC/HS</i>	MC	HS	Soil unit weight $\gamma$ [kN/m <sup>3</sup> ]	15.24		30.48	
	<i>FreeL- gamma x2 SC/HS</i>	SC	HS	Soil unit weight $\gamma$ [kN/m <sup>3</sup> ]	15.24		30.48	
	<i>FreeL- gamma x2 Gc SC/HS</i>	SC	HS	Soil unit weight $\gamma$ [kN/m <sup>3</sup> ]	15.24		30.48	
		SC	HS	Compressive fracture energy $G_c$ [kJ/m]	50.00		8.00	
	<i>FreeL- worst case SC/HS</i>	SC	HS	No support in free length	-		-	
		SC	HS	Reduced strength $f_c, f_t$ [kN/m <sup>2</sup> ]	25 000	2 000	10 000	800
		SC	HS	Uniaxial plastic failure strain $\varepsilon_{cp}^p$ [-]	-0.001000		-0.000267	
SC		HS	Increase of $\varepsilon_{cp}$ with increase of $p' a$ [-]	16		0		
Grouting	<i>Grouting MC</i>	MC	MLSM	$K_0$ [-]	1		1.5	
	<i>FreeL- grouting MC</i>	MC	MLSM					
	<i>FreeL- grouting MC/HS</i>	MC	HS					
	<i>FreeL- no grouting MC</i>	MC	MLSM	No enlargement fixed length	-		-	

## 6.2 Modifications

This section deals with modification made in comparison to the basic model. First of all, the compressive fracture energy  $G_c$  of the SC model is adjusted. As already mentioned, it is increased from 8 kN/m to 50 kN/m. This parameter does not have any impact on the load-displacement curve of the basic model. However, it has a major influence on the behaviour of the anchor when considering the grout in the free length. Higher fracture energy increases the ductility of the system, which prevents sudden failure of the free length. The impact of this parameter on anchor loading is analysed in sections 6.7 and 6.8.

Another modification was made concerning the calculations conducted with the HS model used for the surrounding soil. As already shown in Fig. 5.14 and described in section 5.6, neither the ultimate nor the residual load bearing capacity of the models using the MLSM or the HS model coincide. The reason for the higher residual value in the MLSM calculations is the dilatancy. The normal stress acting on the grout body in varying states of anchor loading is shown in Fig. 6.2 for the model *FreeL SC*. As the majority of the analyses in this section focus on the SC model and its impact on anchor loading, the MLSM is replaced by the HS model in the surrounding soil of the anchor. However, the

HS model does not feature intrinsic specification of dilatant behaviour without any additional input, which is why the residual normal stress is predefined in order to reach the same residual load bearing capacity. This creates similar stress states in the grout, which is the aim of this modification.

Tab. 6.3. Approximated residual normal stress state for calculations with HS model

Approximated perpendicular residual stress state - Free length		
Stress at ground surface	kN/m <sup>2</sup>	0.00
Stress at the distal end of the anchor	kN/m <sup>2</sup>	320.00
Total anchor length	m	21.00
Soil unit weight	kN/m <sup>3</sup>	18.50
Input soil unit weight - MLSM	kN/m <sup>3</sup>	9.20
<b>Input soil unit weight - HS</b>	<b>kN/m<sup>3</sup></b>	<b>15.24</b>

The change in normal stress on the anchor is implemented by increasing the soil unit weight. Its extent is adapted to the normal stress in the reference model. The initial and approximated residual stress state is indicated by the dashed lines in Fig. 6.2. Tab. 6.3 lists the conditions leading to the soil unit weight used for the approximated stress in the HS model. It is obvious that the stress in the area of the free length is intentionally underestimated compared to the model *FreeL SC*. The intention is to decrease the impact of the free length for the same reasons indicated in section 4.1 with regard to the void in the free length. Furthermore, the soil closer to the ground surface has experienced higher unloading of the POP, which is why the increase in normal stress due to dilatancy in the uppermost soil layer is too high. Section 6.4 goes into detail of that matter.

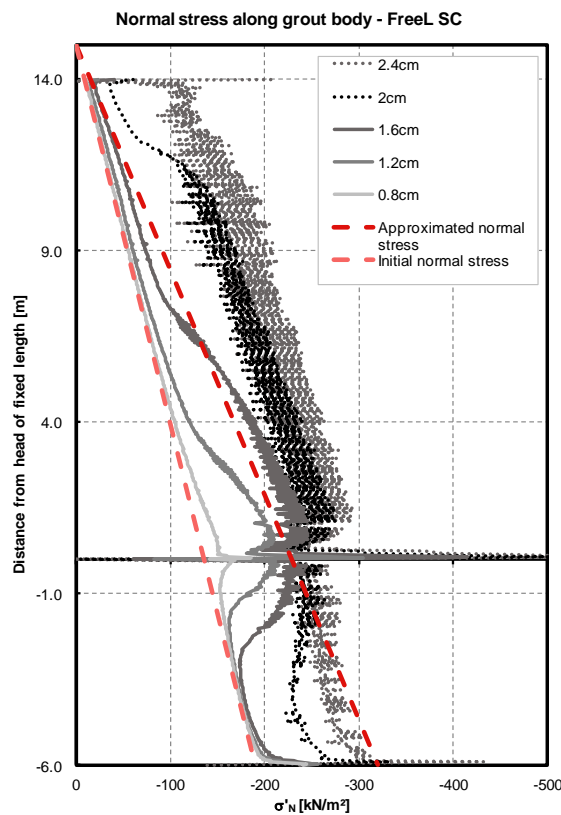


Fig. 6.2. *FreeL SC*: normal stress along grout body and approximated normal stress for the residual state with HS

Tab. 6.4. Modifications for HS model: comparison of the load bearing capacity and the respective displacement at top of the fixed length

Model	Displacement at peak [m]	Difference	Bearing capacity [kN]	Difference
<i>FreeL SC/HS</i>	0.018	-	1 075	-
<i>FreeL SC</i>	0.024	+33 %	1 291	+20 %
<i>FreeL- no dilatancy SC/HS</i>	0.011	-39 %	670	-38 %

Fig. 6.3 shows the results of the increase in normal stress by changing the soil unit weight in the HS model compared to the former conditions and Tab. 6.4 lists the values at failure.

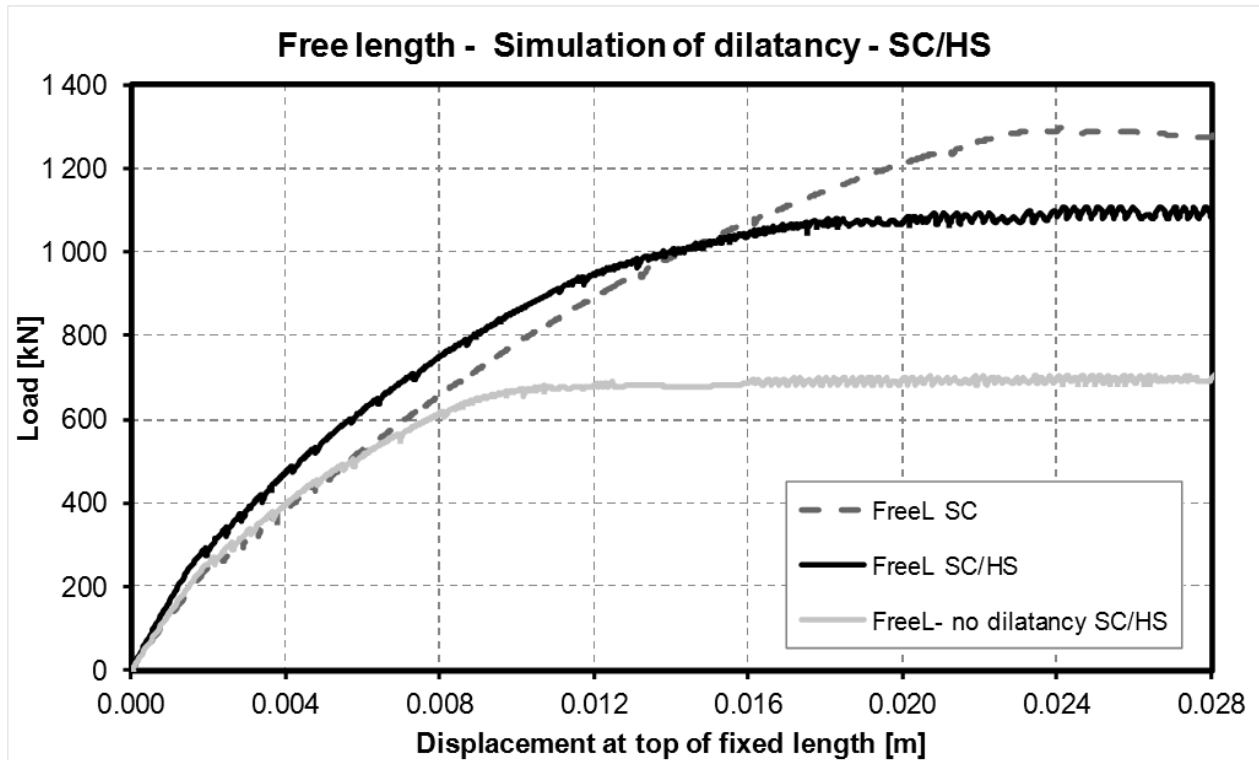


Fig. 6.3. Comparison of load-displacement curves of initial and residual state of the normal stress acting on the anchor

Fig. 6.4 shows the impact of the used constitutive models on the load distribution between fixed and free length. The load component in the free length is plotted vs. displacement at top of the fixed length. This figure is generated by integrating the normal stress at the junction between free and fixed length (cross section as defined in Tab. 6.8) and comparing it to the entire force at the respective displacement.

Approximately 50 % of the load is transferred to the soil via free length in the models *FreeL SC* and *FreeL MC*, which is the highest proportion of the compared models. The reason for the difference between MC model and SC model used for the grout is the non-cracked state of the fixed length in the MC model. As strain softening is not featured in the MC model, it behaves stiffer and as a result, dilatancy along the fixed length is mobilised earlier in the load advancement procedure. This difference is not visible in the models incorporating the HS model instead of MLSM, since the normal stress due to dilatancy is initially set. The geometries of the grout body and the even gradient of the normal stress  $\sigma'_{xx}$  determine the load distribution in those models. The load proportion in the free length for the current case is 46 %, which is calculated according to section 2.2.1 in Tab. 6.5 and the results of the simulation shown in Fig. 6.4. It does not depend on the input value of the soil unit

weight, because the ratio of stress acting on the anchor stays the same. However, this is only applicable if the interface between soil and grout is decisive, which is the case in these computations. This is verified by adding up the friction and cohesion along the grout body in Tab. 6.5, which equals the ultimate load bearing capacity of the model *FreeL SC/HS*. Furthermore, the maximum uniaxial load of the free length is calculated, which is much higher than the actual peak load in the free length. In conclusion, the bearing capacity of the grout is not exceeded.

Tab. 6.5. Calculative load distribution in HS model

Load proportion in free length (HS model)			
Input soil unit weight HS		kN/m <sup>3</sup>	15.24
Free length	Circumference	m	0.69
	Length	m	14.00
	Load perpendicular to free length	kN/m	1 707
		kN	1 180
	Friction along free length	kN	429
	Cohesion	kN	58
	Total peak load	kN	487
	Area free length $A_{free}$	m <sup>2</sup>	0.03
Max. uniaxial load (=UCS * $A_{free}$ )	kN	754	
Fixed length	Circumference	m	0.94
	Length	m	6.00
	Load perpendicular to fixed length	kN/m	1 554
		kN	1 465
	Friction along free length	kN	533
	Cohesion	kN	34
	Total peak load	kN	567
Total load		kN	1 054
Load proportion free length		%	0.46

Other modifications are conducted concerning the overall geometries. The radius of the model is reduced from 5 m to 3 m and the MLSM was applied within an area of 0.35 m to the axis of symmetry instead of 0.5 m (cf. Fig. 4.3, Fig. 4.4). Section 5.8 delivers evidence that these modifications impact neither the stiffness nor the load bearing capacity. Furthermore, the shear band is reduced from 2 cm to 1.5 cm and implemented twice in parallel in order to refine the mesh in those areas, which can be seen in Fig. 6.6.

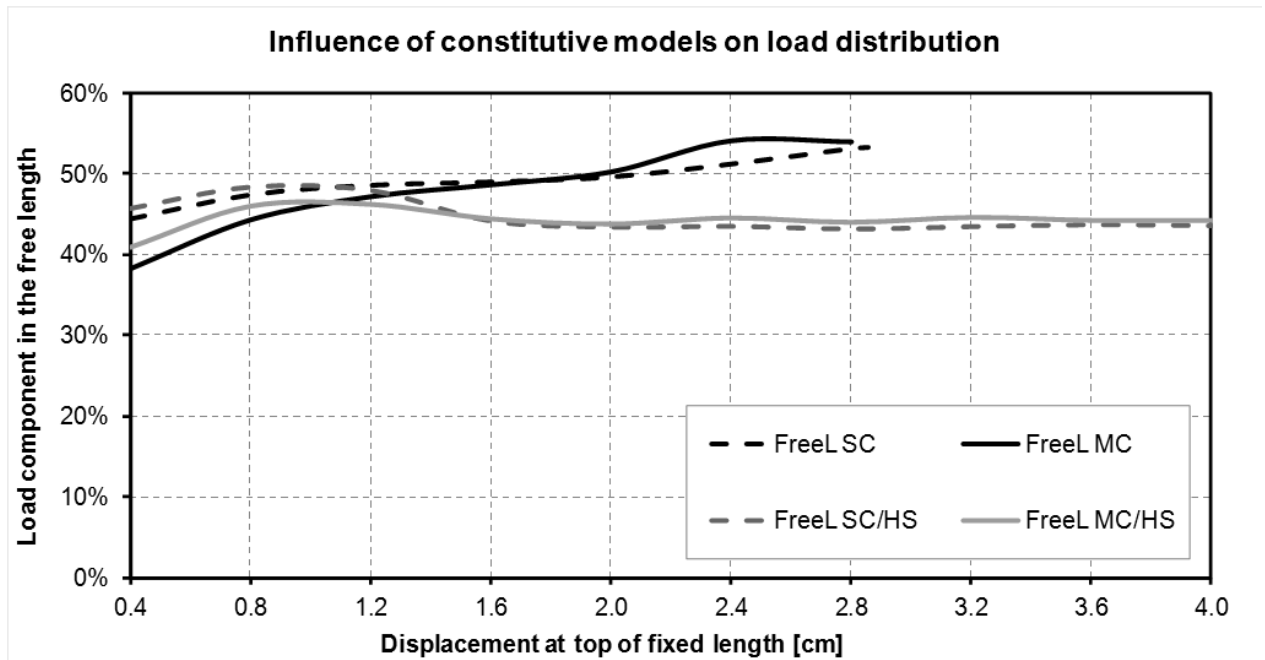


Fig. 6.4. Influence of used constitutive model on load distribution

### 6.3 Free length – mesh sensitivity analysis

The finest mesh possible for the given geometries is chosen for the advanced model analyses conducted in this chapter. Thus, these results are compared to coarser meshes in order to show its impact. Three different analyses are performed with three reference models (*FreeL SC*, *FreeL MC* and *FreeL SC/HS*), but with the same fine and coarse mesh. Tab. 6.6 lists the number of elements and the average element size of the used, fine mesh and the compared, coarse one.

Tab. 6.6. Free length: mesh sensitivity analysis

Mesh sensitivity analysis		
	Number of elements [-]	Average element size [m]
Used mesh	12 321	0.078
Coarse mesh	3 917	0.179

Fig. 6.5 shows the different mesh fineness used for the compared models. The detail of the junction between free and fixed length is picked out in Fig. 6.6.

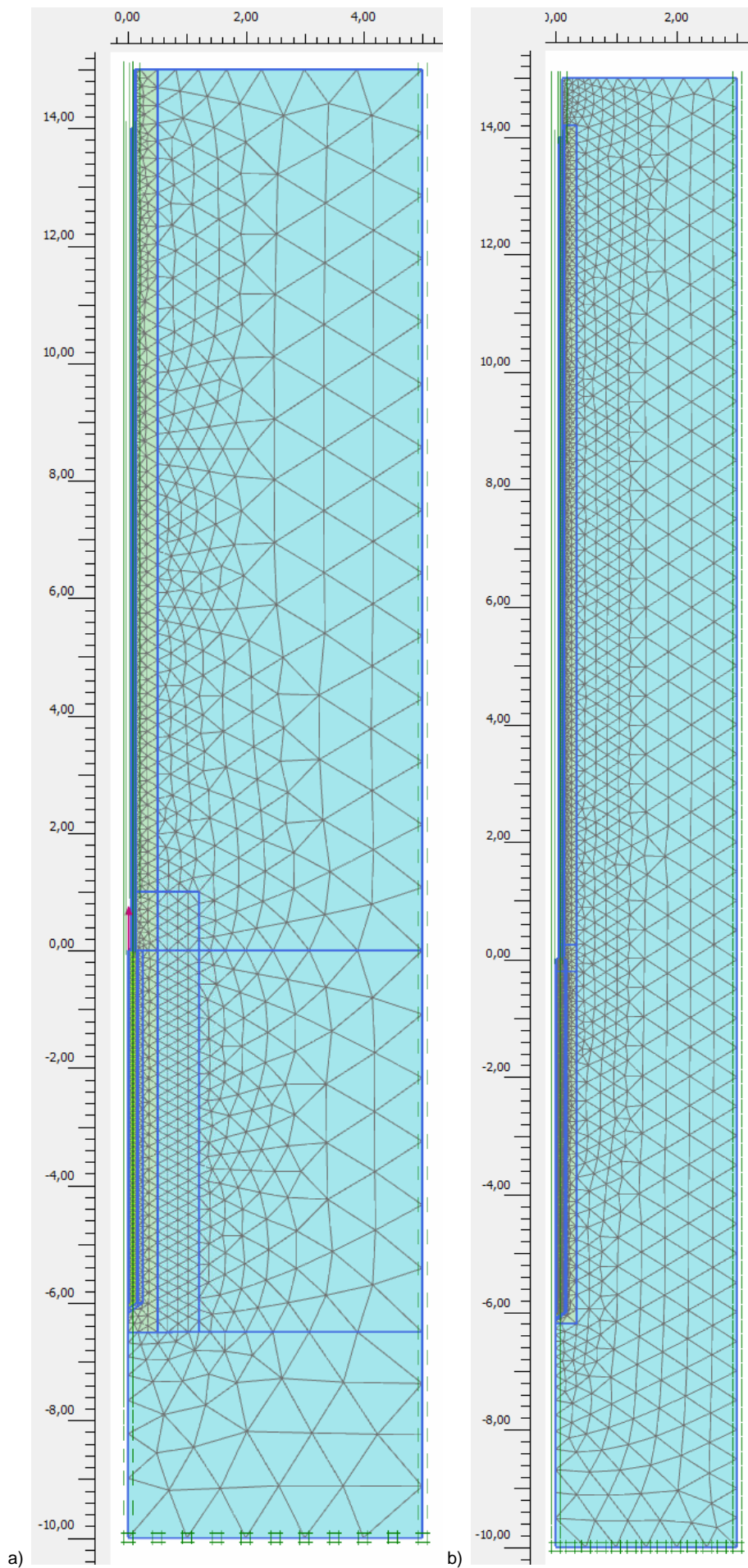


Fig. 6.5. Comparison of different mesh fineness: a) coarse, b) fine

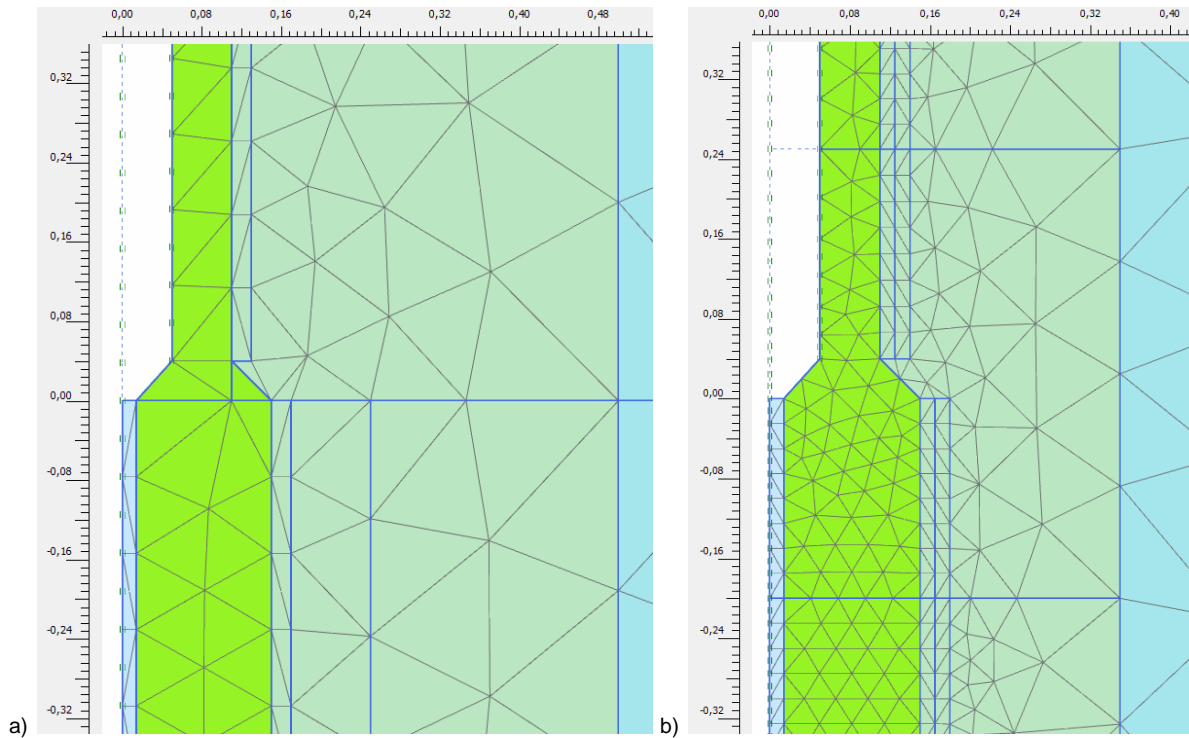


Fig. 6.6. Comparison of different mesh fineness: a) *FreeL - coarse SC*, b) *FreeL SC*

The load-displacement curves of the compared models are shown in Fig. 6.7 and compared in Tab. 6.7.

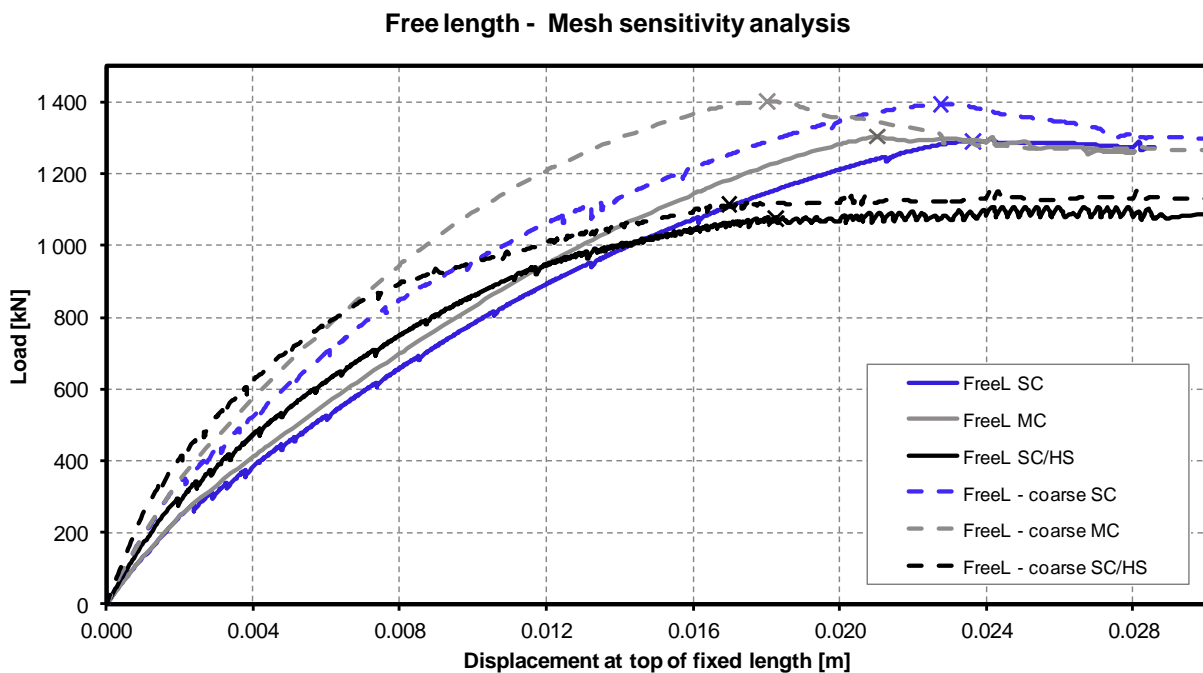


Fig. 6.7. Mesh sensitivity advanced model: load-displacement curves

The combination of MC and MLSM is most affected by the change of mesh fineness regarding stiffness of the system. Both sensitivity analyses with the MLSM are in the same range of about 8 % and the SC model combined with the HS model 3 % in terms of load bearing capacity. Thus, the MLSM exhibits the highest mesh dependency in this case. Nevertheless, the stresses occurring in the grout body especially in the junction between free and fixed length are much different. The main

deviations occurring in the coarse mesh are shown in the following and compared to the figures resulting from the fine mesh in the subsequent two sections.

Tab. 6.7. Advanced model: mesh sensitivity analysis

SC/MLSM mesh sensitivity				
Model	Displacement [m]	Difference	Bearing capacity [kN]	Difference
<i>FreeL SC</i>	0.024	-	1 291	-
<i>FreeL - coarse SC</i>	0.023	-3 %	1 394	+8.0 %
MC/MLSM mesh sensitivity				
Model	Displacement [m]	Difference	Bearing capacity [kN]	Difference
<i>FreeL MC</i>	0.021	-	1304	-
<i>FreeL - coarse MC</i>	0.018	-15 %	1 401	+7.4 %
SC/HS mesh sensitivity				
Model	Displacement [m]	Difference	Bearing capacity [kN]	Difference
<i>FreeL SC/HS</i>	0.018	-	1 075	-
<i>FreeL - coarse SC/HS</i>	0.017	-6 %	1 108	+3.1 %

Fig. 6.8 plots the stresses in different stress points in the soil along the grout body against the displacement at top of the fixed length. The stresses in the soil at top of the free length (point K, L) differ significantly from those in the basic model (cf. Fig. 5.10a) and the fine mesh (cf. Fig. 6.18), whereas the other points further down are not affected (point U, V). The reason is a failure mechanism at the junction between free and fixed length, which does not occur to the same extent in the fine mesh. The consequences are represented hereafter.

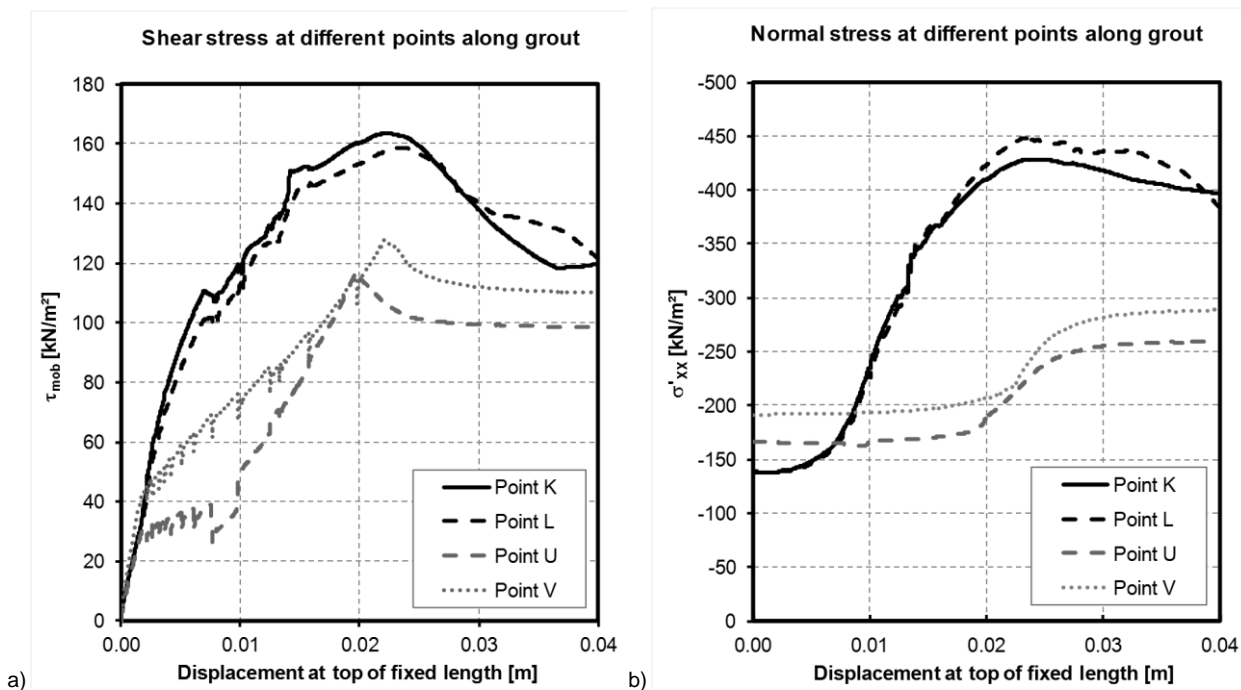


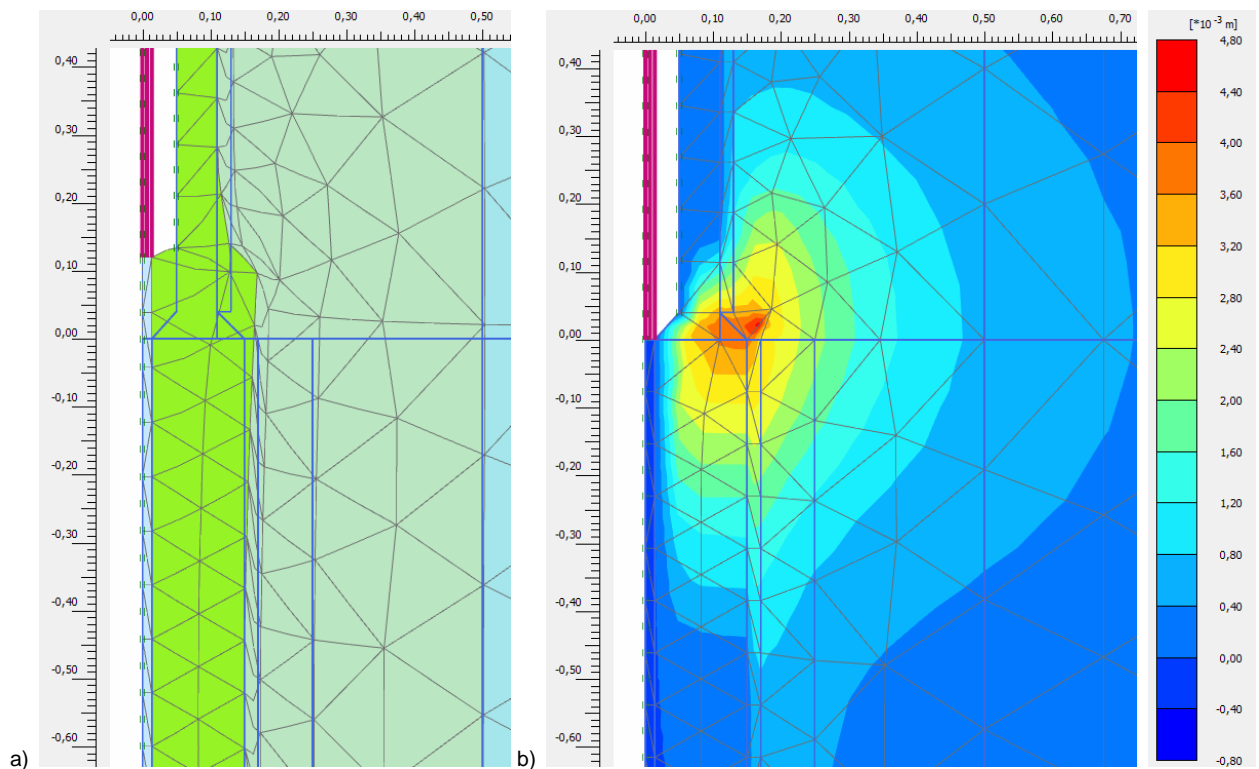
Fig. 6.8. *FreeL - coarse SC*: Stress at different points along the grout body (K, L: top; U: centre; V: bottom) vs. displacement at top of fixed length: a) shear stress and load-displacement curve, b) normal stress

Fig. 6.9 shows similar figures for the model *FreeL - coarse SC* as in Fig. 6.19 for the model *FreeL SC* in order to represent the impact of the mesh fineness. The focus is set on the junction between free and fixed length in terms of deformed mesh, total displacements in horizontal direction, normal pre-consolidation stress, effective principal stresses in the soil and compression softening parameter  $H_c$  at a post-peak displacement of 2.4 cm. At this state, a displacement of approximately 4.5 mm in

perpendicular direction to the prescribed displacement has developed, which is twice as much as in the model *FreeL SC*. In particular, the grout body deforms in this direction together with the soil when using the coarse mesh, whereas the fine mesh prevents this behaviour.

The scale of the figure of the normal pre-consolidation stress shows only hardening in plane 1 (see Fig. 6.9c). This area stretches along the topmost 60 cm of the fixed length. The major effective principal compressive stresses in the adjacent soil have aligned horizontally at the elevation of the junction. Moreover, the soil on top of the fixed length is pressurised by the enlargement of the grout body in the fixed length. This failure mechanism arising at the junction between free and fixed length is a result of compression softening and crack alignment along element boundaries, because it does not occur when the MC model is used and it is diminished by increasing the compression fracture energy  $G_c$ . This context is discussed in sections 6.5 and 6.6.

The described radial stress increase in the area of the junction between fixed and free length is clearly demonstrated when plotting the normal stress along the grout body as in Fig. 6.10 and comparing it to the respective figure of the fine mesh (cf. Fig. 6.20b).



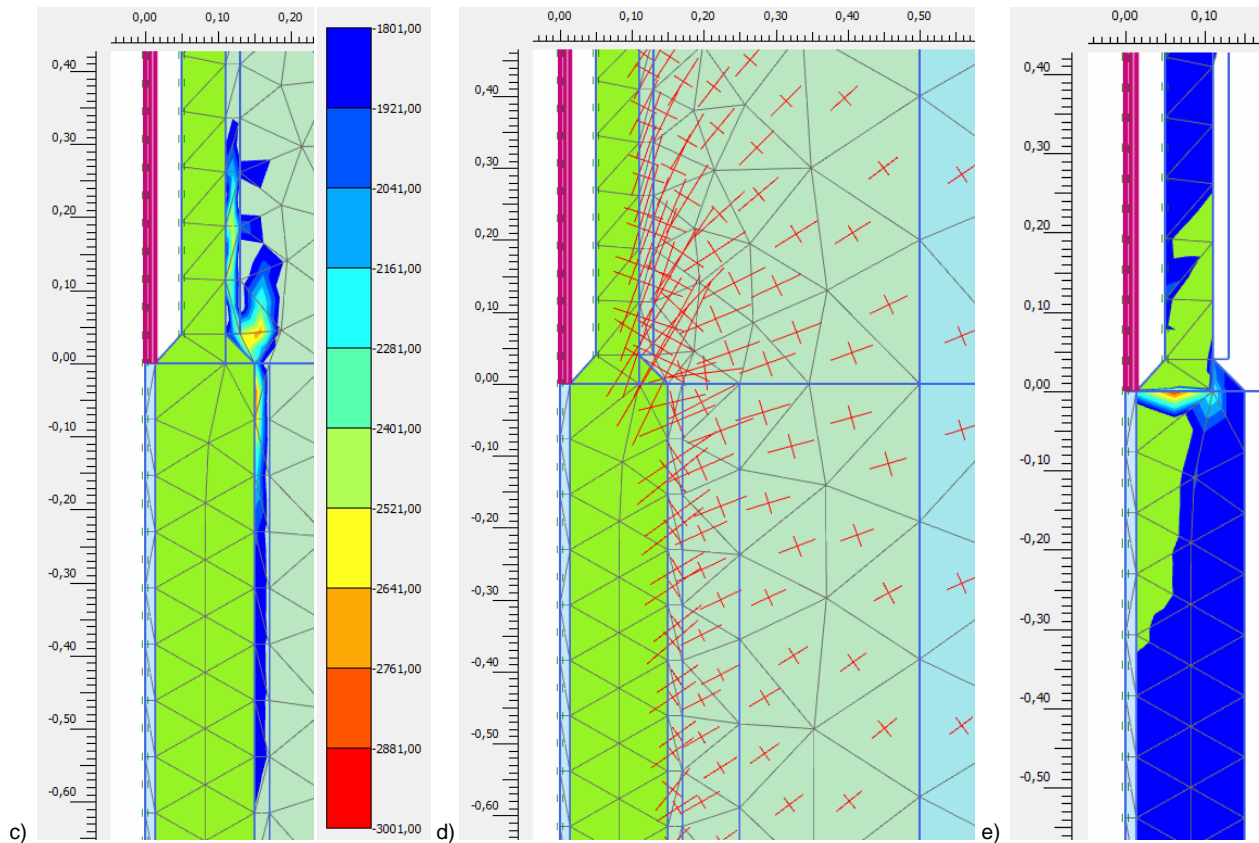


Fig. 6.9. *FreeL - coarse SC*: top of fixed length at a displacement of 2.4 cm: a) deformed mesh (scaled up 5 times), b) total displacements  $u_x$  c) normal pre-consolidation stress, hardening only, plane 1, d) effective principal stresses in soil adjacent to top of fixed length (scaled up  $0.25e-3$ ), e) compression hardening/softening parameter  $H_c$  (green: softening)

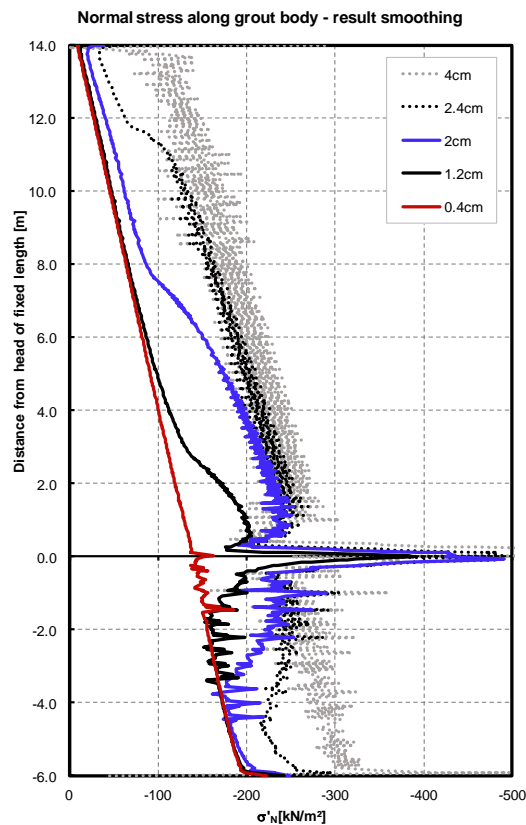


Fig. 6.10. *FreeL - coarse SC*: normal stress along grout body

As already mentioned, the stress in the grout differs significantly when changing the mesh fineness. Two points are selected in order to represent these differences, one in the junction between free and

fixed length (point M) and the other one 8 cm above it (point S). Fig. 6.11 shows the principal stresses in the coarse mesh, which can be compared to the fine mesh in Fig. 6.22. In spite of this mesh dependency concerning those stress points, the ultimate load bearing capacity of the anchor and the overall stiffness is much less affected.

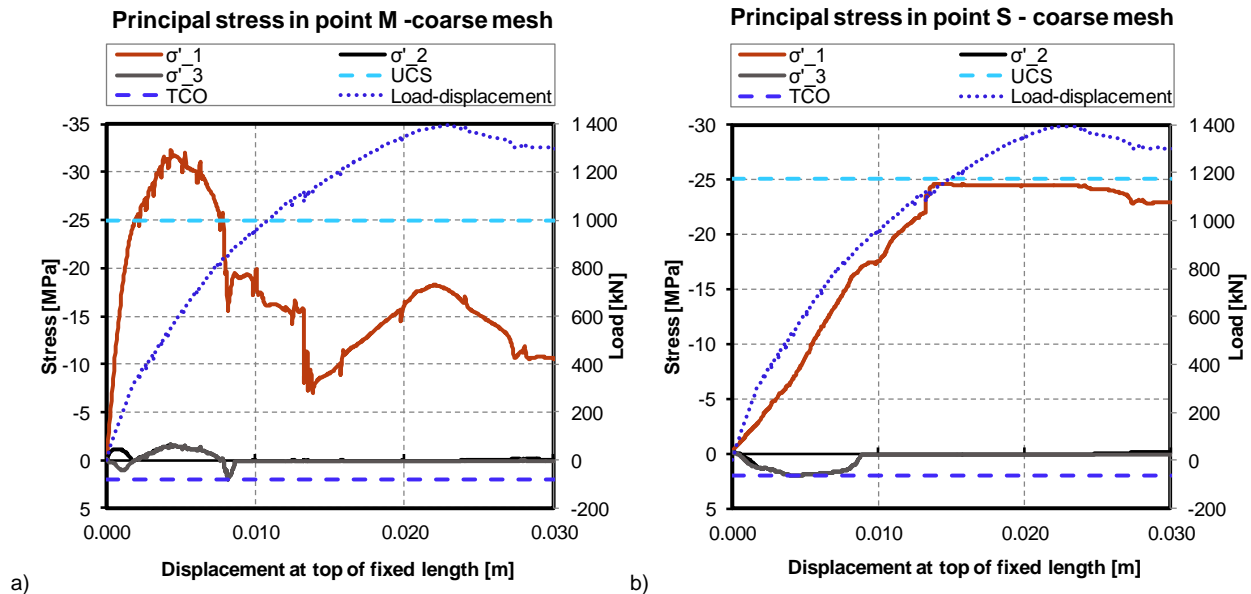


Fig. 6.11. *FreeL*- coarse SC: stress in free length: a) Point M, b) Point S

In conclusion, even the finest mesh possible might not be sufficient for detailed analyses. However, a finer mesh is not feasible for the given, slender geometries in PLAXIS.

## 6.4 Softening and dilatancy – MLSM

This section analyses the model *FreeL MC* in terms of softening and dilatancy of the MLSM, comparable with the evaluation of the model *Reference MC* in section 5.4.

The curves of the stress points plotted in Fig. 6.12 are corresponding to the reference model (see Fig. 5.9, Tab. 5.6). Fig. 6.12a shows a representation of the shear stress in point K in the soil adjacent to the top of the fixed length against the displacement equivalent to Fig. 5.10a of the model *Reference MC* without grout in the free length. They are qualitatively similar, but the peak is reached at a larger prescribed displacement. The reason is the shear stress that is transferred by the grout in the free length. The load-displacement curve, referenced to the secondary ordinate, is also displayed in Fig. 6.12a.

Point L, which is at the same elevation as point K but located at the edge of the shear band, exhibits a little lower shear stress. The normal stress  $\sigma'_{xx}$  in these points increases due to dilatancy (see Fig. 6.12b). However, it decreases again in point L. The reason is high oscillation in the normal stress distribution, which is even present when using result smoothing (see Fig. 6.14b).

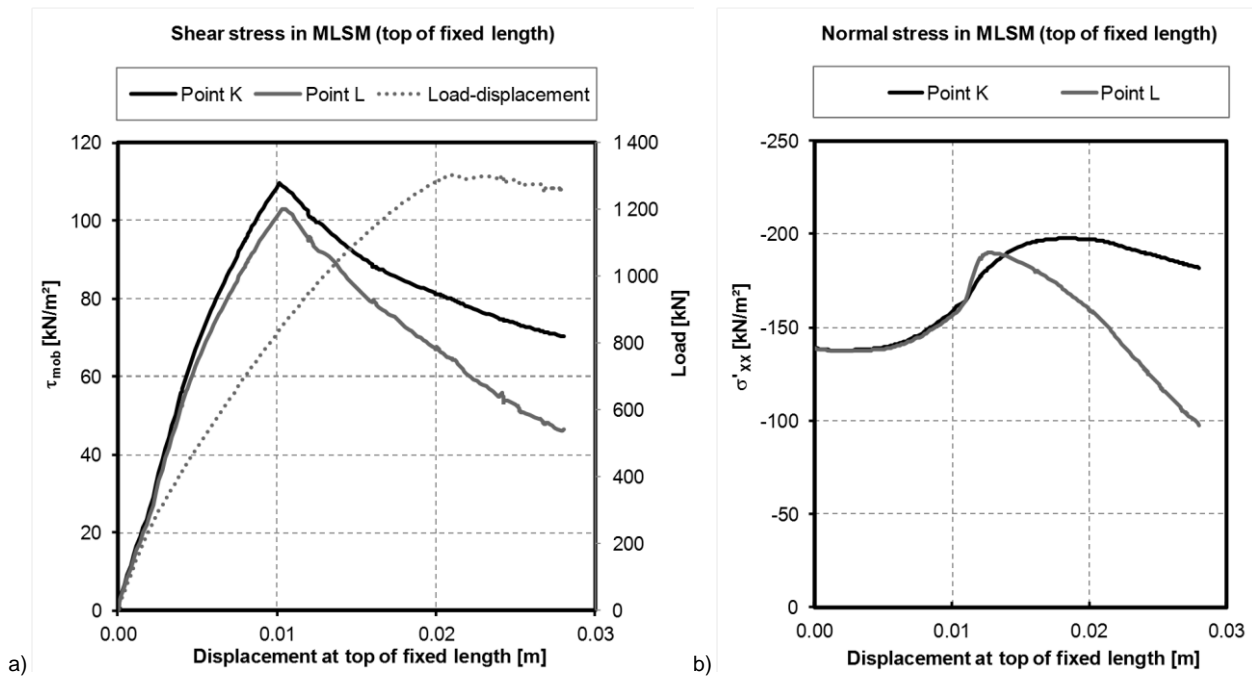


Fig. 6.12. *FreeL MC*: stress next to top of the grout body (points K, L) vs. displacement at top of fixed length: a) shear stress and load-displacement curve, b) normal stress

Fig. 6.13 shows the junction between free and fixed length of the model *FreeL MC* in terms of deformed mesh, total displacements in horizontal direction, normal pre-consolidation stress, effective principal stresses in the soil and failure point history at a post-peak displacement of 2.4 cm.

The mesh primarily deforms in vertical direction. At this state, a displacement of approximately 2.4 mm in perpendicular direction to the prescribed displacement has developed, because the soil is pushed aside. For this reason, hardening occurs in this area, which is shown for plane 1 in Fig. 6.13c. The major effective principal compressive stresses in the adjacent soil have aligned horizontally.

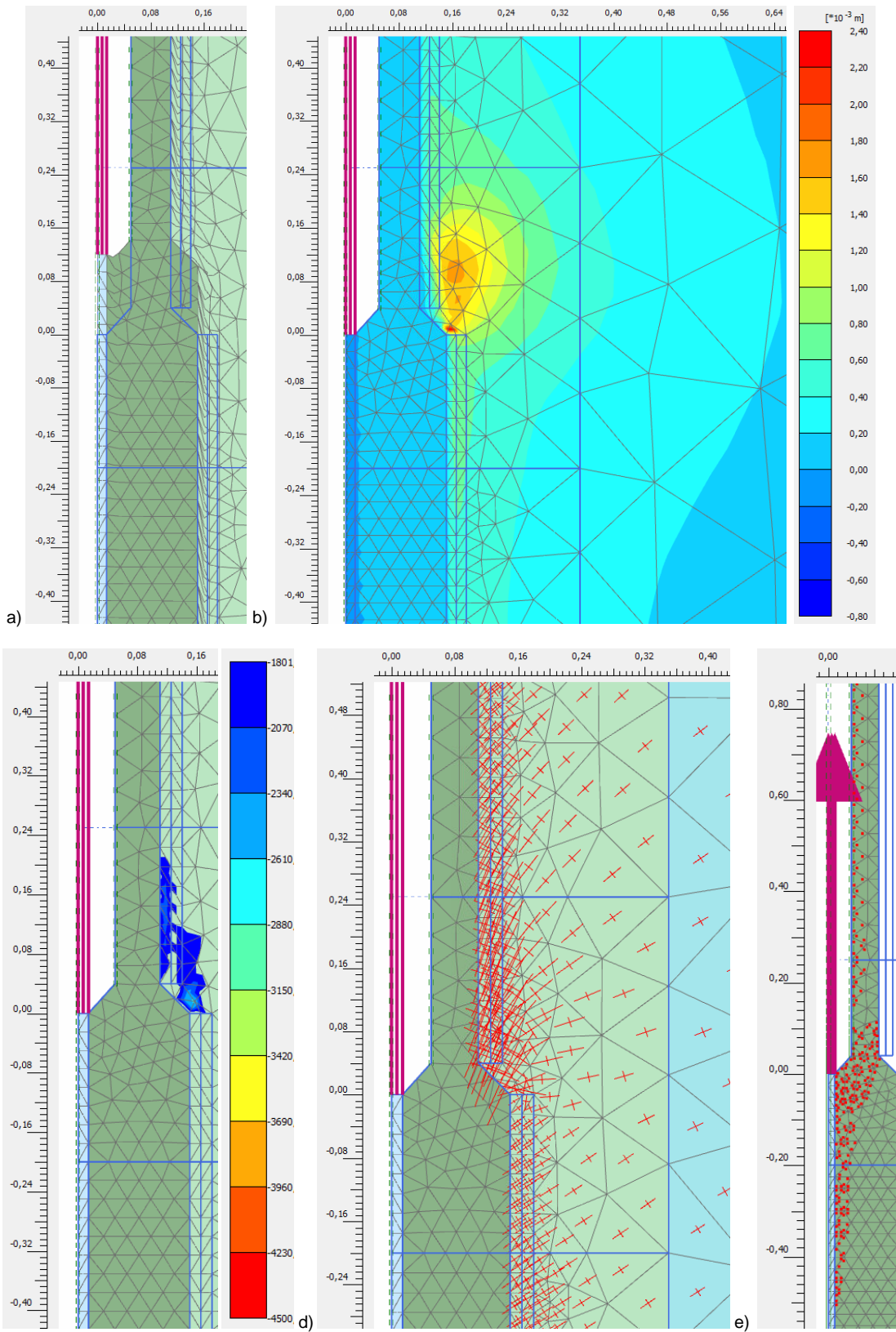


Fig. 6.13. *FreeL MC*: top of fixed length at a displacement of 2.4 cm: a) deformed mesh (scaled up 5 times), b) total displacements  $u_x$ , c) normal pre-consolidation stress, hardening only, plane 1, d) effective principal stresses in soil adjacent to top of fixed length (scaled up  $0.125 \times 10^{-3}$ ), e) failure point history

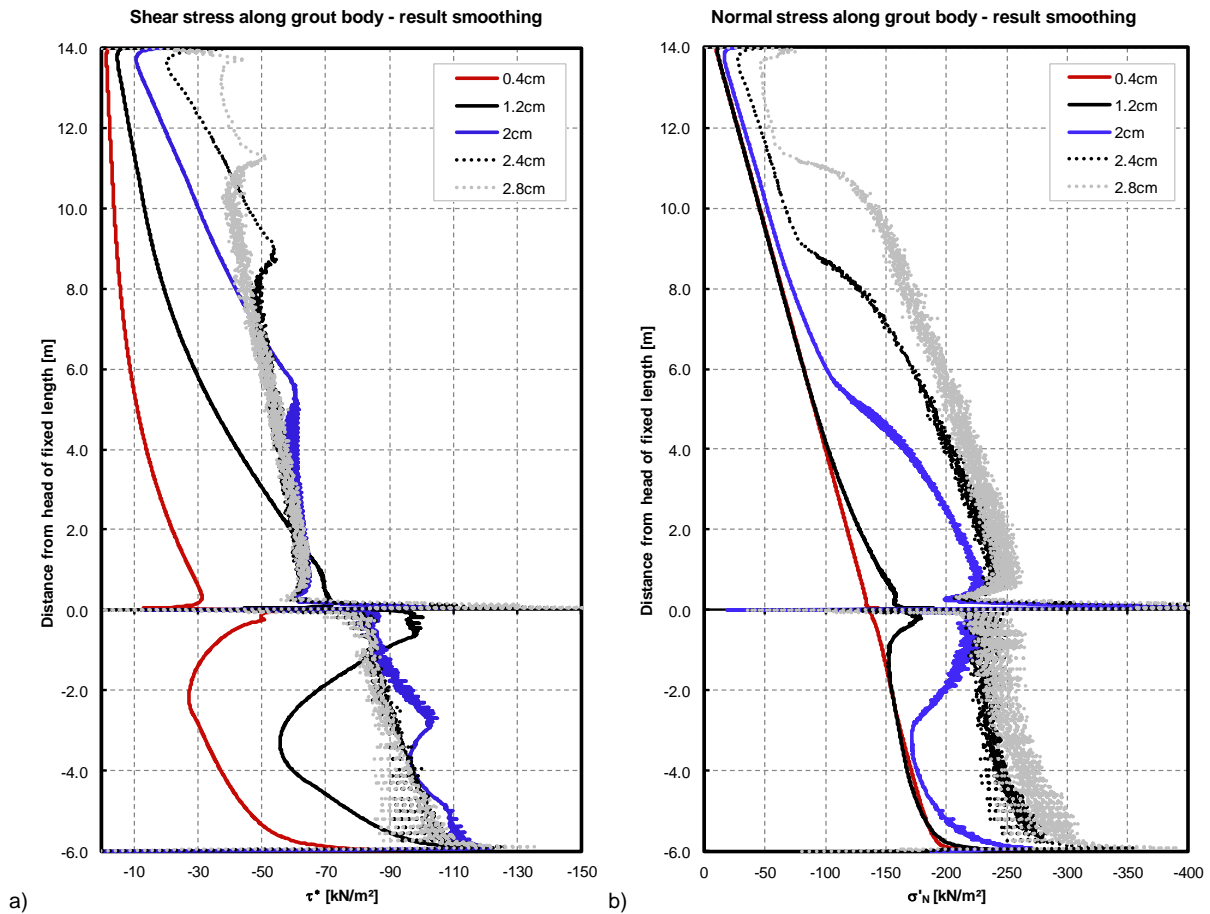


Fig. 6.14. *FreeL MC*: stress along grout body: a) shear stress (normalised by respective grout body surface), b) normal stress

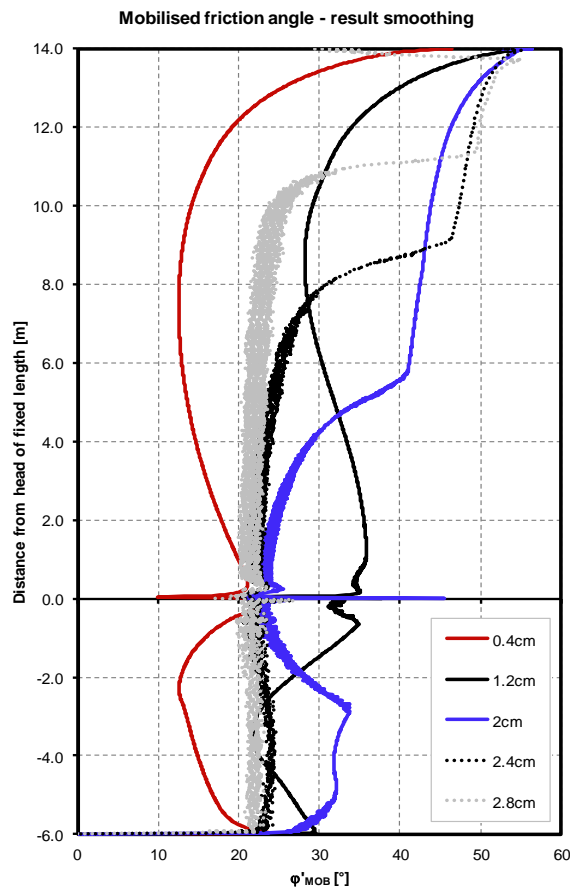


Fig. 6.15. *FreeL MC*: mobilised friction angle along grout body

Failure points have occurred in the grout in the junction between free and fixed length. The failure mechanisms arising in this area when using the SC model is discussed in section 6.5.

The stress distribution in the soil of the model *FreeL MC* is plotted along the whole grout body in Fig. 6.14. The shear stress is normalised by the respective circumference of the grout body in order to show the proportion of the load transfer between fixed and free length. The progressive failure mechanism spreads from the force application point in the free length upwards as well as in the fixed length downwards. The mobilised friction angle along the grout body is derived from this stress distribution (see Fig. 6.15). It looks similar to the basic model along the fixed length (cf. Fig. 5.7). The mobilised friction angle in the area of the free length is much higher than in the fixed length, because the OCR differs significantly between the very top and the bottom of the whole anchor. The reason is that the POP is specified for the whole soil in the model's input parameters instead of the OCR. This issue is diminished by shortening the free length to 14 m instead of 15 m. Furthermore, the POP could be reduced in the uppermost soil layer. This is a reason for the difference in post-peak behaviour of the load-displacement curves between the basic and advanced model.

The junction between free and fixed length, which has already been analysed in Fig. 6.13, is observed in detail in terms of stresses. Thus, several stress points are selected. Their coordinates are listed in Tab. 6.8 and sketched in Fig. 6.16.

Tab. 6.8. Location of selected stress points and cross-section for comparison

Coordinates	x	y
M	0.04	0.01
N	0.05	0.04
O	0.07	0.04
P	0.08	0.04
Q	0.10	0.04
R	0.08	0.12
S	0.09	0.12
Cross-section	0.05	0.04
	0.11	0.04

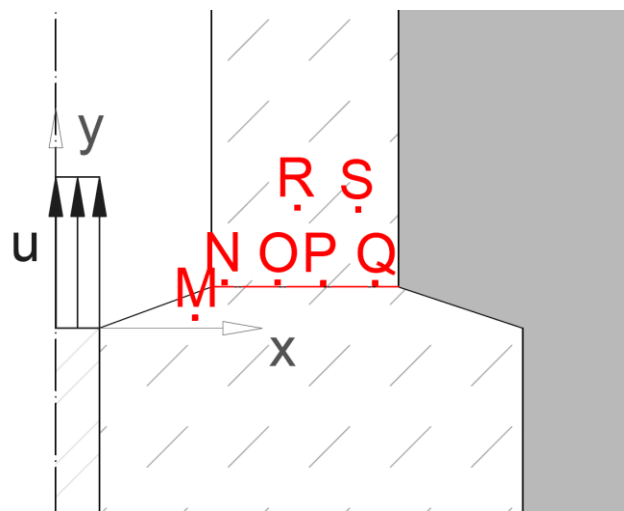


Fig. 6.16. Observed stress points and cross section

Fig. 6.17 shows the principal stresses in four of the selected stress points against the displacement at top of the fixed length. UCS and TCO are also indicated. Point M, close to the point of load application, reaches the defined TCO quickly and stays at this value. Hence, the major principal stress  $\sigma'_1$  cannot be increased any further. Point N exhibits almost the same curves, because they are close to each other. Point Q is at the same elevation, but with hardly any tension. The UCS is exceeded, because of the confining pressure. Point S exhibits similar stresses, but none beyond UCS.

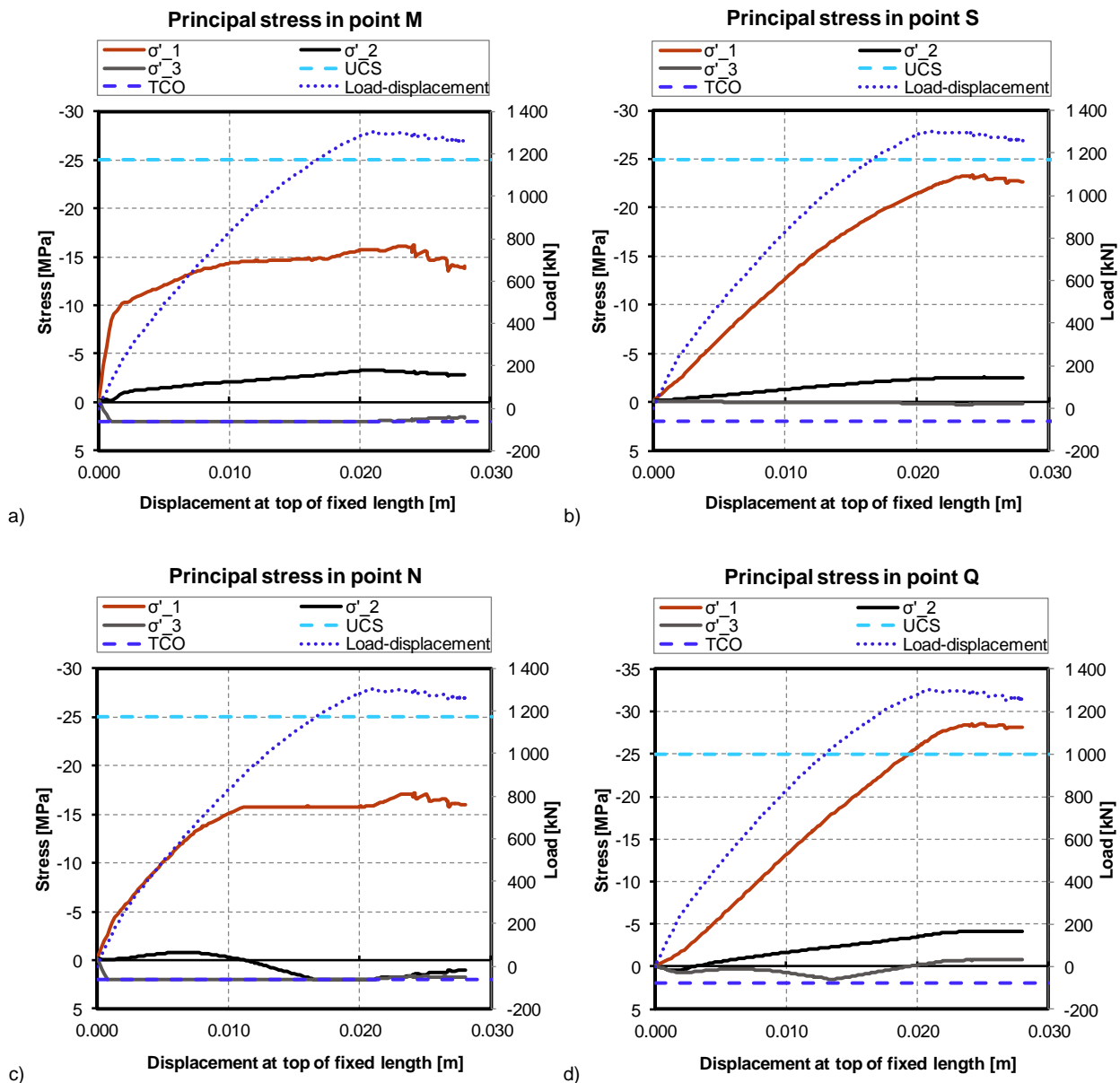


Fig. 6.17. *FreeL MC*: Principal stress in selected points in grout (junction between fixed and free length) and load-displacement curve (secondary ordinate) vs. displacement at top of fixed length: a) point M, b) point S, c) point N, d) point Q

## 6.5 Compression softening – SC model

The inner load bearing capacity of the grout is not supposed to be decisive, but as the capacity of the free length is usually not taken into account in the model considerations, especially the junction between fixed and free length is a key factor for load transfer and thus observation.

This section is focused on the model *FreeL SC* and its difference to the model *FreeL MC* in order to determine the impact of the SC model. As already mentioned, using the SC model in the present comparison results in a decrease in stiffness and even slightly in ultimate bearing capacity. Similar to the tension softening parameter  $H_t$ , the SC model features a compression hardening/ softening parameter  $H_c$  as well. Hardening is indicated in the range of 0 to 1 and softening above that threshold. Fig. 6.19e shows a plot with the softened areas in green.

The stress in the soil next to the top of the fixed length of the model *FreeL SC* is displayed in Fig. 6.18. The curves are shaped just as in the model *FreeL MC* (cf. Fig. 6.12), but the peak shear stress is reached earlier when using the SC model.

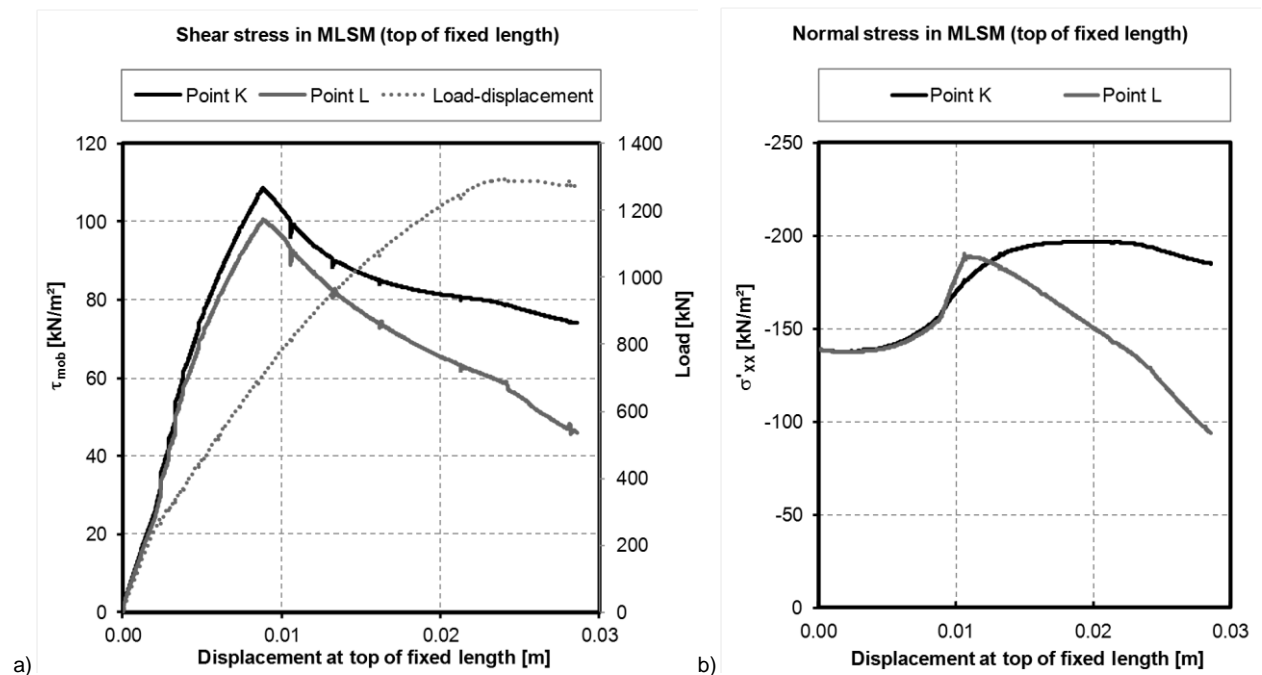


Fig. 6.18. *FreeL SC*: stress next to top of the grout body (points K, L) vs. displacement at top of fixed length: a) shear stress and load-displacement curve, b) normal stress

The plots of the deformed mesh, the total displacements in horizontal direction, the normal pre-consolidation stress and the effective principal stresses in Fig. 6.13a to d of the model *FreeL MC* are almost the same when using the SC model, which is why they are not represented here. However, there is a difference in failure point history as shown in Fig. 6.19a and Fig. 6.13e. More points in the grout have reached the failure line when using the MC model.

Fig. 6.20 shows the stress distribution in the soil along the grout body of the model *FreeL SC*. The oscillations in the fixed length are caused by the simulation of cracks in the grout body again. Compared to the model *FreeL MC* in Fig. 6.14, the average normal stress caused by dilatancy at top of the fixed length is slightly increased. Furthermore, dilatant behaviour along with softening in the free length has progressed further at the same state in the model *FreeL MC*. Using the SC model changes the progressive failure mechanism slightly in the fixed length, as the progression of the peak is less pronounced. The same can be seen when comparing the mobilised friction angle in Fig. 6.21 and Fig. 6.15. The reason is the lowered stiffness of the cracked grout body in the fixed length. This change in failure progression has already been investigated in section 5.6.

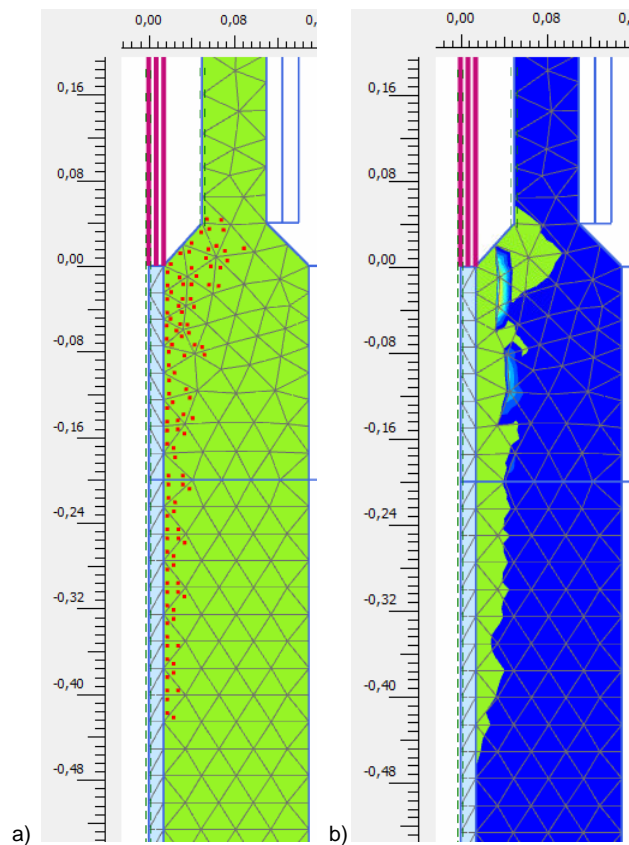


Fig. 6.19. *FreeL SC*: top of fixed length at a displacement of 2.4 cm: a) failure point history, b) compression hardening/ softening parameter  $H_c$  (green: softening)

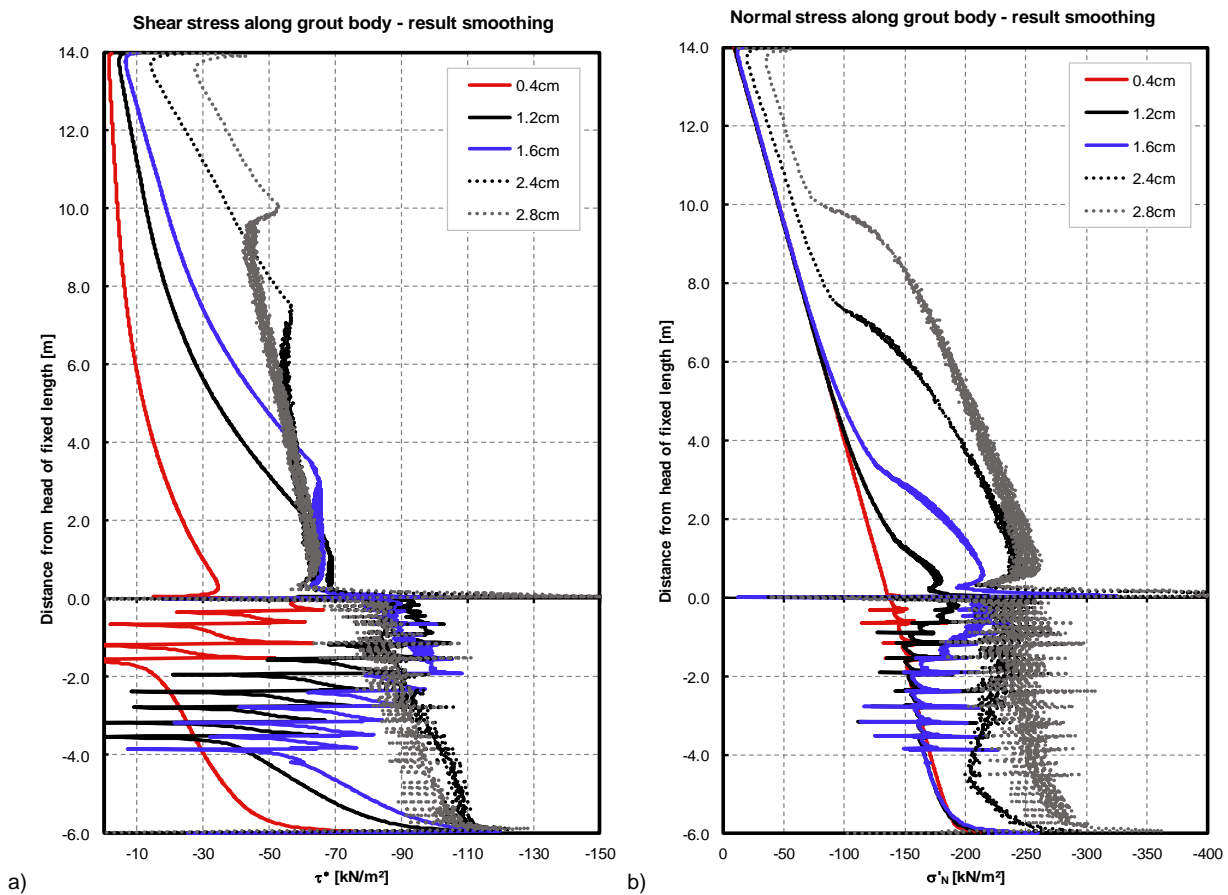


Fig. 6.20. *FreeL SC*: stress along grout body: a) shear stress (normalised by respective grout body surface), b) normal stress

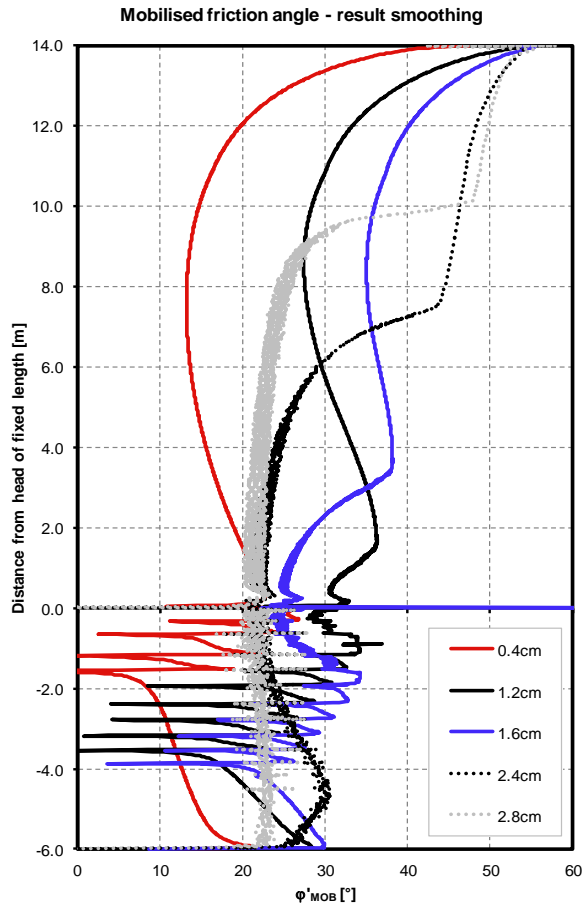
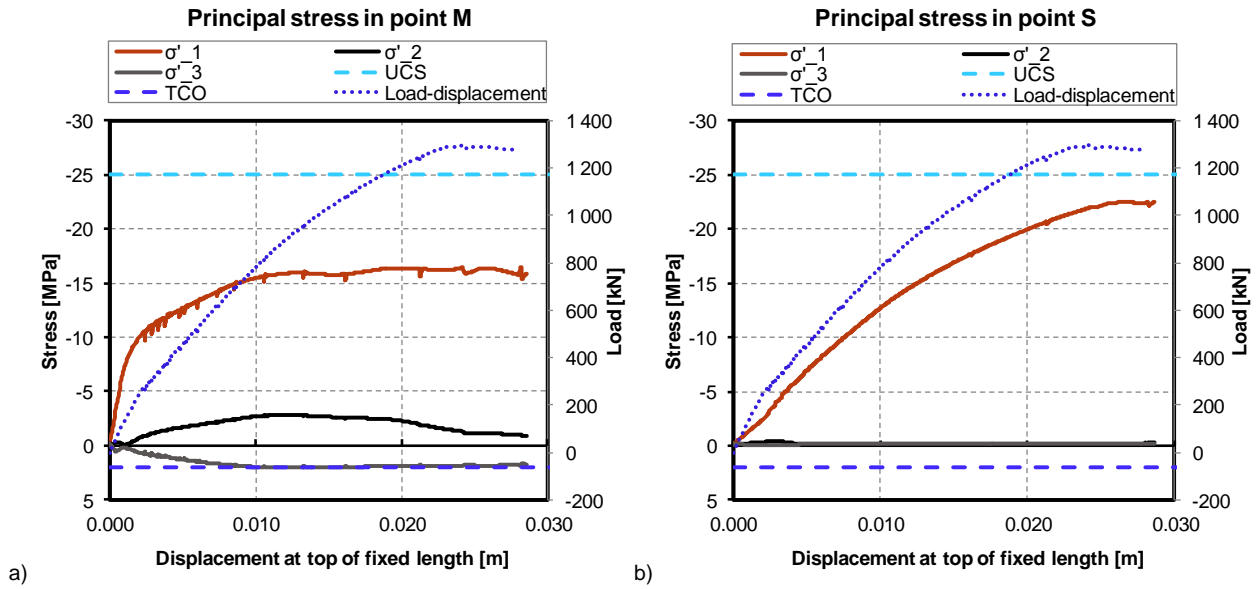


Fig. 6.21. *FreeL* SC: mobilised friction angle along grout body



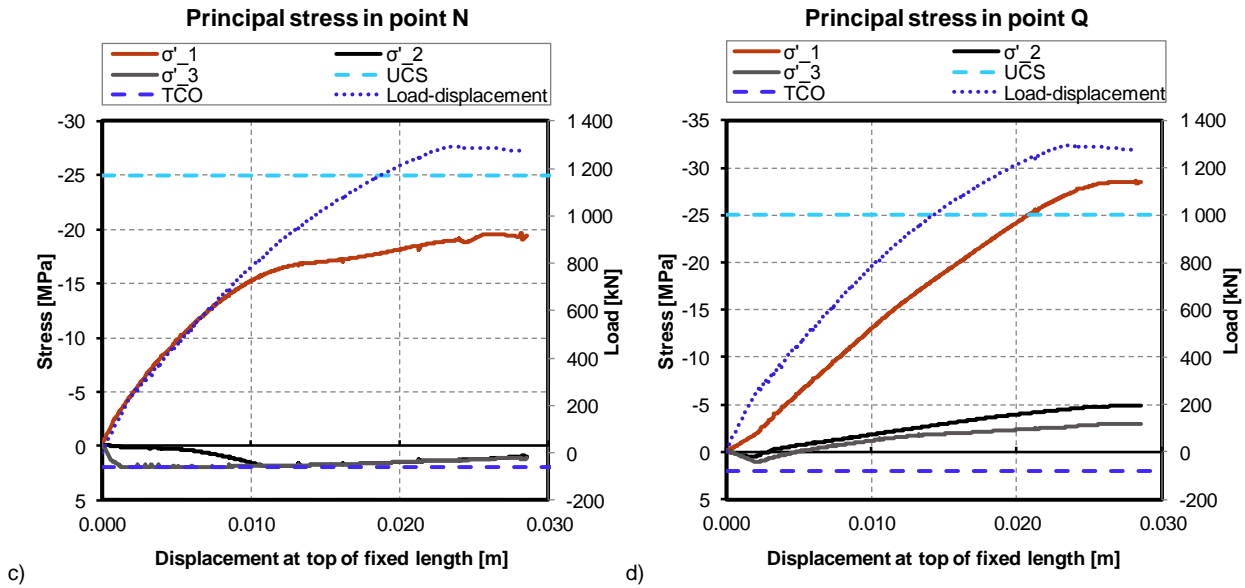


Fig. 6.22. *FreeL SC*: Principal stress in selected points in grout (junction between fixed and free length) and load-displacement curve (secondary ordinate) vs. displacement at top of fixed length: a) point M, b) point S, c) point N, d) point Q

The same analysis for the stress points (see Tab. 6.8) as in Fig. 6.17 for *FreeL MC* is conducted for the model *FreeL SC* as well (see Fig. 6.22). The minor principal stresses in the selected stress points in both models are very similar. Yet, the other principal stresses differ, but are comparatively small.

Fig. 6.23 shows Mohr's circles for the peak stress in point Q, the outermost stress point at the junction between free and fixed length, for both *FreeL SC* and *FreeL MC*. As the two material models behave differently, the peak stresses occur at different anchor load levels, which is 0.28 cm for the SC model and 0.25 cm for the MC model. Furthermore, the circle of UCS is pictured. Both models exceed this stress, since confining pressure occurs. Only the point in the model *FreeL MC* has reached the failure line. The load in the free length of this model is higher at that stage, which can be deduced from Fig. 6.4.

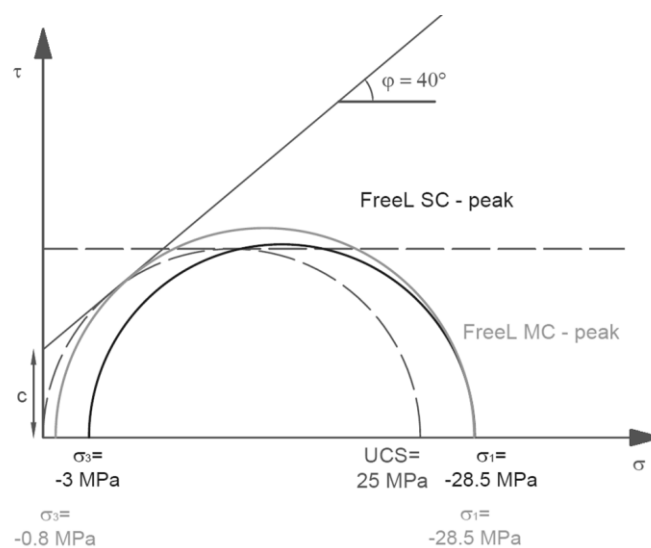


Fig. 6.23. *FreeL SC* and *FreeL MC*: Mohr's circle for peak stress in point Q

The compression hardening/ softening parameter  $H_c$  along the junction between free and fixed length (cross section: see Tab. 6.8) is displayed for different prescribed displacements and the values at the

left and right edge are plotted against the displacement. The same is done with the current yield stress  $f_{cy}$  and shown in Fig. 6.24. The compression hardening/ softening parameter  $H_c$  increases and thereby the uniaxial yield stress  $f_{cy}$  mobilises, which stops when  $H_c$  has reached 1. Softening starts afterwards, but this is not captured by the yield stress. It even exceeds UCS due to the set tolerance.

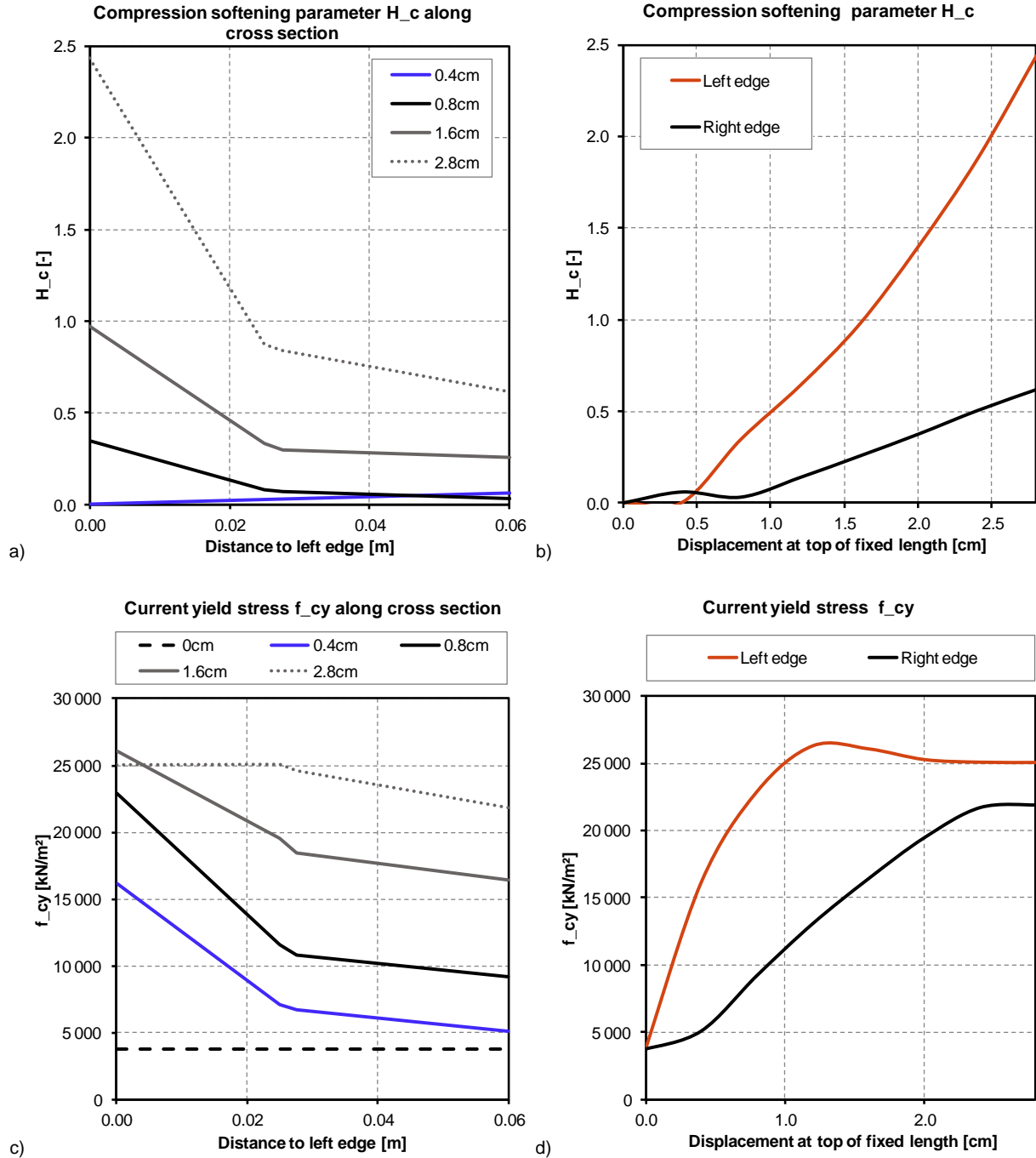


Fig. 6.24. *FreeL SC*: parameters along cross section at top of fixed length and vs. displacement at top of fixed length: a) compression hardening/ softening parameter  $H_c$  along cross section, b) left and right edge vs. displacement at top of fixed length, c) current yield stress  $f_{cy}$  along cross section, d) left and right edge vs. displacement at top of fixed length

## 6.6 Geometry alteration

Two models are prepared in order to evaluate the influence of the implementation of the free length as described in section 4.1. Fig. 6.25a shows the mesh of the reference model *FreeL SC/HS* with the void in the free length and the horizontal support of the grout. The modified model *FreeL- no support*

SC/HS has no support conditions in the free length (see Fig. 6.25b). The same applies to the model *FreeL- width- no support SC/HS* with the addition of reducing the void in the free length to the area of the tendon (see Fig. 6.25c). These modifications are listed in Tab. 6.9.

Tab. 6.9. Free length: changed conditions for comparison

Model	Changed parameter	Unit	Initial value	Changed value
<i>FreeL - no support SC/HS</i>	Support condition free length	-	Horizontally fixed	No support
<i>FreeL- width- no support SC/HS</i>	Support condition free length	-	Horizontally fixed	No support
	Width free length	m	0.060	0.096

Fig. 6.26 shows the load-displacement curves of the three compared models and their peak values are listed in Tab. 6.10. The vertical support in the free length has no impact on this calculation. As the bearing capacity of the interface between soil and grout is lower, the grout is not decisive in the present case. Thus, the ultimate bearing capacity is almost the same in all models.

Tab. 6.10. Geometry alterations in free length: comparison of the load bearing capacity and the respective displacement at top of the fixed length

Model	Displacement at peak [m]	Difference	Bearing capacity [kN]	Difference
<i>FreeL SC/HS</i>	0.018	-	1 075	-
<i>FreeL- no support SC/HS</i>	0.018	±0 %	1 075	±0 %
<i>FreeL- width- no support SC/HS</i>	0.030	+65 %	1 070	-0 %

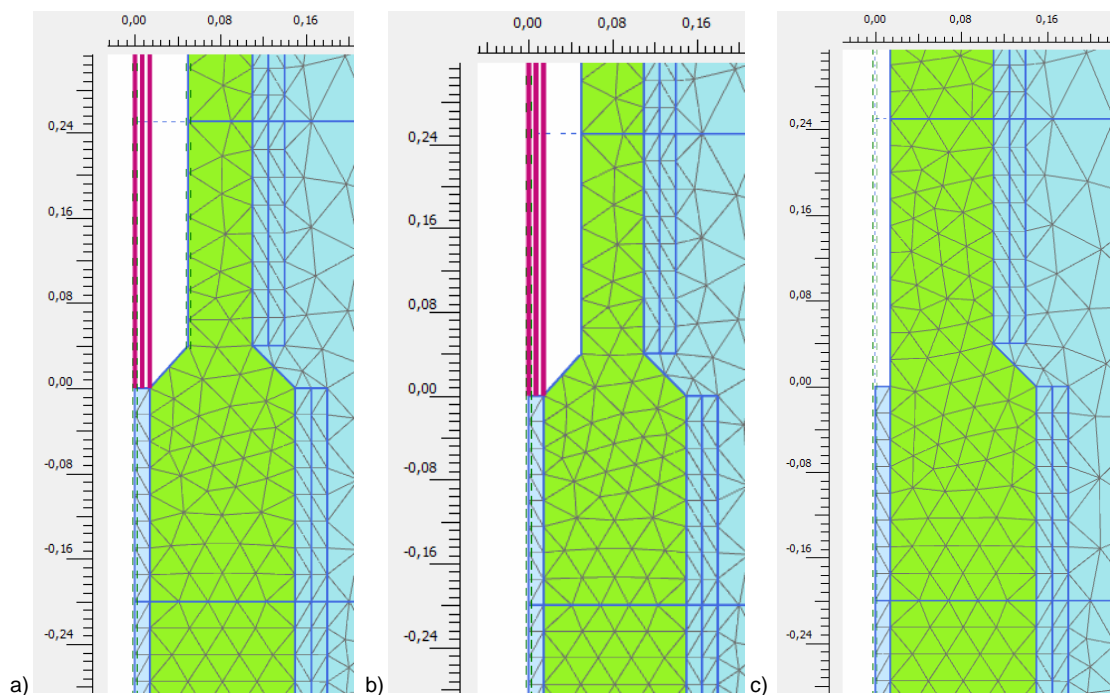


Fig. 6.25. Detail (top of fixed length) of compared models with grout in the free length: a) *FreeL SC/HS*, b) *FreeL- no support SC/HS*, c) *FreeL- width- no support SC/HS* (prescribed displacement not displayed)

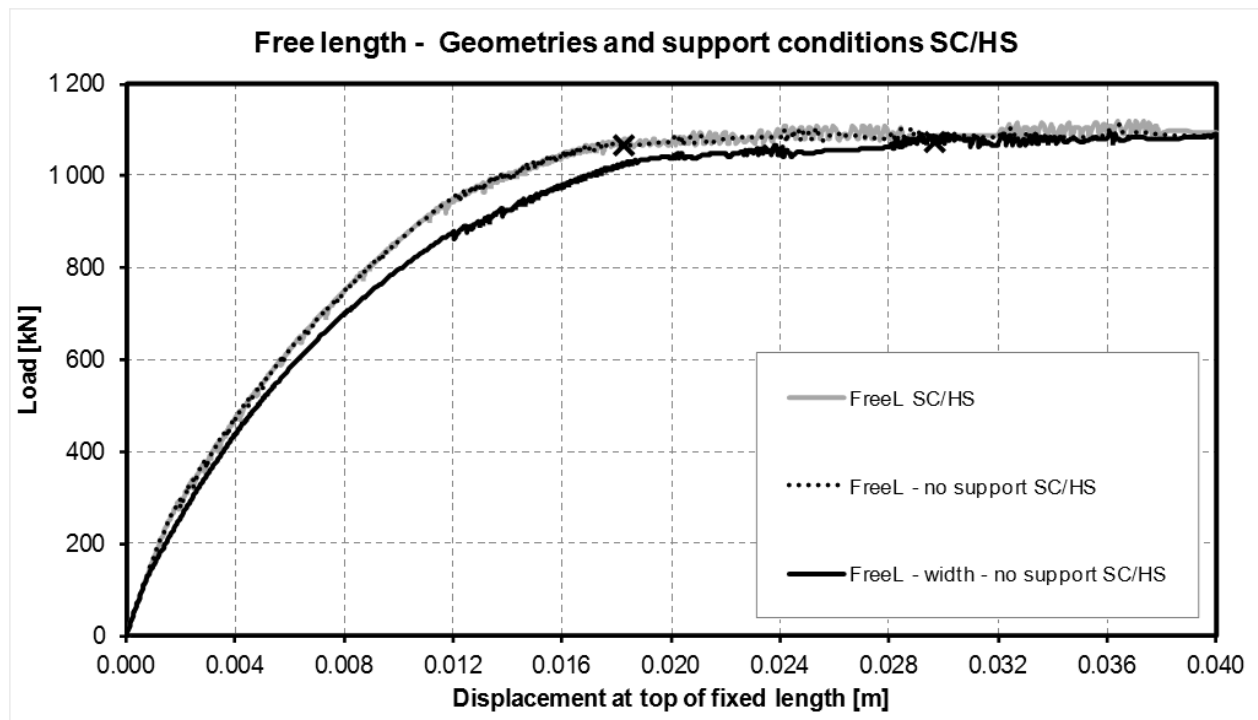


Fig. 6.26. Load-displacement curves of geometries and support condition alterations

However, increasing the area of the free length changes the behaviour of the system as can be seen by the load-displacement curve of the model *FreeL- width- no support SC/HS*. This modification is supposed to increase the stiffness, since the axial stiffness is raised by 24 % compared to the area of the grout in the free length in the reference models, as calculated in Tab. 4.2. The same applies to the force at failure. The difference in behaviour of the models *FreeL SC/HS* and *FreeL- width- no support SC/HS* is shown in Fig. 6.29 and Fig. 6.30 and analysed hereafter.

The first crack in the fixed length occurs when a prescribed displacement of 0.2 cm is applied in the model *FreeL SC/HS*, but at 1.2 cm with an enlarged area of the grout in the free length. This can also be recognised in the load-displacement curve. The reason is the increase in axial stiffness of the free length that causes a different stress distribution in the grout. The load proportion in the free length is initially higher, which can be seen in Fig. 6.27. However, the curves align at a displacement of 1.2 cm, because failure occurs in the free length in the model *FreeL- width- no support SC/HS*. This failure is plotted in terms of compression hardening/ softening parameter  $H_c$  at various displacements in Fig. 6.28. The area exhibiting a value above 1 spreads, which indicates softening. Consequently, the free length buckles, which can be seen in Fig. 6.29. A similar analysis for the model *FreeL SC/HS* is conducted in Fig. 6.30, which differs significantly.

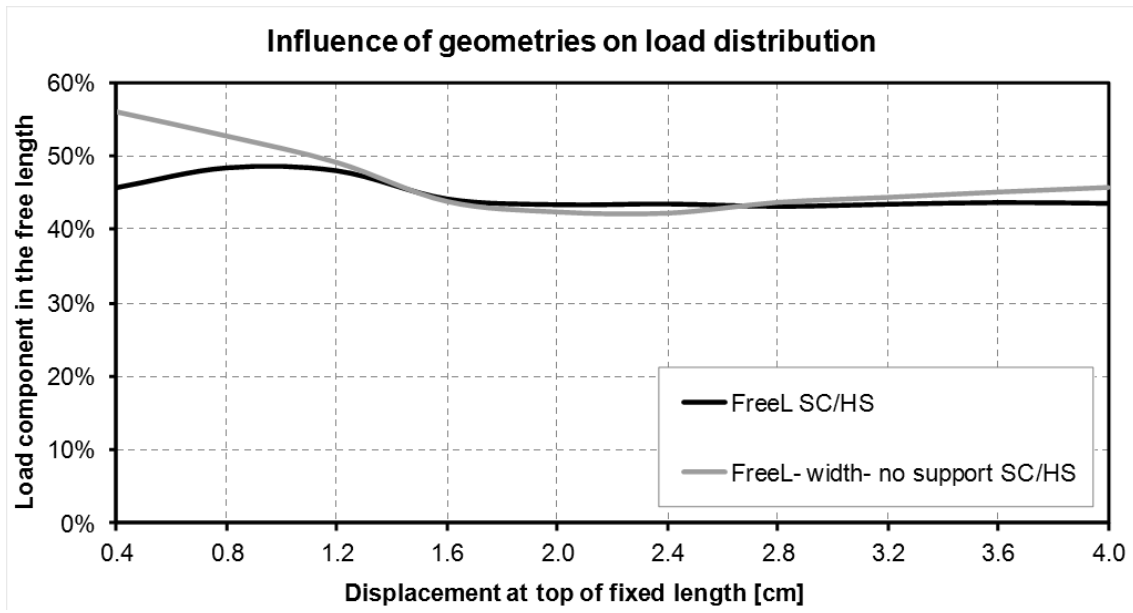


Fig. 6.27. Influence of geometries on load distribution

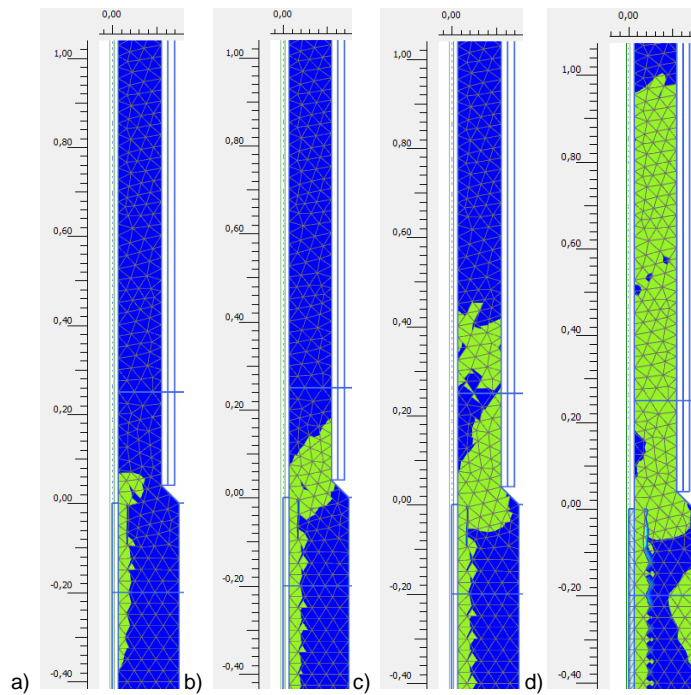


Fig. 6.28. *FreeL- width- no support SC/HS*: compression hardening/ softening parameter  $H_c$  (green: softening) at various displacements of 4 cm: a) 0.4 cm, b) 0.8 cm, c) 1.2 cm, d) 4 cm

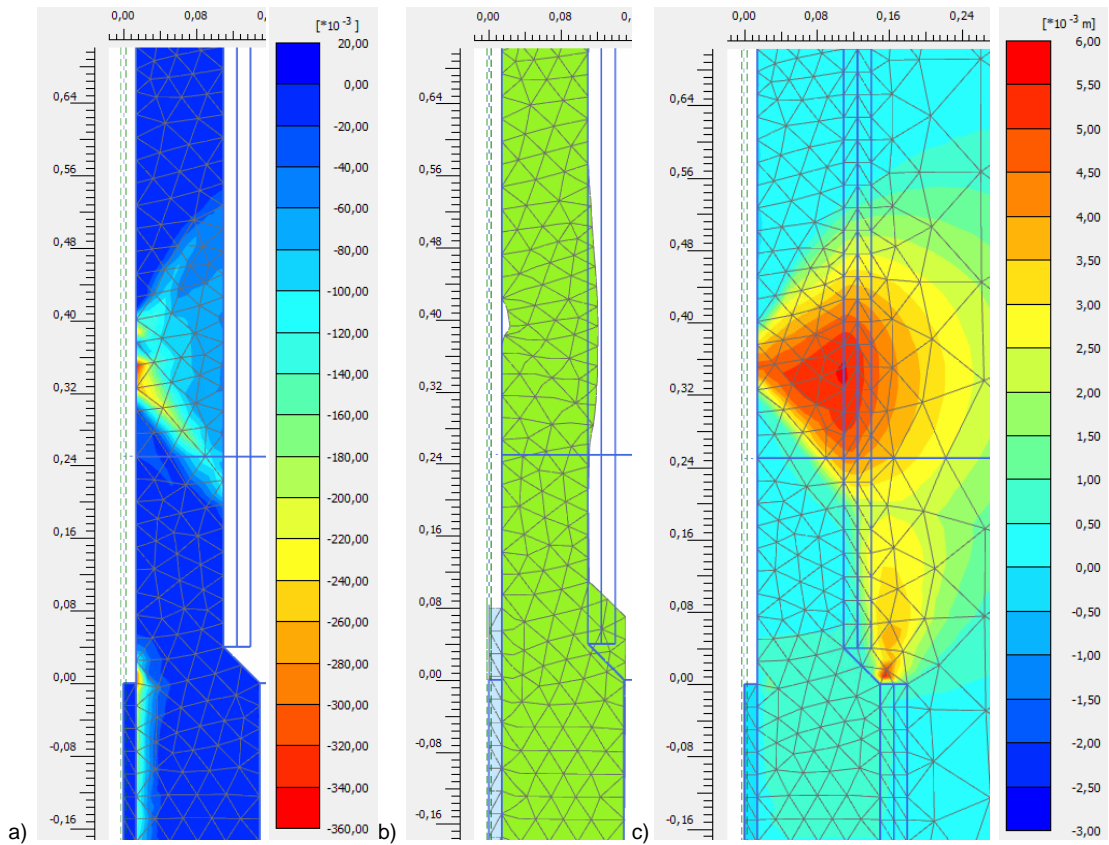


Fig. 6.29. *FreeL- width- no support SC/HS*: junction between free and fixed length at a displacement of 4 cm: a) total principal strain  $\varepsilon_1$ , b) deformed mesh (scaled up 2 times), c) total displacement  $u_x$

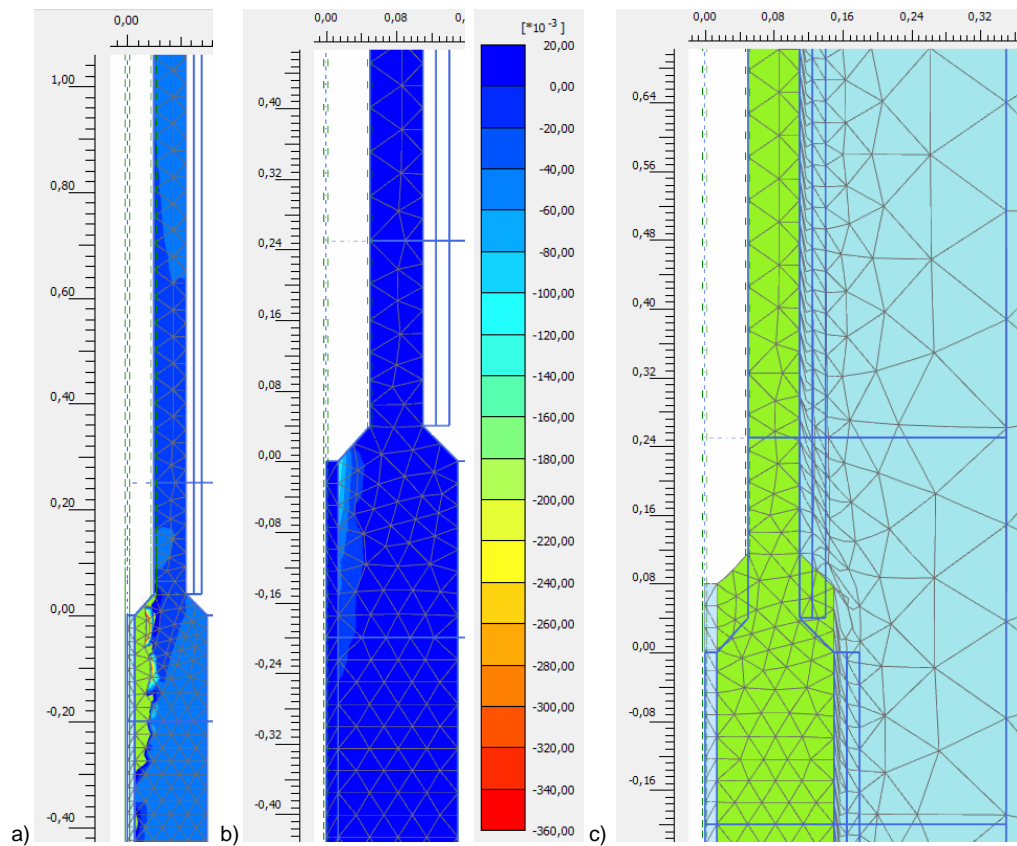


Fig. 6.30. *FreeL SC/HS*: junction between free and fixed length at a displacement of 4 cm: a) compression hardening/softening parameter  $H_c$  (green: softening), b) total principal strain  $\varepsilon_1$ , c) deformed mesh

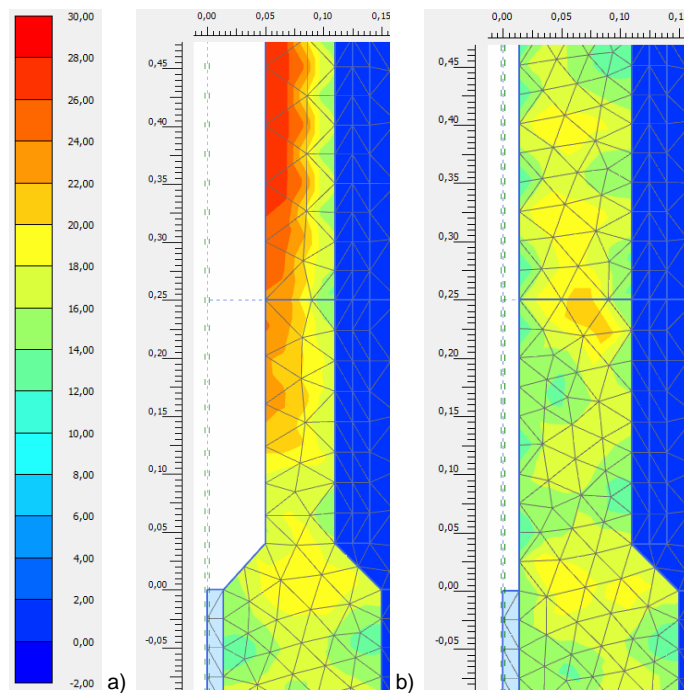


Fig. 6.31. Equivalent length  $L_{eq}$ : a) *FreeL SC/HS*, b) *FreeL-width-no support SC/HS*

As already mentioned, crack alignment along element boundaries is an open issue in the SC model (Schädlich and Schweiger 2014 b). The reason is that strains are localised in one stress point at the boundaries and otherwise in more, which increases the load that is necessary to generate failure. This effect can be seen in Fig. 6.29a. The equivalent length  $L_{eq}$ , depending on the number of stress points per finite element and the area of the element, is assigned to each stress point and used for regularisation in order to avoid mesh dependent results. Fig. 6.31 shows the calculated equivalent length  $L_{eq}$  in the compared models. The steepest and straightest continuous element boundary crossing the free length is most prone to strain softening and therefore the point of failure. There is no such element boundary at the same angle in the model *FreeL SC/HS*, which could be the reason for the different behaviour. However, the cause is assumed to be the lower load proportion in the free length in this model for the abovementioned reasons. This issue could be solved by a non-local strain regularisation approach, such as the multilaminar framework in the MLSM.

The real conditions in the free length being present on-site are neither easily determinable nor straightforwardly modelled. However, the calculations carried out in this thesis are focused on the load bearing capacity of the interface between soil and grout, which is why it is not very sensitive to changes in those model geometries.

## 6.7 SC material parameter alteration

Several material parameters of the SC model are modified separately in order to determine their impact on the ultimate load bearing capacity. The analyses are conducted using the reference model *FreeL SC/HS*. Five models are prepared, which are listed along with the parameter changes in Tab. 6.11. The difference between the models with a lower strength is that this change is restricted to the free length in the model *FreeL-strength Free SC/HS*.

Tab. 6.11. Free length: changed SC parameters for comparison

Model	Changed parameter	Unit	Initial value	Changed value
<i>FreeL- Gc SC/HS</i>	Compressive fracture energy $G_c$	kN/m	0.15	0.50
<i>FreeL- strength low SC/HS</i>	Uniaxial compressive strength $f_c$	kN/m <sup>2</sup>	25 000	10 000
	Uniaxial tensile strength $f_t$	kN/m <sup>2</sup>	2 000	800
<i>FreeL- strength Free SC/HS</i>	Uniaxial compressive strength $f_c$ of the free length	kN/m <sup>2</sup>	25 000	10 000
	Uniaxial tensile strength $f_t$ of the free length	kN/m <sup>2</sup>	2 000	800
<i>FreeL- ecp low SC/HS</i>	Uniaxial plastic failure strain $\varepsilon_{cp}^P$	-	-0.0010	-0.0005
<i>FreeL- a 0 SC/HS</i>	Increase of $\varepsilon_{cp}$ with increase of $p'$	-	16	0

The resulting load-displacement curves of the models are shown in Fig. 6.32 and listed in terms of displacement at peak and ultimate bearing capacity in Tab. 6.12. Except for the reduction in strength, none of the alterations has an impact on these factors. Thus, this chapter focuses on the influence of the set strength for the grout. As anticipated, there is hardly any difference in load bearing capacity when assigning a low strength to solely the free length or the whole grout body. However, the initial stiffness of the system is higher when the strength of the fixed length is not decreased, because the TCO is higher and cracking starts later. In additional, failure occurs in the models with lower strength at a prescribed displacement of 3.8 cm, which can be seen in their load-displacement curves.

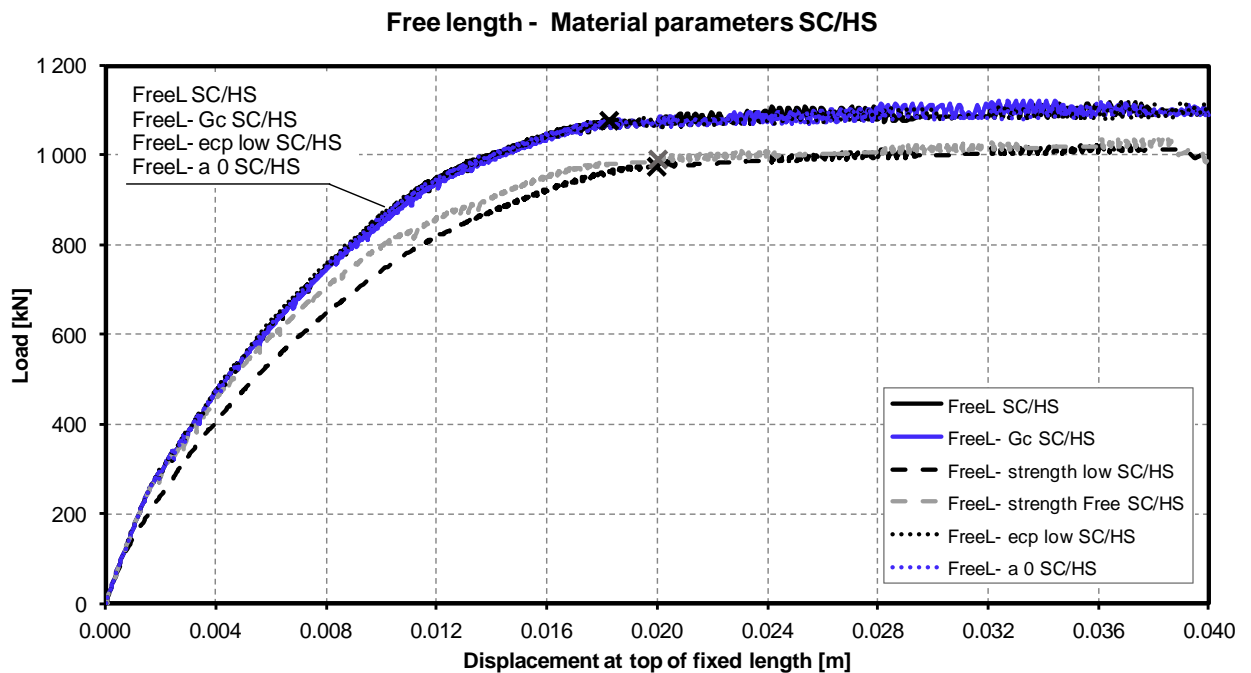


Fig. 6.32. Load-displacement curves of SC material parameter alterations

Tab. 6.12. SC material parameter alterations: comparison of the load bearing capacity and the respective displacement at top of the fixed length

Model	Displacement at peak [m]	Difference	Bearing capacity [kN]	Difference
<i>FreeL SC/HS</i>	0.018	-	1 075	-
<i>FreeL- Gc SC/HS</i>	0.018	±0 %	1 075	±0 %
<i>FreeL- strength low SC/HS</i>	0.020	+11 %	980	-9 %
<i>FreeL- strength Free SC/HS</i>	0.020	+11 %	990	-8 %
<i>FreeL- ecp low SC/HS</i>	0.018	±0 %	1 075	±0 %
<i>FreeL- a 0 SC/HS</i>	0.018	±0 %	1 075	±0 %

The model *FreeL- strength Free SC/HS* exhibits a similar failure mechanism to the model *FreeL- width- no support SC/HS* as presented in section 6.6, although the free length is horizontally supported in this case. Since the strength of the free length is exceeded, it buckles as shown in Fig. 6.33.

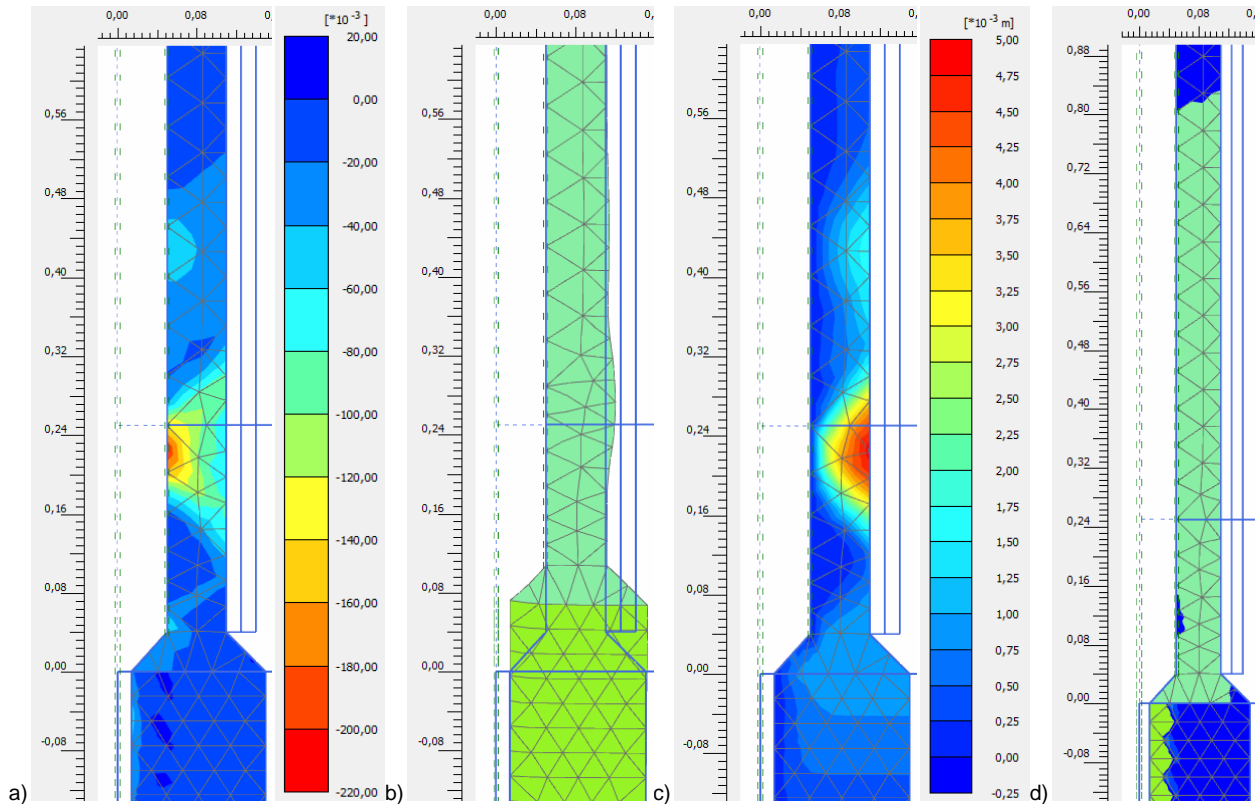


Fig. 6.33. *FreeL- strength Free SC/HS*: junction between free and fixed length at a displacement of 3.6 cm: a) total principal strain  $\varepsilon_1$ , b) deformed mesh (scaled up 2 times), c) total displacement  $U_x$ , d) compression hardening/softening parameter  $H_c$  (green: softening)

The lower strength of the free length reduces its load proportion from 45 to 40 %, as shown in Fig. 6.35. The maximum uniaxial load in the free length is calculated in Tab. 6.13, which is lower than its actual peak load due to the confining pressure. In conclusion, it is not the bearing capacity of the interface between soil and grout that is decisive in this case but the strength of the grout in the free length.

Tab. 6.13. *FreeL- strength low SC/HS*: load free length

<b><i>FreeL- strength low SC/HS</i>: load free length</b>		
Uniaxial compressive strength $UCS$	kN/m <sup>2</sup>	10 000
Area free length $A_{free}$	m <sup>2</sup>	0.03
Max. uniaxial load free length (= $UCS * A_{free}$ )	kN	302
Load proportion free length	%	40
Total load	kN	980
Load free length	kN	392

Fig. 6.34 shows Mohr's circles for the peak stress in point Q, the outermost stress point at the junction between free and fixed length, for the model *FreeL- strength Free SC/HS*. UCS is exceeded by far and the MC line is reached. The same analysis is conducted for the models *FreeL MC* and *FreeL SC* in Fig. 6.23.

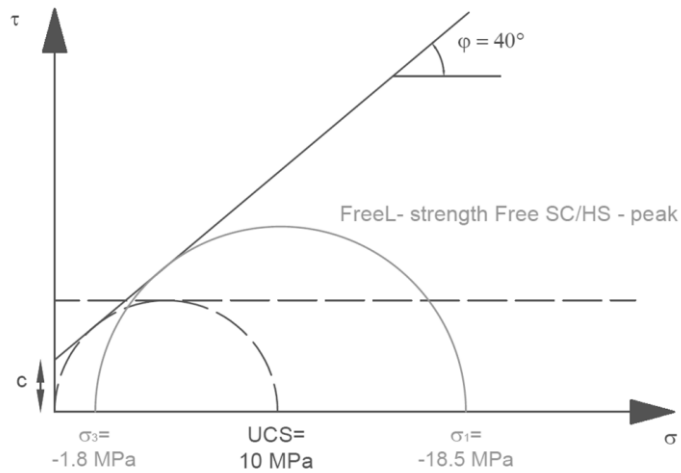


Fig. 6.34. *FreeL- strength Free SC/HS*: Mohr's circle for peak stress in point Q

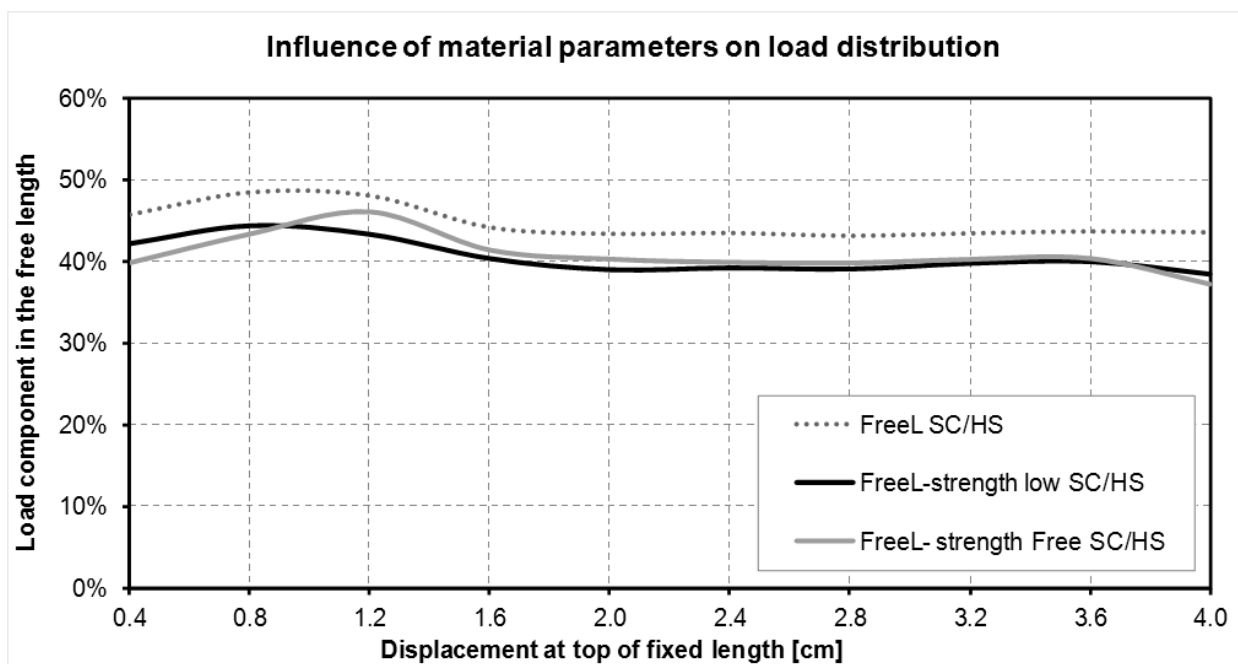


Fig. 6.35. Influence of material parameters on load distribution

## 6.8 Bearing capacity grout

The bearing capacity has already been an issue in the previous sections, although the calculations are focused on the capacity of the interface between soil and grout. The reason is that the conditions being present in the free length are not easily determinable. Hence, this section deals with cases that lead to failure in the free length. Two different approaches of implementation are shown in this section:

- **Bearing capacity interface soil-grout heightened:**  
The bearing capacity of the interface between soil and grout is increased by doubling the soil unit weight, which increases the stress acting perpendicular to the grout.
- **Deterioration of grout material properties:**  
A combination of worse grout material properties is assigned to the free length.

Tab. 6.14 gives an overview of the models and their changes compared to the reference model *FreeL SC/HS*.

Tab. 6.14. Free length: analyses of the bearing capacity of the grout

Model	Changed parameter	Unit	Initial value	Changed value
<i>FreeL- gamma x2 MC/HS</i>	Soil unit weight $\gamma$	kN/m <sup>3</sup>	15.24	30.48
<i>FreeL gamma x2 SC/HS</i>	Soil unit weight $\gamma$	kN/m <sup>3</sup>	15.24	30.48
<i>FreeL gamma x2 Gc SC/HS</i>	Soil unit weight $\gamma$	kN/m <sup>3</sup>	15.24	30.48
	Compressive fracture energy $G_c$	kN/m	50.00	8.00
<i>FreeL- worst case SC/HS</i>	Support condition free length	-	Horizontally fixed	No support
	Uniaxial compressive strength $f_c$	kN/m <sup>2</sup>	25 000	10 000
	Uniaxial tensile strength $f_t$	kN/m <sup>2</sup>	2 000	800
	Uniaxial plastic failure strain $\varepsilon_{cp}^P$	-	-0.001000	-0.000267
	Increase of $\varepsilon_{cp}$ with increase of $p'$ $a$	-	16	0
	Compressive fracture energy $G_c$	kN/m	50.00	8.00

The resulting load-displacement curves of the calculations are shown in Fig. 6.36 and their peak values listed in Tab. 6.15. The model *FreeL- worst case SC/HS* is compared to the model *FreeL-strength Free SC/HS*, as the strength of the free length is reduced in this case as well. The peak values are almost the same, but failure occurs in the model with the worsened material properties in the free length at that stage. The same happens to the model *FreeL- gamma x2 SC/HS*. Thus, these two models set the boundary conditions for which the interface between soil and grout is still decisive. However, when the compressive fracture energy  $G_c$  is reduced, failure occurs at an earlier stage. The failure mechanism in the grout is the same as described in the previous two sections. In the model *FreeL- gamma x2 MC/HS* the shear strength of the soil along the whole grout body is fully mobilised. On the contrary, the stresses in the uppermost 7 m of the soil along the free length in the model *FreeL- gamma x2 SC/HS* do not lie on the MC failure line.

Tab. 6.15. Bearing capacity of the grout: comparison of the load bearing capacity and the respective displacement at top of the fixed length

Model	Displacement at peak [m]	Difference	Bearing capacity [kN]	Difference
<i>FreeL- gamma x2 MC/HS</i>	0.032	-	2 056	-
<i>FreeL- gamma x2 SC/HS</i>	0.035	+10 %	2 050	±0 %
<i>FreeL- gamma x2 Gc SC/HS</i>	0.028	-12 %	1 819	-12 %
<i>FreeL- strength Free SC/HS</i>	0.020	-	990	-
<i>FreeL- worst case SC/HS</i>	0.017	-14 %	970	-2 %

Fig. 6.37 shows the curves of load component in the free length against the prescribed displacement of the analysed models. The crosses indicate failure of the grout in the free length and the circles of the interface between soil and grout. They can be distinguished easily, since the load component in the free length decreases sharply at point of failure. In the model *FreeL- strength Free SC/HS*, the interface fails first and the grout afterwards due to high strains.

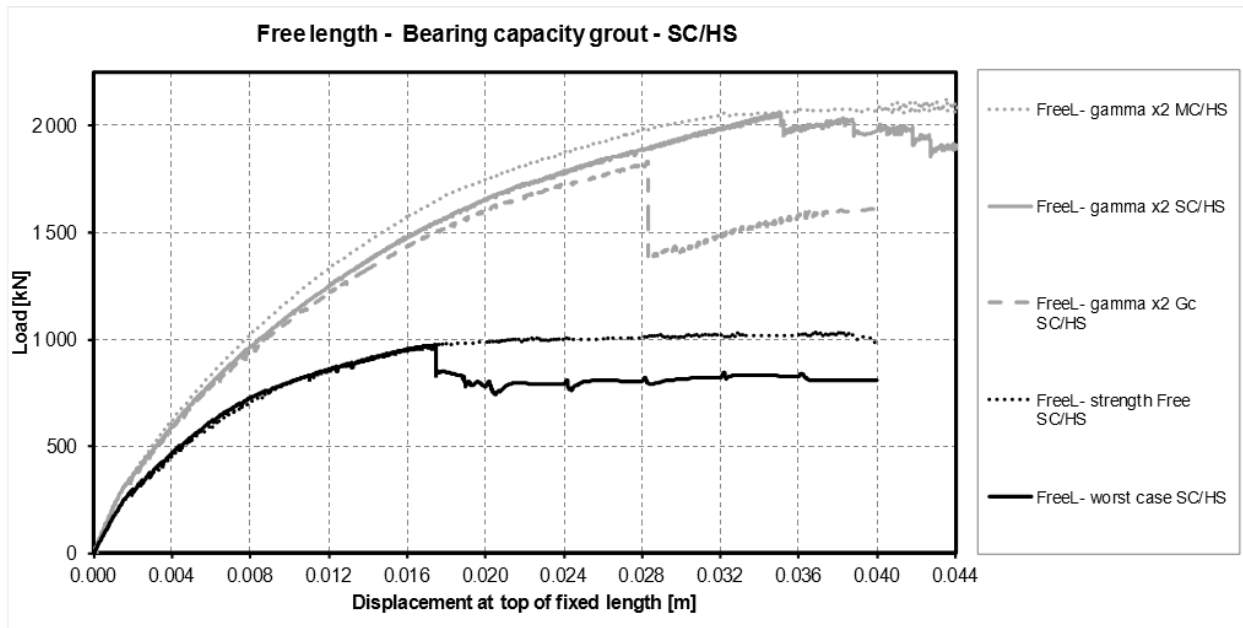


Fig. 6.36. Load-displacement curves of studies on the bearing capacity of the grout

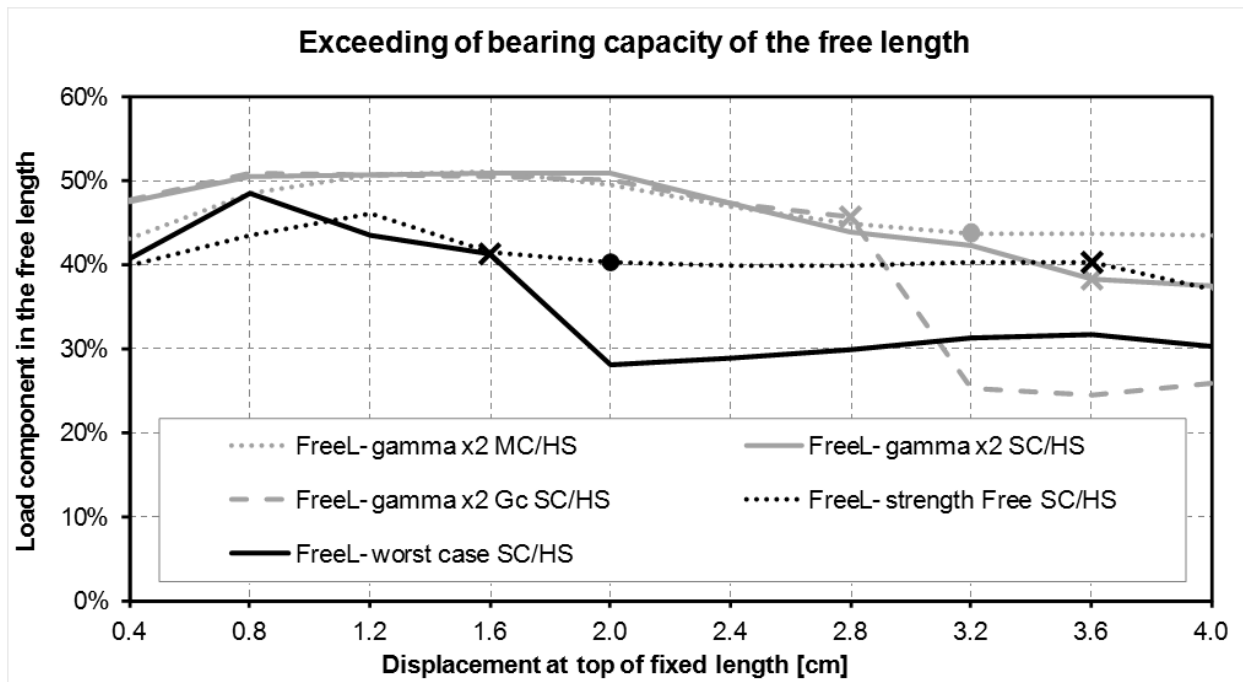


Fig. 6.37. Load distribution at exceedance of bearing capacity grout vs. displacement at top of fixed length

### 6.9 Pressure grouting

As already mentioned in section 2.3, pressure grouting results in an increase in ultimate anchor load bearing capacity of 20 % to 50 % (Witt 2011). The reasons are the expanded grout body and increase in radial stress. The increase in diameter of the grout body has already been considered in the previous calculations, which accounts for an enlargement of the fixed length’s grout surface of 36 %. Additional studies on the increase in radial stress are conducted and presented in this section.

The pressure grouting process is simulated by changing the horizontal initial stress state, using a higher earth pressure coefficient at rest  $K_0$  for the soil layer at the level of the fixed length than for the surrounding soil. The value is increased from 1.0 to 1.5 for these simulations. This approach is



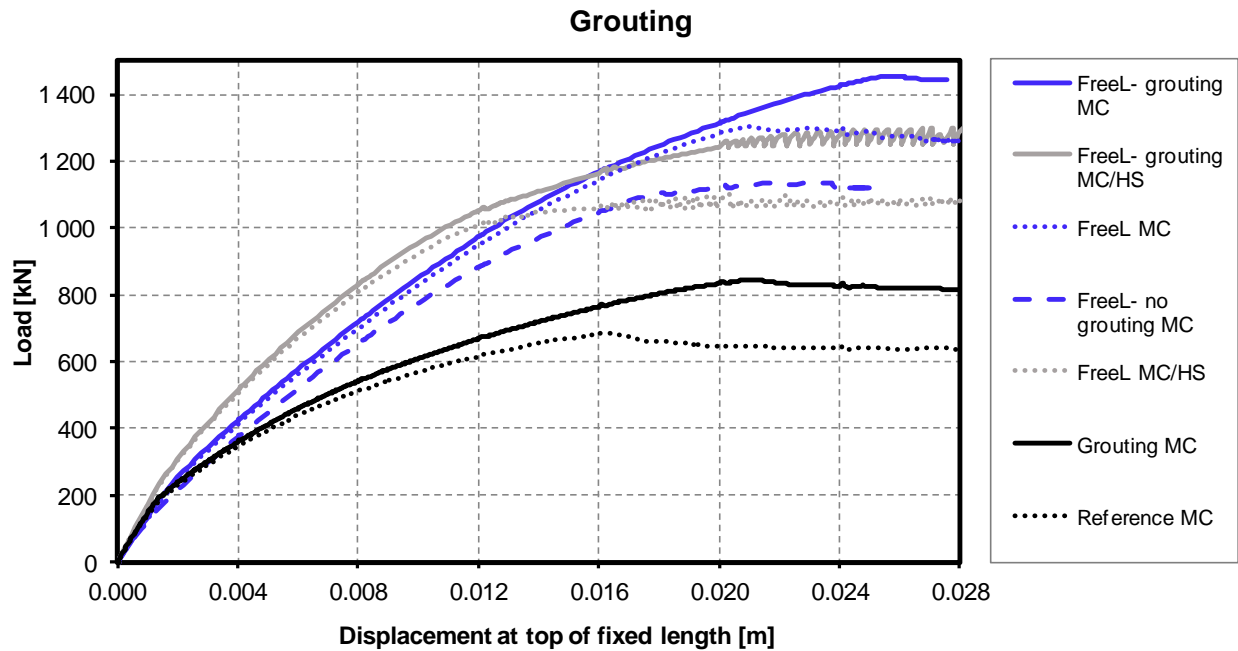


Fig. 6.39. Pressure grouting impact on load-displacement curves

Tab. 6.16. Pressure grouting: comparison of the load bearing capacity and the respective displacement at top of the fixed length

Model	Displacement at peak [m]	Difference	Bearing capacity [kN]	Difference
Reference MC	0.016	-	686	-
Grouting MC	0.021	+31 %	845	+23 %
FreeL MC	0.021	-	1 304	-
FreeL- grouting MC	0.026	+21 %	1 456	+12 %
FreeL- no grouting MC	0.022	+3 %	1 136	-13 %
FreeL MC/HS	0.018	-	1 068	-
FreeL- grouting MC/HS	0.022	+22 %	1 281	+20 %

As anticipated, the ultimate load bearing capacity is not directly proportional to the stress acting perpendicular to the grout body. Several factors account for this, such as the Hvorslev surface. Furthermore, the initial shear stress is increased from 0 to 35 kN/m<sup>2</sup>, since the vertical stress  $\sigma'_{yy}$  stays the same. Fig. 6.40 shows the stress next to top of the grout body (points K, L) against the displacement at top of fixed length. The peak shear stress is increased by 17 % compared to the model *FreeL MC*, whereas the normal stress varies in a smaller range (cf. Fig. 6.12).

Fig. 6.41 shows the mobilised friction angle along the grout body at different displacements for the model *FreeL- grouting MC*. As anticipated, the peak friction angle decreases in the area of the fixed length compared to the model *FreeL MC* (cf. Fig. 6.15) due to the initially increased effective mean stress  $p'$ .

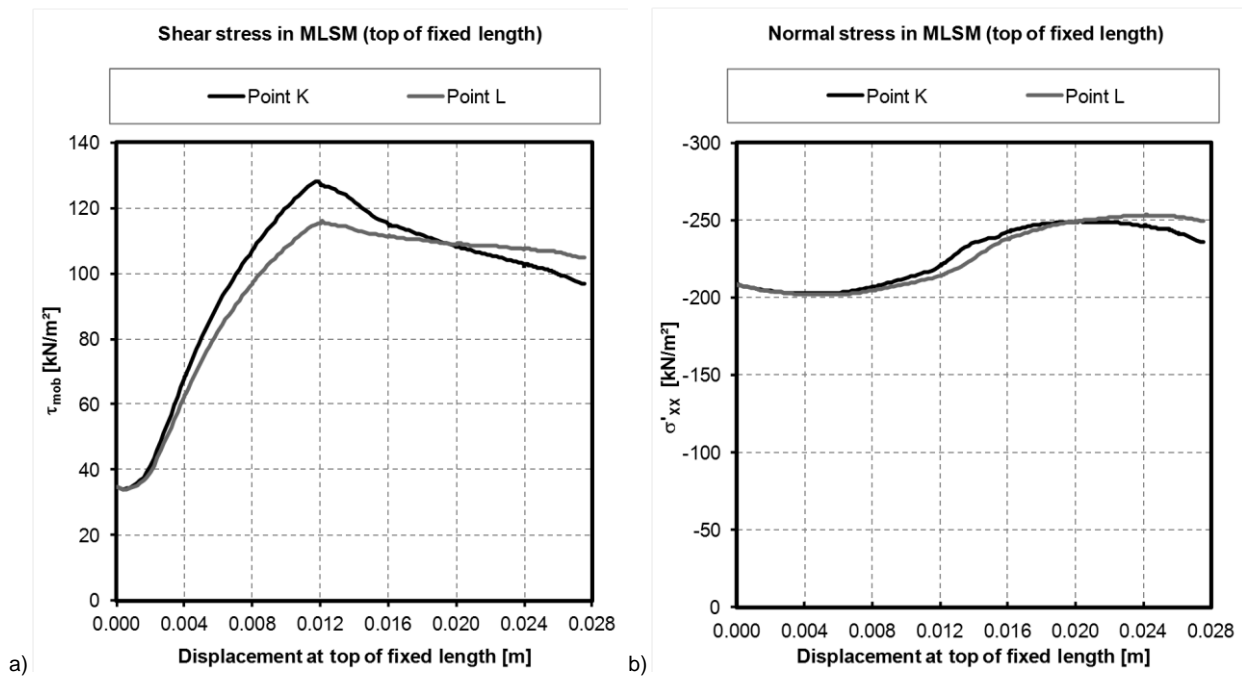


Fig. 6.40. *FreeL-grouting MC*: stress next to top of the grout body (points K, L) vs. displacement at top of fixed length: a) shear stress, b) normal stress

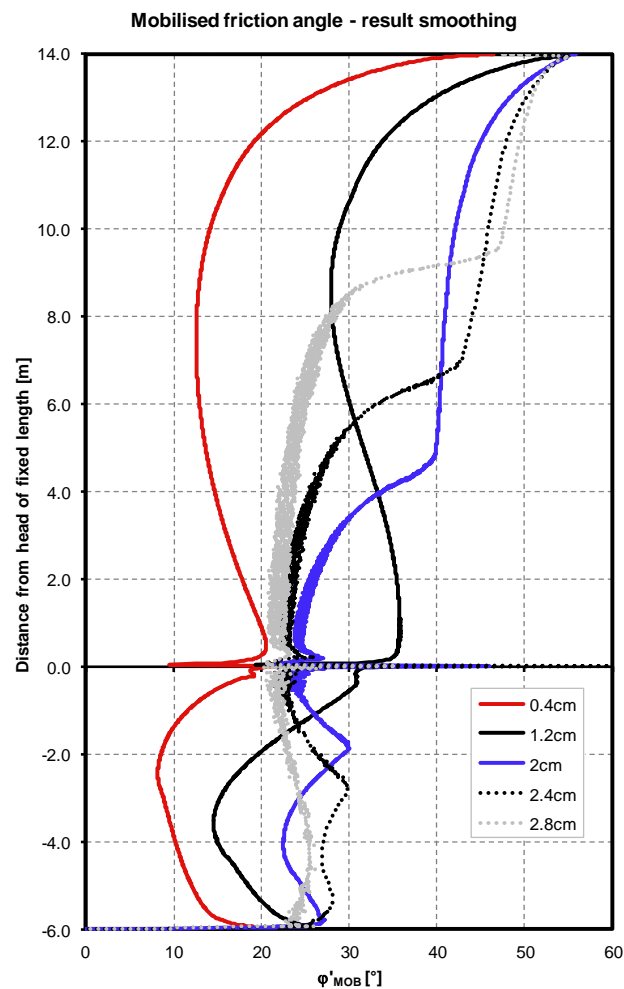


Fig. 6.41. *FreeL-grouting MC*: mobilised friction angle along grout body

The difference between the models *FreeL- no grouting MC* and *FreeL- grouting MC* is 28 %, which is the overall impact of pressure grouting on the ultimate load bearing capacity of this system. Fig. 6.42

shows the influence on the load distribution against the displacement at top of the fixed length. If no enlargement of the fixed length is set, the load component in the free length at peak load increases by 20 % to 65 %.

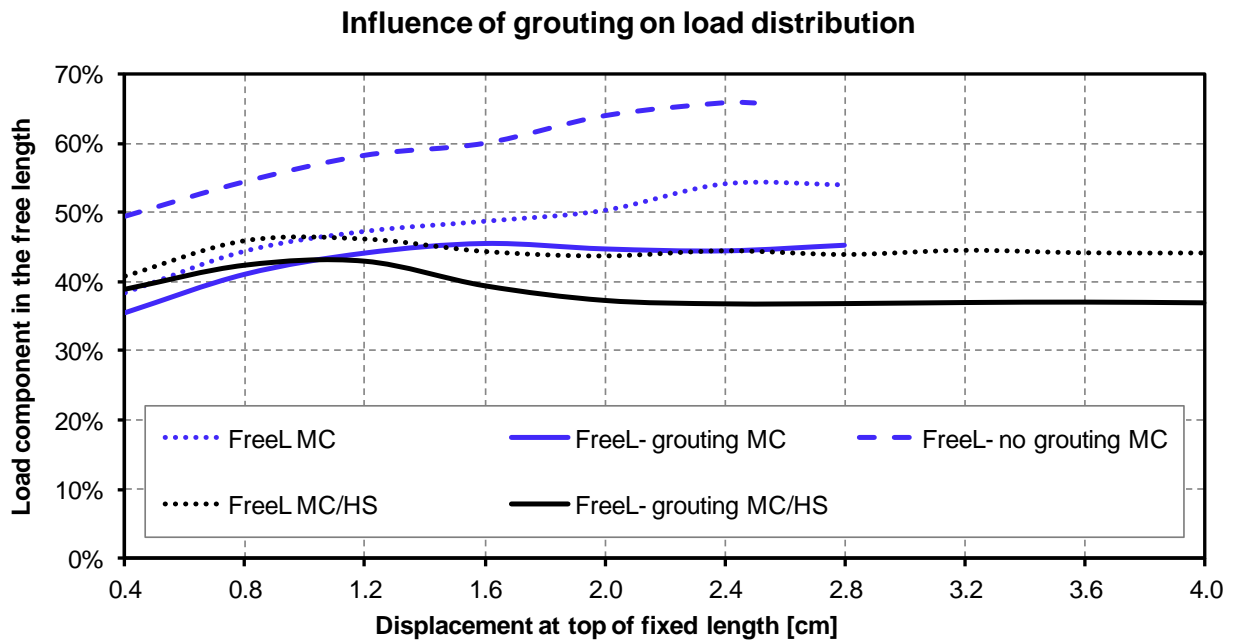


Fig. 6.42. Impact of grouting on load distribution

An estimation of the linear dependency between the radius of the grout body and the ultimate bearing capacity is conducted in Tab. 6.17. The radius is weighted by the respective load proportion in order to account for the free length as well. The result is a decrease in radius in the model *FreeL- no grouting MC* of 15 % compared to the enlarged grout body, which matches well with the decrease in ultimate load bearing capacity of 13 %.

Tab. 6.17. Grouting: dependency between radius of fixed length and ultimate bearing capacity

	Unit	<i>FreeL MC</i>	<i>FreeL- no grouting MC</i>
Load proportion in fixed length at peak	-	50 %	35 %
Load proportion in free length at peak	-	50 %	65 %
Radius fixed length	m	0.15	0.11
Radius free length	m	0.11	0.11
Reduction in radius	-	-27 %	0 %
Weighted radius (=Load proportion times respective radius)	m	0.13	0.11
Reduction in radius	-	-15%	

## 7 Comparison to literature

In order to reproduce the ultimate bearing capacity calculated by PLAXIS, the estimation proposed by Barley (1997) according to Equ. (2-3) is conducted in Tab. 7.1. The efficiency factor is calculated using Equ. (2-4). The estimation of the undrained shear strength in the middle of the fixed length is made based on Equ. (2-5). Moreover, the undrained shear strength is calculated with the PLAXIS SoilTest tool as well. As the undrained shear strength is influenced by the stress path followed during the test, it is computed for both triaxial compression and extension. The arithmetic average is calculated and taken as reference value for the manual determination. The values of the undrained shear strength of the estimation and the PLAXIS SoilTest tool match well. However, this strength is not mobilised in any of the calculations (cf. Fig. 5.11), as they are conducted in drained conditions and the Hvorslev surface would be reached previously anyhow. The reason is the high overconsolidation and the relatively low confining pressure.

The deviation between this estimated bearing capacity according to Barley and the computation of the model *Reference SC* is 4 %. This could be considered as a good fit between estimation and simulation. However, this does not apply to the models with the modelled grout in the free length. Furthermore, as the undrained shear strength is not reached in any of the calculations, this approach has to be questioned for the highly overconsolidated state.

Tab. 7.1. Estimation of the bearing capacity of the Reference model

Estimation of the bearing capacity			
Pre-consolidation stress	$\sigma_{v,p}$	kN/m <sup>2</sup>	1 800
Initial vertical stress (middle of fixed length)	$\sigma'_{v,0}$	kN/m <sup>2</sup>	166
Overconsolidation ratio	OCR	-	10.87
Cohesion	$c'$	kN/m <sup>2</sup>	6
Average undrained shear strength in middle of fixed length	$c_u$	kN/m <sup>2</sup>	218
Undrained shear strength in middle of fixed length according to SoilTest tool (triaxial compression)			223
Undrained shear strength in middle of fixed length according to SoilTest tool (triaxial extension)			182
Undrained shear strength in middle of fixed length according to SoilTest tool (average)			203
Bearing capacity without efficiency factor	$F$	kN	1 234
Efficiency factor (proposed by Barley)	$f_s$	-	0.58
Estimated bearing capacity	$F$	kN	711
Bearing capacity - <i>Reference SC</i>	$F$	kN	680
Bearing capacity - <i>FreeL SC</i>	$F$	kN	1 291

A back calculation of the efficiency factor as proposed by Barley (1997) is conducted in Tab. 7.2 for the models *Reference MC* and *hsoft 500 MC*. The ultimate bearing capacity at maximum efficiency is calculated by assuming that the ultimate bond stress acts along the entire fixed length. Since the stress acting on the anchor increases with depth, the average ultimate bond stress in the middle of the fixed length is applied. This approach underestimates the load slightly. The ratio between the actually computed bearing capacity diminished by the force in the soil at top of the fixed length and this notional force is the efficiency factor. The efficiency is 95 % in the model *Reference MC* and

79 % when the softening ratio is 5 times higher. Yet, both values are higher than the estimation for the models as calculated according to Equ. (2-4) with the result of 58 %.

Tab. 7.2. Estimation of efficiency factor

Estimation of efficiency factor				
Parameter	Symbol	Unit	Reference MC	<i>hsoft 500 MC</i>
Ultimate bond stress (middle of fixed length)	$\tau_{ult}$	kN/m <sup>2</sup>	117	117
Ultimate bearing capacity at max. efficiency	$F_{ult}$	kN	662	662
Computed bearing capacity	$F_{calc}$	kN	629	522
Efficiency factor $\left( = \frac{F_{calc}}{F_{ult}} \right)$	$f_s$	-	0.95	0.79

## 8 Conclusion

In conclusion, the aim of modelling progressive failure on ground anchors in highly overconsolidated clay is achieved. The MLSM intrinsically reproduces shear hardening up to peak shear strength and subsequent strain softening to the residual state. This causes the widely acknowledged non-uniform shear stress distribution along the interface between soil and grout. As the peak of this distribution moves towards the distal end of the anchor along with anchor load increase, inherent dilatancy heightens the stress acting perpendicular to the grout surface. This implicates increase in both ultimate bearing capacity and residual anchor force, at which the residual friction angle is finally reached.

The values entered for softening ratio and POP have high impact on bearing capacity and efficiency of the anchor, which is why thorough calibration of soil tests is necessary. The forms of progressive failure are a matter of the stiffness ratio between anchor and soil. However, it does not affect the ultimate bearing capacity unless the POP is changed as well.

The SC model simulates cracking of the grout body, which also influences shear stress distribution in the adjacent soil. Yet, it only decreases the stiffness of the grout in the basic model, because the interface between soil and grout is decisive in terms of bearing capacity. Numerical ill-conditioning as a result of the snap-back phenomenon can be overcome.

The advanced model revealed the high impact of the incorporated grout in the free length. The ultimate load bearing capacity almost doubles compared to the basic model. It must be pointed out that this solely applies to the given geometries and conditions. However, the OCR in the uppermost soil layers leads to delusive mobilised friction angles in those areas, which amplifies this effect. Especially in these models, high demands are placed on the mesh quality as it has a significant impact on the calculation. Thorough sensitivity analysis is necessary, particularly with such slender geometries. Furthermore, the SC model is susceptible to crack alignment along element boundaries when it comes to compression softening.

The SC model is of greater relevance in the advanced model, although the calculations are still aimed at reproducing failure in the interface between soil and grout. The reason is the focus being set on the behaviour of the grout in the free length. However, if its properties are the same as in the fixed length, the use of the SC model almost solely results in a decrease in stiffness.

Compared to the MC model used for the grout, the load proportion in the free length is slightly changed by the SC model and the capacity of the free length is not fully utilised. The advanced models are generally not susceptible to change in geometries and material properties of the free length in terms of ultimate bearing capacity, since the shear strength of the soil is still decisive in any case. Reduction in uniaxial compressive strength  $f_c$  or compressive fracture energy  $G_c$  of the free length cause vastly spread areas of strain softening at the junction between free and fixed length.

Unlike the basic model calculations, brittle grout in the free length is prone to sudden failure, as it buckles in the computations. If this risk can be eliminated, the factor of safety could be decreased in

the estimations of the bearing capacity. Subsequently, the efficiency of anchors in their practical application would be increased.

The applied approach of implementing pressure grouting by increasing the radial stress by means of earth pressure at rest and fixed length enlargement performs well. However, it is highly dependent on input values.

The estimation of bearing capacity according to Barley (1997) is in accordance with the basic model, although it is calculated with the undrained shear strength, which is of no relevance in this highly overconsolidated state. Yet, it is questionable if the grout in the free length is considered in the calculation. Furthermore, the efficiency factor differs significantly, as it is comparatively high in all of the conducted calculations.

## 9 Registers

### 9.1 List of figures

Fig. 2.1. Schematic longitudinal section and terminology of a prestressed ground anchor (Iten 2011) .....	2
Fig. 2.2. Development of bond stress distribution along the fixed anchor length (Barley 1995) .....	3
Fig. 2.3. Sketch for determination of the bearing capacity (Witt 2011) .....	5
Fig. 2.4. Correlation between fixed anchor length and skin friction in cohesive soil: a) diagrammatic representation, b) legend (Ostermayer 1974).....	6
Fig. 2.5. Dependency between post-grouting pressure and skin friction (Ostermayer 1974) .....	8
Fig. 3.1. Stress-strain curves of different material behaviours.....	9
Fig. 3.2. Yield surface and failure line (Schädlich and Schweiger 2014 b) .....	10
Fig. 3.3. Normalized stress-strain curve in compression (Schädlich and Schweiger 2014 b).....	11
Fig. 3.4. Tension softening: a) yield surface, b) normalized stress-strain curve in tension (Schädlich and Schweiger 2014 b).....	11
Fig. 3.5. Behaviour of overconsolidated clay: a) stress-strain behaviour and dilatancy, b) schematic stress paths and volumetric behaviour (Schädlich and Schweiger 2014 a) .....	13
Fig. 3.6. 3D state boundary surface (Schädlich 2012).....	13
Fig. 3.7. Definition of local stress components and integration plane orientation (Schädlich and Schweiger 2014 a) .....	15
Fig. 3.8. Local yield surfaces (Schädlich 2012) .....	15
Fig. 3.9. Normalised Hvorslev surface on integration plane (Schädlich 2012).....	16
Fig. 3.10. Difference in approaches of strain hardening and softening (Schädlich 2012) .....	16
Fig. 3.11. Dilatancy: a) mobilisation, b) mobilised and maximum angle of dilatancy (Schädlich 2012).....	17
Fig. 4.1. 2D – axial symmetry (Brinkgreve et al. 2014 b) .....	18
Fig. 4.2. Conversion from the inclined to the vertical system: a) inclined, b) vertical .....	19
Fig. 4.3. Basic model geometries (horizontally scaled up 50 times) .....	19
Fig. 4.4. Advanced model geometries (horizontally scaled up 50 times) .....	20
Fig. 4.5. Discretisation of the cross section: a) schematic section of fixed length, b) discretised section fixed length, c) discretised section free length .....	21
Fig. 4.6. Mohr-Coulomb failure line for concrete.....	23
Fig. 5.1. Mesh sensitivity SC: comparison of load-displacement curves .....	31
Fig. 5.2. FE-mesh: a) used mesh, b) fine mesh.....	32
Fig. 5.3. Comparison of different mesh fineness: a) <i>Reference MC</i> , b) <i>Fine mesh MC</i> .....	33
Fig. 5.4. Effective principal stresses without grout in the free length: a) along grout, b) in the grout modelled with MC.....	34
Fig. 5.5. <i>Reference MC</i> : stress along fixed length at different load levels and cross-sections: a) shear stress, b) normal stress.....	35
Fig. 5.6. Oscillations .....	36
Fig. 5.7. <i>Reference MC</i> : Mobilised friction angle along fixed length in a cross-section at a distance of 3 mm to the grout body .....	36
Fig. 5.8. <i>Reference MC</i> : load-displacement curve at top of fixed length (continuous) and load levels for Fig. 5.5 (dotted).....	37
Fig. 5.9. Points and cross-section for analysis.....	38
Fig. 5.10. <i>Reference MC</i> : stress-strain behaviour at point K: a) mobilised shear stress vs. displacement at top of fixed length, b) shear stress in section perpendicular to grout body at point K, c) volumetric and shear strain vs. displacement at top of fixed length, d) displacements along cross-section .....	39
Fig. 5.11. <i>Reference MC</i> : Comparison of the shear stress vs. displacement at top of fixed length in the soil: top (K, L), centre (U) and bottom (V) of the fixed length .....	40
Fig. 5.12. Comparison of load-displacement curves.....	41
Fig. 5.13. Softening behaviour in point K: deviatoric stress vs. shear strain.....	42
Fig. 5.14. Comparison of the load-displacement curves with the MLSM and the HS model featuring the critical state friction angle and models with a low soil stiffness.....	44
Fig. 5.15. Comparison of the shear stress at different points along the fixed length in the MLSM vs. displacement at top of fixed length for different softening ratios and soil stiffness: a) point K (top), b) point L (top), c) point U (centre), d) point V (bottom) of the fixed length.....	45
Fig. 5.16. <i>Reference MC</i> : a) Cartesian strain development $\epsilon_{xx}$ , b) pre-consolidation stress development along fixed length .....	46
Fig. 5.17. <i>Reference MC</i> , <i>hsoft 500 MC</i> , <i>MC/HS</i> : a) Normal stress acting on fixed length (post-peak), b) Normal pre-consolidation stress at three cross-sections at indicated distance along fixed length and POP.....	47
Fig. 5.18. <i>Reference MC</i> , <i>hsoft 500 MC</i> , <i>MC/HS</i> : Shear stress along fixed length: a) pre-peak, b) post-peak.....	47
Fig. 5.19. <i>Reference MC</i> , <i>hsoft 500 MC</i> , <i>MC/HS</i> : Mobilised friction angle along fixed length .....	48
Fig. 5.20. Strain in point K vs. displacement at top of fixed length for different softening ratios and soil stiffness: a) <i>Reference MC</i> : Cartesian and volumetric strain, b) <i>Reference MC</i> , <i>E soil low MC</i> , <i>hsoft 500 MC</i> , <i>E soil low hsoft 500 MC</i> : Cartesian strain $\epsilon_{xx}$ .....	49
Fig. 5.21. Stress along fixed length of <i>hsoft 500 MC</i> , <i>E soil low hsoft 500 MC</i> : a) shear stress, b) normal stress.....	50
Fig. 5.22. <i>E soil low MC</i> : mobilised friction angle along fixed length.....	50
Fig. 5.23. Load-displacement curves with HS model and dilatancy / DCO.....	51

Fig. 5.24. Dilatancy 3° - DCO 0.6 MC: a) shear stress development, b) normal stress development along fixed length .....	51
Fig. 5.25. Load- displacement curves: difference between SC ( <i>Reference SC</i> ) and MC material model ( <i>Reference MC</i> ) for grout body .....	52
Fig. 5.26. Comparison tension softening (scaled from 0 to 1) of different values for the fracture energy $G_f$ at peak load: a) $G_f 0.5$ SC ( $G_f=0.5$ ), b) <i>Reference SC</i> ( $G_f=0.15$ ) and c) effective principal stresses ( <i>Reference SC</i> ; $G_f=0.15$ ) .....	54
Fig. 5.27. Influence of the SC model on the shear stress in soil and variation of fracture energy in tension $G_f$ (dashed: low; dotted: high) at a load level of 390 kN.....	54
Fig. 5.28. <i>Reference SC</i> : Global error and anchor load vs. load steps.....	55
Fig. 5.29. Influence of Young's modulus on the shear stress in soil at two different load levels.....	56
Fig. 6.1. Load-displacement curves for comparison of basic and advanced model .....	57
Fig. 6.2. <i>FreeL SC</i> : normal stress along grout body and approximated normal stress for the residual state with HS .....	60
Fig. 6.3. Comparison of load-displacement curves of initial and residual state of the normal stress acting on the anchor .....	61
Fig. 6.4. Influence of used constitutive model on load distribution .....	63
Fig. 6.5. Comparison of different mesh fineness: a) <i>coarse</i> , b) <i>fine</i> .....	64
Fig. 6.6. Comparison of different mesh fineness: a) <i>FreeL-coarse SC</i> , b) <i>FreeL SC</i> .....	65
Fig. 6.7. Mesh sensitivity advanced model: load-displacement curves .....	65
Fig. 6.8. <i>FreeL-coarse SC</i> : Stress at different points along the grout body (K, L: top; U: centre; V: bottom) vs. displacement at top of fixed length: a) shear stress and load-displacement curve, b) normal stress .....	66
Fig. 6.9. <i>FreeL-coarse SC</i> : top of fixed length at a displacement of 2.4 cm: a) deformed mesh (scaled up 5 times), b) total displacements $u_x$ c) normal pre-consolidation stress, hardening only, plane 1, d) effective principal stresses in soil adjacent to top of fixed length (scaled up 0.25e-3), e) compression hardening/ softening parameter $H_c$ (green: softening).....	68
Fig. 6.10. <i>FreeL-coarse SC</i> : normal stress along grout body .....	68
Fig. 6.11. <i>FreeL-coarse SC</i> : stress in free length: a) Point M, b) Point S .....	69
Fig. 6.12. <i>FreeL MC</i> : stress next to top of the grout body (points K, L) vs. displacement at top of fixed length: a) shear stress and load-displacement curve, b) normal stress .....	70
Fig. 6.13. <i>FreeL MC</i> : top of fixed length at a displacement of 2.4 cm: a) deformed mesh (scaled up 5 times), b) total displacements $u_x$ , c) normal pre-consolidation stress, hardening only, plane 1, d) effective principal stresses in soil adjacent to top of fixed length (scaled up 0.125e-3), e) failure point history.....	71
Fig. 6.14. <i>FreeL MC</i> : stress along grout body: a) shear stress (normalised by respective grout body surface), b) normal stress.....	72
Fig. 6.15. <i>FreeL MC</i> : mobilised friction angle along grout body .....	72
Fig. 6.16. Observed stress points and cross section .....	73
Fig. 6.17. <i>FreeL MC</i> : Principal stress in selected points in grout (junction between fixed and free length) and load-displacement curve (secondary ordinate) vs. displacement at top of fixed length: a) point M, b) point S, c) point N, d) point Q.....	74
Fig. 6.18. <i>FreeL SC</i> : stress next to top of the grout body (points K, L) vs. displacement at top of fixed length: a) shear stress and load-displacement curve, b) normal stress .....	75
Fig. 6.19. <i>FreeL SC</i> : top of fixed length at a displacement of 2.4 cm: a) failure point history, b) compression hardening/ softening parameter $H_c$ (green: softening).....	76
Fig. 6.20. <i>FreeL SC</i> : stress along grout body: a) shear stress (normalised by respective grout body surface), b) normal stress.....	76
Fig. 6.21. <i>FreeL SC</i> : mobilised friction angle along grout body .....	77
Fig. 6.22. <i>FreeL SC</i> : Principal stress in selected points in grout (junction between fixed and free length) and load-displacement curve (secondary ordinate) vs. displacement at top of fixed length: a) point M, b) point S, c) point N, d) point Q.....	78
Fig. 6.23. <i>FreeL SC</i> and <i>FreeL MC</i> : Mohr's circle for peak stress in point Q .....	78
Fig. 6.24. <i>FreeL SC</i> : parameters along cross section at top of fixed length and vs. displacement at top of fixed length: a) compression hardening/ softening parameter $H_c$ along cross section, b) left and right edge vs. displacement at top of fixed length, c) current yield stress $f_{cy}$ along cross section, d) left and right edge vs. displacement at top of fixed length .....	79
Fig. 6.25. Detail (top of fixed length) of compared models with grout in the free length: a) <i>FreeL SC/HS</i> , b) <i>FreeL-no support SC/HS</i> , c) <i>FreeL-width-no support SC/HS</i> (prescribed displacement not displayed) .....	80
Fig. 6.26. Load-displacement curves of geometries and support condition alterations .....	81
Fig. 6.27. Influence of geometries on load distribution .....	82
Fig. 6.28. <i>FreeL-width-no support SC/HS</i> : compression hardening/ softening parameter $H_c$ (green: softening) at various displacements of 4 cm: a) 0.4 cm, b) 0.8 cm, c) 1.2 cm, d) 4 cm.....	82
Fig. 6.29. <i>FreeL-width-no support SC/HS</i> : junction between free and fixed length at a displacement of 4 cm: a) total principal strain $\epsilon_1$ , b) deformed mesh (scaled up 2 times), c) total displacement $u_x$ .....	83
Fig. 6.30. <i>FreeL SC/HS</i> : junction between free and fixed length at a displacement of 4 cm: a) compression hardening/ softening parameter $H_c$ (green: softening), b) total principal strain $\epsilon_1$ , c) deformed mesh .....	83
Fig. 6.31. Equivalent length $L_{eq}$ : a) <i>FreeL SC/HS</i> , b) <i>FreeL-width-no support SC/HS</i> .....	84
Fig. 6.32. Load-displacement curves of SC material parameter alterations .....	85
Fig. 6.33. <i>FreeL-strength Free SC/HS</i> : junction between free and fixed length at a displacement of 3.6 cm: a) total principal strain $\epsilon_1$ , b) deformed mesh (scaled up 2 times), c) total displacement $u_x$ , d) compression hardening/ softening parameter $H_c$ (green: softening) .....	86
Fig. 6.34. <i>FreeL-strength Free SC/HS</i> : Mohr's circle for peak stress in point Q.....	87

Fig. 6.35. Influence of material parameters on load distribution ..... 87

Fig. 6.36. Load-displacement curves of studies on the bearing capacity of the grout..... 89

Fig. 6.37. Load distribution at exceedance of bearing capacity grout vs. displacement at top of fixed length ..... 89

Fig. 6.38. Simulation of grouting with  $K_0$ -procedure..... 90

Fig. 6.39. Pressure grouting impact on load-displacement curves ..... 91

Fig. 6.40. *FreeL-grouting MC*: stress next to top of the grout body (points K, L) vs. displacement at top of fixed length: a) shear stress, b) normal stress ..... 92

Fig. 6.41. *FreeL-grouting MC*: mobilised friction angle along grout body..... 92

Fig. 6.42. Impact of grouting on load distribution ..... 93

## 9.2 List of tables

Tab. 3.1. Application and material behaviour of applied constitutive models .....	9
Tab. 4.1. Parameters and results of the initial stress state .....	18
Tab. 4.2. Axial stiffness and force at failure – free length with and without void and comparison of free and fixed length .....	21
Tab. 4.3. Main geometries and properties .....	22
Tab. 4.4. Material parameters – tendon .....	23
Tab. 4.5. Material parameter grout body – Mohr-Coulomb model .....	23
Tab. 4.6. Material parameter grout body – Shotcrete model .....	24
Tab. 4.7. HS – parameters surrounding soil .....	25
Tab. 4.8. MLSM – parameters Reference model .....	26
Tab. 5.1. Reference models: employed material models .....	27
Tab. 5.2. Basic model: overview of performed analyses and changed parameters .....	29
Tab. 5.3. Iteration procedure settings .....	30
Tab. 5.4. Basic model: mesh sensitivity analysis .....	30
Tab. 5.5. Results – mesh sensitivity analysis .....	31
Tab. 5.6. Location of selected stress points and cross-section for comparison .....	37
Tab. 5.7. Comparison of softening parameters – input parameters and results .....	43
Tab. 5.8. Comparison of the load bearing capacity and the respective displacement at top of the fixed length .....	44
Tab. 5.9. Calculation according to static approach with the critical state friction angle .....	45
Tab. 5.10. Changed parameters for comparison .....	52
Tab. 5.11. Comparison of the load bearing capacity and the respective displacement for the determination of the SC model impact .....	53
Tab. 5.12. Changes and results of the geometry modifications .....	56
Tab. 6.1. Grout in free length: comparison of the load bearing capacity and the respective displacement at top of the fixed length .....	58
Tab. 6.2. Advanced model: overview of performed analyses and changed parameters .....	59
Tab. 6.3. Approximated residual normal stress state for calculations with HS model .....	60
Tab. 6.4. Modifications for HS model: comparison of the load bearing capacity and the respective displacement at top of the fixed length .....	61
Tab. 6.5. Calculative load distribution in HS model .....	62
Tab. 6.6. Free length: mesh sensitivity analysis .....	63
Tab. 6.7. Advanced model: mesh sensitivity analysis .....	66
Tab. 6.8. Location of selected stress points and cross-section for comparison .....	73
Tab. 6.9. Free length: changed conditions for comparison .....	80
Tab. 6.10. Geometry alterations in free length: comparison of the load bearing capacity and the respective displacement at top of the fixed length .....	80
Tab. 6.11. Free length: changed SC parameters for comparison .....	85
Tab. 6.12. SC material parameter alterations: comparison of the load bearing capacity and the respective displacement at top of the fixed length .....	85
Tab. 6.13. <i>FreeL- strength low SC/HS</i> : load free length .....	86
Tab. 6.14. Free length: analyses of the bearing capacity of the grout .....	88
Tab. 6.15. Bearing capacity of the grout: comparison of the load bearing capacity and the respective displacement at top of the fixed length .....	88
Tab. 6.16. Pressure grouting: comparison of the load bearing capacity and the respective displacement at top of the fixed length .....	91
Tab. 6.17. Grouting: dependency between radius of fixed length and ultimate bearing capacity .....	93
Tab. 7.1. Estimation of the bearing capacity of the Reference model .....	94
Tab. 7.2. Estimation of efficiency factor .....	95

### 9.3 List of notations and abbreviations

#### Capital letters

$A_{fixed}$	[m <sup>2</sup> ]	Area fixed length
$A_{free}$	[m <sup>2</sup> ]	Area free length
$A_{grout}$	[m <sup>2</sup> ]	Area of the modelled grout
$A_M$	[m <sup>2</sup> ]	Grout surface
$A_{mat}$	[-]	Shear hardening parameter
$A_{strand}$	[m <sup>2</sup> ]	Single area strand
$A_{strands}$	[m <sup>2</sup> ]	Total area 4 strands
$D$	[m]	Diameter
$E$	[kN/m <sup>2</sup> ]	Young's modulus
$E_1/E_{28}$	[-]	Time dependency of elastic stiffness
$E_{28}$	[kN/m <sup>2</sup> ]	Young's modulus at a shotcrete age of 28 days
$E_{50,ref}$	[kN/m <sup>2</sup> ]	Secant modulus from triaxial test at reference pressure
$E_{oed,ref}$	[kN/m <sup>2</sup> ]	Oedometric stiffness at reference pressure
$E_{oed,ref}$	[kN/m <sup>2</sup> ]	Tangential modulus from oedometer test at reference pressure
$E_{tendon}$	[kN/m <sup>2</sup> ]	Young's modulus of the tendon
$E_{ur,ref}$	[kN/m <sup>2</sup> ]	Unloading / reloading modulus at reference pressure
$F_c$	[-]	Mohr-Coulomb yield surface
$F_{calc}$	[kN]	Computed bearing capacity
$F_t$	[-]	Rankine yield surface
$F_{ult}$	[kN]	Ultimate bearing capacity at max. efficiency
$G_{c,28}$	[kN/m]	Fracture energy in compression
$G_{t,28}$	[kN/m <sup>2</sup> ]	Fracture energy in tension
$H_c$	[-]	Normalized compression hardening / softening parameter
$H_t$	[-]	Normalized tension softening parameter
$K_0$	[-]	Earth pressure at rest
$K_{0,nc}$	[-]	Earth pressure coefficient in normal consolidation
$L$	[m]	Fixed length
$L_{cal}$	[m]	Internal length for non-local regularization
$L_{eq}$	[m]	Equivalent length
$MaxPoint$	[-]	Maximum # stresspoints for non-local regularization
$M_{cs}$	[-]	Critical stress ratio
$M_{cp}$	[-]	Cap shape parameter
$OCR$	[-]	Overconsolidation ratio
$POP$	[kN/m <sup>2</sup> ]	Pre-overburden pressure
$R_f$	[-]	Failure ratio
$R_{p0.1k}$	[kN]	Force at yield point
$R_{p0.1k}$	[kN]	Force at yield point (4 strands)
$TCO (\sigma_t)$	[kN/m <sup>2</sup> ]	Tension cut-off (tensile strength)
$T_F$	[kN]	Bearing capacity
$UCS$	[kN/m <sup>2</sup> ]	Uniaxial compressive strength
$WF$	[-]	Switch for non-local weighting functions

## Small letters

$a$	[-]	Increase of $\varepsilon_{cp}$ with increase of $p'$
$a_{ad}$	[-]	Adhesion factor
$a_f$	[-]	Factor for conversion to normal stress on lateral surface
$c'_{ref}$	[kN/m <sup>2</sup> ]	Cohesion
$c_u$	[kN/m <sup>2</sup> ]	Undrained shear strength
$e$	[-]	Void ratio
$f_c$	[kN/m <sup>2</sup> ]	Uniaxial compressive strength
$f_{c,1}/f_{c,28}$	[-]	Time dependency of strength
$f_{c0,n}$	[-]	Normalized initially mobilised strength (compression)
$f_{cap}$	[-]	Cap yield surface
$f_{cone}$	[-]	Cone yield surface
$f_{ct,n}$	[-]	Normalized failure strength (compression)
$f_{cu,n}$	[-]	Normalized residual strength (compression)
$f_{cy}$	[kN/m <sup>2</sup> ]	Current compressive yield stress
$f_{HV}$	[-]	Hvorslev yield surface
$f_s$	[-]	Efficiency factor
$f_t$	[kN/m <sup>2</sup> ]	Ultimate uniaxial tensile strength
$f_{tu,n}$	[-]	Residual strength level
$f_{yk}$	[kN/m <sup>2</sup> ]	Yield strength
$f_{yk}$	[kN/m <sup>2</sup> ]	Yield strength
$h$	[m]	Overburden
$h_{soft}$	[-]	Softening parameter
$m$	[-]	Power exponent for stress-dependency of stiffness
$n_{CP}$	[-]	Number of integration planes
$p'$	[kN/m <sup>2</sup> ]	Effective mean stress
$p_{ref}$	[kN/m <sup>2</sup> ]	Reference pressure
$r$	[m]	Radius
$r_{fixed}$	[m]	Radius fixed length
$r_{free}$	[m]	Radius free length
$r_{strands}$	[m]	Radius continuum of 4 strands
$r_{void}$	[m]	Radius void
$stepsize$	[kN/m <sup>2</sup> ]	Maximum substep size stress
$switch_{HV}$	[-]	Switch to activate model features
$switch_{p/\sigma}$	[-]	Switch for stiffness dependence
$t_{50}^{cr}$	[d]	Time for 50% of creep strains
$t_{50}^{shr}$	[d]	Time for 50% of shrinkage strains
$t_{hydr}$	[d]	Time for full hydration
$U_{max}$	[m]	Max. displacements
$U_x$	[m]	Total displacements
$q$	[kN/m <sup>2</sup> ]	Deviatoric stress
$q_{max}$	[kN/m <sup>2</sup> ]	Max. deviatoric stress
$q_{res}$	[kN/m <sup>2</sup> ]	Residual deviatoric stress

## Greek letters

$\varepsilon_{\infty}^{shr}$	[-]	Final shrinkage strain
$\varepsilon_1, \varepsilon_2, \varepsilon_3$	[-]	Total major, intermediate and minor principal strain
$\varepsilon_{cp}^P$	[-]	Uniaxial plastic failure strain at 1h, 8h, 24h
$\varepsilon_{cp}^D$	[-]	Plastic peak strain in uniaxial compression
$\varepsilon_v$	[-]	Volumetric strain
$\varepsilon_{xx}, \varepsilon_{yy}, \varepsilon_{zz}$	[-]	Cartesian strain in direction X, Y, Z
$\phi^{cr}$	[-]	Ratio between creep and elastic strains
$\phi^{max}$	[°]	Maximum friction angle
$\gamma$	[kN/m <sup>3</sup> ]	Unit weight
$\gamma_{fc}$	[-]	Safety factor for compressive strength
$\gamma_{ft}$	[-]	Safety factor for tensile strength
$\gamma_s$	[-]	Total deviatoric strain
$\gamma_{xy}$	[-]	Total Cartesian shear strains on plane X pointing in global axis Y
$\phi'$	[°]	Effective friction angle
$\phi_e$	[°]	Hvorslev surface inclination
$\phi'_{max}$	[°]	Maximum friction angle
$\phi'_{mob}$	[°]	Mobilised friction angle
$\phi_{res}$	[°]	Critical state friction angle
$\nu$	[-]	Poisson's ratio
$\nu'_{ur}$	[-]	Poisson's ratio in un/reloading (isotropic)
$\sigma'_1, \sigma'_2, \sigma'_3,$	[kN/m <sup>2</sup> ]	Major, intermediate and minor principal stress
$\sigma'_N$	[kN/m <sup>2</sup> ]	Normal stress
$\sigma'_{nc}$	[kN/m <sup>2</sup> ]	Current pre-consolidation stress
$\sigma_{nc}^*$	[kN/m <sup>2</sup> ]	Normal pre-consolidation stress with Hvorslev softening
$\sigma_{nc0}$	[kN/m <sup>2</sup> ]	Initial value of $\sigma_{nc}$
$\sigma'_{ne}$	[kN/m <sup>2</sup> ]	Equivalent stress
$\sigma'_{xx}, \sigma'_{yy}, \sigma'_{zz}$	[-]	Cartesian effective stress on plane X, Y, Z
$\sigma_{xy}$	[-]	Shear stress on plane X pointing in global axis Y
$\tau_{mob}$	[kN/m <sup>2</sup> ]	Mobilised shear stress
$\tau_{ult}$	[kN/m <sup>2</sup> ]	Ultimate bond stress (middle of fixed length)
$\psi$	[°]	Dilatancy angle
$\psi_m$	[°]	Mobilised dilatancy angle

## Abbreviations

CSL	Critical state line
FE	Finite elements
FEM	Finite element method
FreeL	Free length (indicates grout in free length)
HS	Hardening soil (model)
LE	Linear elastic
MC	Mohr-Coulomb
MLSM	Multilaminar soil model
SBMA	Single Bore Multiple Anchor
SC	Shotcrete (model)
UDSM	User-defined soil model

## 9.4 References

Barley, A. D. (1995)

*Theory and practice of the Single Bore Multiple Anchor System*, Proc. of the International Symposium on Anchors in Theory and Practice, Salzburg, Austria, pp. 293-301.

Barley, A. D. (1997)

*The Single Bore Multiple Anchor System*. Proc. Int. Conf.: Ground anchorages and anchored structures. London, pp. 65-75.

Brinkgreve, R.B.J.; Engin, E.; Swolfs, W.M. (2014 a)

*PLAXIS 2D Anniversary Edition 2014 – Material Models Manual*. Plaxis bv, Delft, Niederlande.

Brinkgreve, R.B.J.; Engin, E.; Swolfs, W.M. (2014 b)

*PLAXIS 2D Anniversary Edition 2014 – Reference Manual*. Plaxis bv, Delft, Niederlande.

Evangelista, A. and Sapio, G. (1978)

*Behaviour of Ground Anchors in Stiff Clays*, Speciality Session No. 4, 9<sup>th</sup> Int. Conf. Soil Mech. Found Eng., Tokyo, pp.39-47.

Galavi, V. (2007)

*A multilaminate model for structured clay incorporating inherent anisotropy and strain softening*. Ph.D. thesis, Gruppe Geotechnik Graz, Graz University of Technology, Austria, Heft 32.

Iten, M. (2011)

*Novel Application of Distributed Fiber-Optic Sensing in Geotechnical Engineering*, Dissertation, ETH Zürich.

Mayer, A. (2008)

*FE-Berechnungen zum Tragverhalten von Ankern im Boden*, Master's thesis, Graz University of Technology, Austria.

Miča L., Chalmovsky J., Fiala R., Račanský V. (2011)

*Numerical analysis of retaining structures (in Czech)*. CERM s.r.o., Brno

Ostermayer, H. (1974)

*Construction Carrying Behaviour and Creep Characteristics of Ground Anchors*, Conf. on Diaphragm Walls and Anchorages, Inst. Civil Engineers, London, pp. 141-151.

Schädlich, B. (2012)

*A Multilaminate Constitutive model for Stiff Soils*, Ph.D. thesis, Gruppe Geotechnik Graz, Graz University of Technology, Austria, Heft 47.

Schädlich, B. (2014)

*How to use the multilaminate soil model MMS\_HV*, Computational Geotechnics Group, Graz University of Technology.

Schädlich, B.; Schweiger, H.F. (2014 a)

*Modelling the shear strength of overconsolidated clays with a Hvorslev surface*. In: geotechnik 37, Ernst & Sohn, Berlin, pp. 47-56.

Schädlich, B.; Schweiger, H.F. (2014 b)

*Shotcrete model – Internal report: Implementation, validation and application of the shotcrete model*, Computational Geotechnics Group, Graz University of Technology.

Terzaghi, K.; Peck, R.B. (1948)

*Soil Mechanics in Engineering Practice*, 1st Edition, John Wiley and Sons, New York.

Witt, Karl Josef (ed.) (2011)

*Grundbau-Taschenbuch. Teil 2: Geotechnische Verfahren*. 7. Aufl., 1. Nachdr. Berlin: Ernst & Sohn, pp. 303-366.

Xanthakos, P. (1991)

*Ground anchors and anchored structures*, John Wiley & Sons, Inc.

Zong-Ze, Y.; Hong, Z.; Guo-Hua, X. (1995)

*A study of deformation in the interface between soil and concrete*. Computers and Geotechnics, 17(1), pp. 75–92